Antibody Conjugated Nano and Microparticle Systems for Targeted Immunosuppression and Purification of Extracellular Vesicles

By

Christopher P. Haycook, M.S.

Dissertation

Submitted to the Faculty of the

Graduate School of Vanderbilt University

in partial fulfillment of the requirements

for the degree of

DOCTOR OF PHILOSOPHY

in

Biomedical Engineering

October 31st, 2021

Nashville, Tennessee

Approved:

Todd D. Giorgio, PhD

John T. Wilson, PhD

Frederick R. Haselton, PhD

Amy S. Major, PhD

Jeffrey L. Franklin, PhD

This thesis is dedicated to my wife, Margaret, who has constantly supported and encouraged me to overcome any challenge I encounter. I am truly grateful to have you in my life. Without your support, I would never have finished. This work is also dedicated to my parents, Lisa and Herbert Haycook, who have always loved me unconditionally and motivated me to accomplish whatever goals I aspired to achieve.

ACKNOWLEDGEMENTS

I would like to thank my advisor Dr. Todd Giorgio and collaborating faculty members Dr. Amy Major, Dr. Charles Hong, Dr. Jeffrey Franklin, and Dr. Robert Coffey for their support throughout this work. Thank you to my dissertation committee for providing scientific guidance and for pushing me to overcome the many exciting challenges and conundrums that scientific research has to offer. I would also like to thank several members of the Giorgio, Major, Coffey, Hong, and Duvall laboratories for their help through this project. Thank you to Isom Kelly for providing nanoparticle synthesis training. Thank you to Evan Glass for conducting many of the preliminary experiments with me presented in Chapter 2. Thank you to Jillian Rhoads and Joe Balsamo for conducting flow cytometry analysis and ELISAs for Chapter 2. Thank you to James Higginbotham for conducting the flow cytometry analysis for Chapter 3. Thank you to Alex Sorets and Zheng Cao for conducting the western blots for Chapter 3. Thank you to Charles Williams for providing the Eggmanone used in all experiments presented herein. Thank you to my undergraduate colleagues Carla Pax and Fan Xue for supporting the work presented herein. Thank you to my undergraduate mentor, Dr. M. Robert Gower, for providing the initial research training that motivated me to pursue biomedical engineering graduate research. Lastly, I would like to thank my friends and family for supporting me throughout my graduate education.

TABLE OF CONTENTS

Page

LIST OF TABLES

LIST OF FIGURES

CHAPTER 1

INTRODUCTION

BACKGROUND AND SIGNIFICANCE

Antibodies are an Extension of the Adaptive Immune System

Antibodies are specialized proteins that recognize specific molecular sequences known as antigens that are present on pathogens and the cells and tissues of the body. The five main classes of antibodies, IgG, IgM, IgA, IgD, and IgE, are produced by B cells and plasma cells in order to extend the reach of the adaptive immune system into the extracellular space. Each class of antibody is involved in unique cellular processes such as neutralization of viruses in the extracellular space, opsonization of pathogens, and degranulation of mast cells. Those produced by several different immune cells are defined as polyclonal antibodies while antibodies produced by clones of single immune are known as monoclonal antibodies. Antibodies have been refined by evolution to find their targets throughout the body and have thus been repurposed for both therapeutic and diagnostic applications.[1]

Antibody Conjugates Enable Antigen Specific Drug Delivery

One of the most successful drugs ever produced is Humira (adalimumab, AbbVie), a monoclonal antibody therapy that depletes the pro-inflammatory cytokine tumor necrosis factor alpha (TNF-α) to relieve the symptoms of several autoimmune diseases including rheumatoid arthritis. Humira has become one of the most widely prescribed therapies in the world and has produced approximately 150 billion dollars in revenue since 2011.[2] Other monoclonal antibody therapies,

such as pembrolizumab and ipilimumab, have also resulted in significant advancements in survival for patients with metastatic cancer by blocking immune checkpoint proteins from binding with their partner proteins. Because of their large molecular size, antibodies are normally unable to cross cell membranes. Despite this, several antibody drug conjugates (ADCs) have been approved to target the intracellular delivery of chemotherapies. ADCs typically consist of a cell surface receptor-targeting IgG antibody that is attached to a small molecule, cytotoxic drug through a customizable linker. ADC linkers include a chemical group for antibody attachment as well as the option of a cleavable site that can release the drug. In order to enable intracellular delivery, ADCs utilize receptor mediated delivery mechanisms that target internalizing receptors on the surface of cancer cells. Once internalized, the cleavable linkers are destroyed by endosomal proteases, such as cathepsin B, and the cytotoxic drugs are released into the cytoplasm.[2]

The Clinical Need for Targeted Drug Delivery Systems in Rheumatic Autoimmunity

T and B cell activity is dysregulated in a variety of rheumatic autoimmune diseases. Rheumatic autoimmune diseases preferentially affect women and result from inappropriate activation of the immune system, characterized by systemic inflammation within connective tissues including cartilage, joint synovium, and the skin.[3] With the exception of rheumatoid arthritis, targeted therapeutic options for rheumatic autoimmune diseases are limited. This is due to a general lack of understanding of disease mechanisms and the heterogenous nature of many of these diseases. Much like what is observed in cancer, the pathological conditions of patients diagnosed with a single autoimmune disease are actually diverse in almost all cases.[4] Standard treatment usually consists of chronic usage of immunosuppressants and glucocorticoids which results in compromised immunity, premature cardiovascular disease, and osteoporosis.[3] Therefore, the

development of new targeted therapies is vital in order to enable a precision medicine approach for autoimmune diseases.

Inhibition of Germinal Center Reactions May Represent a Novel Therapeutic Strategy for Rheumatic Autoimmunity

The germinal center (GC) reaction is an interaction of antigen-specific B cells, $CD4^+$ T follicular helper (Tfh) cells, and follicular dendritic cells (FDCs) that occurs during an infection in order to produce high-affinity antibodies that act as an extension of the adaptive immune system.[5] In the case of autoimmunity, the GC reaction can result in potentially pathogenic antibodies due to a breakdown of peripheral tolerance mechanisms. Central to Tfh cell and B cell cooperation in the GC reaction is their physical interaction at the immune synapse (IS). The IS is an area of concentrated signaling at the point where the membranes of the T cell and antigen presenting cell (APC) make physical contact. Formation of the IS between $CD4^+$ Tfh cells and B cells is critical for the production of autoantibodies that potentiate the symptoms of rheumatic autoimmunity. Specific disruption of autoimmune IS formation in the germinal center may represent a potential therapeutic strategy that could eliminate the need for chronic usage of immunosuppressants and glucocorticoids in rheumatic autoimmune diseases, such as systemic lupus erythematosus (SLE).

SLE is a debilitating autoimmune disease with complications including arthritis, nephritis pleural edema, neuropathies, and premature cardiovascular disease. SLE affects as many as 150 per 100,000 individuals, and the incidence is increased in women, especially among African Americans, up to 406 per 100,000. There is currently no cure for SLE, and only one approved therapy, Benlysta, has ever been developed specifically for SLE. One issue slowing development of treatments is a lack of complete understanding of disease mechanisms. Although SLE is

largely thought of as an antibody-mediated disease, potentiation of the B cell response via interaction with T helper cells and other accessory immune cells is critical to auto-antibody production. Thus, modulation of the cells involved in the GC reaction could enable novel targeted therapies for SLE and other rheumatic autoimmune diseases.

PDE4 is a Promising Drug Target for Chronic Inflammatory Diseases

Phosphodiesterases (PDEs) are excellent pharmacologic targets for chronic inflammatory diseases because of their role in the regulation of subcellular cyclic adenosine monophosphate (cAMP) gradients and their sensitivity to small molecule inhibitors.[6–8] PDE4 regulates the pro-inflammatory actions of monocytes, B cells, T cells, and neutrophils and is central to the production of cytokines in inflammatory cells.[9] In T cells, PDE4 is involved in signal transduction via association with CD28.[10,11] The production of cytokines and T cell proliferation are dependent on PDE4 activity.[12–15] PDE4 is recruited to the cell surface when CD28 and the TCR are cross-ligated, reducing local TCR induced production of cAMP and suppressing the inhibitory protein kinase A (PKA)/C-terminal Src kinase (Csk)/lymphocyte-specific protein tyrosine kinase (Lck) pathway. Reduction of local cAMP levels by PDE4 allows Lck to be activated so that T cell cytokine production and antigen-induced proliferation can occur.[12,16,17] PDE4 inhibitors have already been tested in several small clinical trials involving patients with cutaneous lupus erythematosus, discoid lupus erythematosus, and SLE, but none have resulted in clinical approval for new therapies focused on PDE4 inhibition.[18–20] Additionally, SLE is already treated with anti-inflammatory therapies that inhibit the same processes that are controlled by PDE4. PDE4 inhibitors have reduced disease progression in murine models of SLE, and PDE4 overexpression was detected in PBMCs isolated from SLE patients.[21–24]

Eggmanone is a Novel Allosteric Inhibitor of PDE4

Despite the clinical success of the PDE4 inhibitor Otezla® in small trials for the treatment of discoid lupus and lupus skin rashes, no studies have demonstrated efficacy in patients with SLE.[25–30] Altering the treatment landscape for SLE requires novel targets and therapeutic agents. One such example is the small molecule Eggmanone (Egm). Egm strongly and specifically inhibits PDE4, leading to locally increased cAMP levels that activate PKA.[31] Egm inhibits all isoforms of the PDE4 family (except PDE4D2) with an IC50 in the range of 0.8-3 μM. Moreover, because Egm does not target the super-short PDE4D2, the most abundant PDE4 isoform present in the cytoplasm, cAMP levels are largely unaffected outside the peri-ciliary microdomain.[32] However, Egm is limited by its poor solubility in aqueous environments and needs a rationally designed drug delivery vehicle to enable *in vivo* efficacy.

The Physical Properties of Nanoparticles Enable Semi-Targeted Drug Delivery

Particle size and zeta potential are known to be important physical properties that influence the circulation half-life, biodistribution, and cellular uptake of nanoparticle drug delivery systems.[33] Once injected intravenously, the size of nanoparticles largely dictates which organs they accumulate in. Particles greater than 200 nm generally accumulate in the spleen and liver, while those between 10 and 100 nm can drain into the lymphatic system and accumulate in lymph nodes.[34,35] Perhaps the most well-known application of nanoparticle size in drug delivery is the enhanced permeation and retention (EPR) effect. Nanoparticles that are approximately 100 nm in diameter have been routinely designed to deliver various cargo, specifically to tumors, by passing through leaky vasculature formed in murine tumor models.[36] Additionally, the zeta potential of nanoparticle targeting systems has also been shown to significantly affect the

potential of cellular binding due to electrostatic interactions with the cell membrane.[33] Nanoparticles with cationic surface charges preferentially interact with negatively charged cell membranes irrespective of targeting ligand conjugation.[37] Conversely, nanoparticles with anionic surface charges are less likely to bind with cell membranes because of electrostatic repulsion that can lead to reduced immunogenicity and increased circulation potential.[38] However, the physicochemical properties of nanoparticle formulations alone are often not sufficient to enable truly selective drug delivery. In order to fully achieve targeted nanoparticle drug delivery to specific cell subsets, some form of targeting ligand must be incorporated into the nanoparticle formulation.

Antibodies Enable Diagnostic Monitoring of Disease

The development of hybridoma technology by Kohler and Milstein in 1975 revolutionized the field of diagnostic science by enabling the production of monoclonal antibodies (MAbs) that recognize specific antigens to become a standard task. MAbs recognize single epitopes, are highly specific, can be produced against almost any antigen, and can be homogenously produced in unlimited quantities.[39] MAbs are routinely used in diagnostic techniques such as immunohistochemistry (IHC), enzyme linked immunosorbent assay (ELISA), immune-positron emission tomography (immunoPET), flow cytometry, and many others. They enable the detection of cancer and infectious disease and monitoring of biomarkers, and they have quickly become one of the most critical reagents in academic, industrial, and clinical diagnostic science.

The Clinical Need for Extracellular Vesicle Diagnostics in Human Cancer

Extracellular Vesicles (EVs) facilitate intercellular communication, serve as disease biomarkers, and prepare pre-metastatic niches for various cancers.[40–42] EVs transport lipids, proteins, and

RNA and range in diameter from approximately 40 nm-10 μm.[42] One of the most well-studied subclasses of EVs are exosomes. Exosomes are approximately 40-130 nm, are found in bodily fluids, and originate from intraluminal budding of the endosomal compartment in multivesicular bodies that then fuse with the plasma membrane and release exosomes into the extracellular environment.[40,42] Exosomes promote cancer progression by functioning as mediators of intracellular communication between tumors and distant tissues and transfer bioactive molecules between tumors and the tumor microenvironment.[40,42,43] The messages that are conveyed through cancer cell derived exosomes are under extensive investigation.[41,42,44,45] One promising analyte is the epidermal growth factor receptor (EGFR). EGFR is estimated to be overexpressed in 60-80% of colorectal cancer (CRC) tumors and is associated with poor prognosis.[46] Moreover, EGFR over expression is reflected in the content of EVs secreted from multiple cancers.[40,47,48] Thus, understanding the biological implications of EGFR+ EVs is of great importance for CRC and other EGFR driven cancers.

The Physical Properties of EVs Enable Centrifugation-Based Purification Methods

EVs are secreted membranous particles produced by most eukaryotic cells that are heterogenous in size, composition, and biogenesis. They have been shown to transport signaling molecules that facilitate intracellular communication, coagulation, and other specialized physiological processes. EVs are normally present in tissues throughout the body, but a significantly higher number of them are produced by human cancer cells.[44,45] Knowledge of the physical properties of extracellular vesicles has also proven useful for developing methods to isolate them from biological samples. EVs are commonly isolated from biofluids via ultracentrifugation and high-resolution density gradient fractionation, a technique that separates particles from a solution

based on particle size and density.[49] Although this method is effective at separating non-membranous nanoparticles such as exomeres and vault particles from subpopulations of EVs, it is labor intensive and is associated with low signal to noise ratio of downstream analyses because of confounding EVs derived from miscellaneous cells.[50] Thus, inclusion of purification methods that utilize affinity based separation in the sample processing workflow is necessary to isolate cancer derived EVs from those produced by healthy tissue.

The Need for Improved Affinity-Based Purification of EVs

In addition to ultracentrifugation, several strategies utilizing liquid chromatography and microfluidics have been developed to isolate EV subtypes based on size. Liquid chromatography utilizing size exclusion and molecular weight cutoff columns can efficiently separate EVs from free protein and other contaminants in biofluids but is subject to the same signal confoundment issue as ultracentrifugation and also significantly dilutes collected EVs due to the large volume of mobile phase required to operate the columns.[51] Microfluidic strategies to isolate EVs are rapidly emerging, but they are limited by low sample processing speeds, non-intuitive operation of microfluidic systems, clogging, and shear-stress induced damage to EVs.[52] Thus, purification methods that preferentially isolate exosomes possessing tumor-specific biomarkers are desperately needed to improve our understanding of the role of tumor-derived EVs.

Affinity based separation methods rely on capture antibodies to isolate EVs based on the cargo that they carry. Superparamagnetic beads decorated with capture antibodies are commonly used to isolate EVs from biological samples, because they significantly reduce the difficulty and time associated with purification. However, these magnetic particles remain linked to collected EVs after capture, which limits the scope of downstream analyses.[50] Several destructive methods, such as modulating the pH to disrupt antibody binding and lysing EVs with detergents,

can be used to liberate EV cargo for identification, but these methods can result in denaturing of protein cargo and disruption of the EV membrane. However, in order to understand the heterogeneity of EVs, improved superparamagnetic capture beads that enable non-destructive release of purified EVs must be developed so that single vesicle analysis techniques such as fluorescence activated vesicle sorting (FAVS) can be employed.[40]

Antibody Conjugation Mechanisms Improve Nanoparticle Drug Delivery and the Purification of Extracellular Vesicles

Great advances have been made in the field of drug delivery and EV analysis by incorporating targeting antibodies into the design of drug delivery vehicles and EV isolation reagents. A variety of antibody conjugation methods exist for these purposes but not all are well suited for each application. Streptavidin-avidin binding is one of the strongest non-covalent binding interactions that exists naturally.[53] The high binding affinity for biotin is accompanied by streptavidin's resistance to heat, denaturants, and proteolysis. These advantageous properties have enabled successful conjugation of targeting antibodies to drug delivery vehicles.[54] However, avidin and streptavidin conjugation systems have previously been shown to be immunogenic and could consequently exacerbate the inflammatory immune environment if used for drug delivery in the context of autoimmunity.[55]

Antibody conjugation mechanisms utilizing copper-free "click" chemistry reactions have been developed in order to enable rapid, durable antibody conjugation for use in physiological environments. Several FDA approved antibody-drug conjugates, such as Brentuximab vedotin and Trastuzumab emtansine, utilize maleimide-thiol conjugation chemistry to enable targeted delivery of chemotherapies to cancer cells.[56] Maleimide groups specifically react with thiols originating from disulfide bonds found in the hinge region of antibodies. Whole antibodies or

$F(ab')_2$ antibody fragments that have had the majority of the Fc region removed are exposed to reducing reagents such as dithiothreitol (DTT) to break the disulfide bonds and expose thiols for binding with maleimide. Although in the absence of excess thiols this linkage is stable, maleimide-thiol linkages suffer from thiol substitution during prolonged exposure to environments such as plasma, which contains high concentrations of excess thiols.[56,57] Nevertheless, specialized versions of maleimide have been developed to mitigate thiol substitution concerns.[57] Thus, maleimide-thiol conjugation of antibodies is most appropriate for antibody targeted drug delivery applications, because it ensures correct orientation of the antigen binding sites on the antibody that do not possess thiol groups.

Dibenzocyclooctyne (DBCO)-azide is another form of copper-free "click" chemistry that is widely used for antibody conjugation. Before conjugation to azide containing species, DBCO-N-hydroxysuccinimidyl (NHS) ester reagents must be conjugated to primary amines in the antibody. Unlike maleimide, DBCO-azide reactions involve the primary amines of antibody structures which are found in both the hinge region and antigen binding sites. Consequentially, this can render some antigen binding sites useless. DBCO-azide conjugations are stable and not susceptible to the same thiol substitutions that can remove maleimide-thiol conjugated antibodies from drug delivery vehicles. Unfortunately, it is well known that residual azides can be toxic to human cells.[58] Thus, DBCO-azide antibody conjugation chemistry is most appropriate for targeted EV purification where cellular toxicity is not a concern and exposure to the thiol-rich environment of plasma is expected.

SPECIFIC AIMS

This research addresses challenges in two distinct areas which are unified through the implementation of antibody conjugates that provide novel solutions for each challenge. The overall goals of this work are to enable targeted immunosuppression of $CD4^+$ T follicular helper (Tfh) cells and purification of $EGFR^+$ cancer associated extracellular vesicles. Although each solution is tailored for the specific application in which it is needed, the antibody conjugation methods developed throughout these studies build upon each other and guide the design of each unique conjugate. Together, the antibody conjugates developed in these studies will enable targeted delivery of Egm to $CD4^+$ T cells as well as improved immunocapture of cancer associated EVs.

Specific Aim 1: Develop and Characterize $CD4^+$ T cell Targeting Nanoparticles for Targeted Delivery of Eggmanone

Egm is insoluble in aqueous solutions, and therefore requires a rationally designed delivery vehicle to enable intravenous injection. Furthermore, delivery of small molecule drugs to T cells in general is a challenging task, because their low phagocytic activity prevents significant uptake of nanoparticle delivery vehicles. In order to overcome both Egm's solubility concerns and the low phagocytic potential of T cells, PEGylated PLGA nanoparticle delivery vehicles capable of hydrolytic release will be formulated. Empty, Eggmanone loaded, and fluorescent PEGylated PLGA nanoparticles with similar physicochemical properties will be synthesized. Particle size, zeta potential, drug loading, drug release rate, reactive chemistry, biocompatibility, and inhibition of helper T cell activation will be characterized to evaluate the drug delivery performance of PEGylated PLGA nanoparticles. Additionally, we will employ maleimide-thiol mediated conjugation of CD4 targeting F(ab') antibody fragments to enable targeted delivery of Egm on the surface of $CD4^+$ T cell membranes. This approach will ensure correct presentation of

the antibody fragment for receptor binding, bypass the inability of T cells to internalize nanoparticles via professional phagocytosis, reduce bioconjugate chemistry-associated immunorecognition and clearance, and minimize the overall size of the decorated delivery system relative to surface functionalization using a complete antibody. The optimal antibody conjugation chemistry and nanoparticle formulation parameters for Egm delivery to $CD4^+$ T cells will be determined from these results to enable specific immunosuppression of $CD4^+$ T cells.

Specific Aim 2: Functionalize Superparamagnetic Microparticles with Removable Targeting Antibodies for Magnetic Purification of Cancer Associated EVs

Epidermal growth factor receptor (EGFR) is estimated to be overexpressed in 60-80% of colorectal cancer tumors and is associated with poor prognosis.[46] Moreover, EGFR overexpression is reflected in the content of EVs secreted from multiple cancers and is thus a critical analyte for understanding the role of $EGFR^+$ cancer associated EVs.[40,47,48] Although paramagnetic microparticles, or immunocapture beads, are commonly used to isolate EVs from biological samples to eliminate the need for ultracentrifugation, there are no commercial options that enable nondestructive release of captured EVs for downstream analysis. In order to enable the capture and non-destructive release of $EGFR^+$ EVs, restriction-enzyme cleavable cetuximab-DNA conjugates will be synthesized. Cy3 fluorescent, heterobifunctional dsDNA linkers with dual restriction enzyme cleavage sites on either side of the Cy3 label will be conjugated to cetuximab capture antibodies via copper-free "click" chemistry. The physicochemical properties and electrophoretic mobility of cetuximab-DNA conjugates will be characterized to confirm DNA conjugation. Cetuximab microparticles (cetuximab-MPs) will be fabricated by conjugated cetuximab-DNA to streptavidin coated, superparamagnetic Dynabeads. The conjugation

efficiency and restriction enzyme-mediated release of cetuximab-DNA conjugates will be verified to demonstrate selective transfer of the Cy3 label and cleavage of dsDNA linkers. $EGFR^+$ EVs will be captured with cetuximab-MPs from increasingly complex biological samples to demonstrate the capture, labeling, and non-destructive release of EVs intended for single EV analysis.

CHAPTER 2

PEGYLATED PLGA NANOPARTICLE DELIVERY OF EGGMANONE FOR T CELL MODULATION: APPLICATIONS IN RHEUMATIC AUTOIMMUNITY

Reprinted with permission from:

Haycook CP, Balsamo JA, Glass EB, Williams CH, Hong CC, Major AS, Giorgio TD. PEGylated PLGA Nanoparticle Delivery of Eggmanone for T Cell Modulation: Applications in Rheumatic Autoimmunity. International Journal of Nanomedicine. 2020. 15. 1215-1228. DOI: 10.2147/IJN.S234850.[59]

ABSTRACT

Background: Helper T cell activity is dysregulated in a number of diseases including those associated with rheumatic autoimmunity. Treatment options are limited and usually consist of systemic immune suppression, resulting in undesirable consequences from compromised immunity. Hedgehog (Hh) signaling has been implicated in the activation of T cells and the formation of the immune synapse, but remains understudied in the context of autoimmunity. Modulation of Hh signaling has the potential to enable controlled immunosuppression but a potential therapy has not yet been developed to leverage this opportunity.

Methods: In this work we developed biodegradable nanoparticles to enable targeted delivery of Eggmanone (Egm), a specific Hh inhibitor, to $CD4^+$ T cell subsets. We utilized two FDA-approved polymers, poly(lactic-co-glycolic acid) and polyethylene glycol, to generate hydrolytically degradable nanoparticles. Furthermore, we employed maleimide-thiol mediated

conjugation chemistry to decorate nanoparticles with anti-CD4 F(ab') antibody fragments to enable targeted delivery of Egm.

Results: Our novel delivery system achieved highly specific association with the majority of $CD4^+$ T cells present among a complex cell population. Additionally, we have demonstrated antigen specific inhibition of $CD4^+$ T cell responses mediated by nanoparticle formulated Egm.

Conclusion: This work is the first characterization of Egm's immunomodulatory potential. Importantly, this study also suggests the potential benefit of a biodegradable delivery vehicle that is rationally designed for preferential interaction with a specific immune cell subtype for targeted modulation of Hh signaling.

Keywords: Advanced delivery systems. Eggmanone. Autoimmunity. Controlled release.

INTRODUCTION

Helper T cell activity is dysregulated in a variety of diseases for which rheumatic autoimmunity is a prime example. Rheumatic autoimmune diseases preferentially affect women, and are characterized by general pathology characteristics including inappropriate activation of the immune system, resulting in systemic inflammation within connective tissues including cartilage, joint synovium, and the skin.[3] With the exception of rheumatoid arthritis, targeted therapeutic options are limited, and treatment consists mainly of chronic, systemic delivery of immunosuppressive and anti-inflammatory agents that can result in compromised immunity, premature cardiovascular disease and osteoporosis.[3]

Central to T cell and B cell cooperation is their physical interaction at the immune synapse (IS). The IS is an area of concentrated signaling at the point where the membranes of the T cell and antigen presenting cell (APC) make physical contact. Formation of the IS between CD4+ T cells and B cells is critical for the production of autoantibodies that potentiate the

systemic inflammation of connective tissues in rheumatic autoimmunity. IS formation involves intricate reorganization of the cytoskeleton facilitated by the polarization of the microtubule-organizing center (MTOC), as well as, actin partitioning and repositioning of the Golgi apparatus below the surface of the IS.[60]

MTOC reorganization and polarization to the IS is dependent on Hedgehog (Hh) signaling, a pathway that is traditionally associated with primary cilia in nonhematopoietic cells.[61,62] De la Roche et al demonstrated that inhibitors of Hh signaling can disrupt the IS and the ability of $CD8^+$ T cells to become activated and lyse antigen-presenting targets.[61] Overactivation of Hh signaling in the thymus can lead to decreased negative selection and the escape of autoreactive T cell clones.[63] Additionally, Hh signaling proteins are able to provide co-stimulatory effects to $CD4^+$ T cells in the periphery that promote proliferation and cytokine production.[64] Furthermore, others have demonstrated that the MTOC in $CD4^+$ T cells is reoriented to face towards the IS junction with B cells in an antigen dependent manner.[65] Therefore, specific disruption of the IS via targeting the Hh-regulated MTOC may represent a potential new, specific therapeutic strategy to disrupt autoantibody production in rheumatic autoimmunity that could eliminate the need for chronic usage of immunosuppressants and glucocorticoids.

Eggmanone (Egm) is a small molecule inhibitor of the Hh signaling pathway that was discovered at Vanderbilt University.[31] Unlike commercially available small molecule Hh inhibitors that inhibit the upstream G protein-coupled receptor Smoothened (SMO) and are susceptible to acquired resistance, Egm antagonizes phosphodiesterase 4 (PDE4), a downstream regulator of Hh gene transcription. Importantly, unlike other PDE4 inhibitors, Egm inhibits PDE4 by raising cyclic AMP locally at the basal body, instead of raising total cellular cyclic

AMP content.[31] If delivered to $CD4^+$ T cells, Egm could potentially inhibit autoimmune lymphocyte activation through suppression of Hh mediated IS formation in $CD4^+$ T cells. However, Egm is also extremely hydrophobic, leading to rapid excretion and ineffective intravenous administration if a rationally designed delivery vehicle is not utilized.[66]

Specific delivery of small molecule drugs to T cells is a challenging task due to their low phagocytic activity. Previous attempts to specifically deliver hydrophobic immunomodulatory cargo to $CD4^+$ T cells have utilized several poly(lactic-co-glycolic acid) (PLGA) nanoparticle formulations to create localized drug delivery depots at the cell surface. McHugh *et al.* conjugated biotin labeled whole anti-CD4 antibodies to avidin coated PLGA nanoparticles.[54] Although they were able to achieve high CD4 targeting specificity *ex vivo*, avidin and streptavidin conjugation systems have previously been shown to be immunogenic, and could, therefore, exacerbate the inflammatory immune environment associated with autoimmunity.[55] Additionally, conjugation of whole targeting antibodies that contain foreign fragment crystallizable (Fc) regions can lead to rapid clearance of nanoparticles in systemic circulation via Fc receptor mediated recognition by the reticuloendothelial system (RES).[67] Cao *et al.* conjugated anti-CD4 antibody fragments to PLGA nanoparticles coated with polyethylene glycol (PEG) conjugated lipids. This formulation decreased the potential for opsonization mediated clearance by the RES through incorporation of hydrophilic PEG[67], and also provided tunable control of nanoparticle surface charge via mixing of cationic and anionic lipids in the surface coating. Although this formulation incorporated several design elements to improve *in vivo* pharmacokinetics by bypassing RES mediated nanoparticle clearance mechanisms, the antibody fragmentation method utilized resulted in conjugation of some non-functional fragments that reduced overall CD4 targeting specificity.[68]

In this work, we employ a therapeutic approach involving hydrolytically degradable nanoparticles that specifically bind to $CD4^+$ helper T cell subsets to form membrane-localized drug delivery depots, bypassing their inability to perform professional phagocytosis. We utilized two FDA-approved polymers, PLGA and PEG, to generate hydrolytically degradable nanoparticles capable of providing rapid release rates of Egm and decreased non-specific delivery to off-target immune cells. Furthermore, we employed maleimide-thiol mediated conjugation of CD4 targeting F(ab') antibody fragments to enable sustained, targeted delivery of Egm on the surface of $CD4^+$ T cell membranes. This approach ensures correct presentation of the antibody fragment for receptor binding, reduces bioconjugate chemistry-associated immunorecognition and clearance, and minimizes the overall size of the decorated delivery system relative to surface functionalization using a complete antibody. To the best of our knowledge, this work represents the first characterization of Egm's immunomodulatory effects and its formulation as a potential nanomedicine for targeted immunomodulation of $CD4^+$ T cells.

EXPERIMENTAL

Cell Culture

8-10 week old female mice (FVB (FVB/NJ stock no: 001800), C57BL/6J stock no: 000664, and OT-II (B6.Cg-Tg(TCRαTCRβ)425Cbn/J stock no: 004194), The Jackson Laboratory) were used for all experiments in order to reflect the higher incidence rates of rheumatic autoimmunity in females. All animal care was conducted in accordance with local and federal guidelines evaluated by the Association for Assessment and Accreditation of Laboratory Animal Care (AAALAC) and an animal protocol (M1700021) approved by the Vanderbilt Institutional Animal Care and Use Committee. Whole splenocyte cultures were derived from spleens

harvested from 8-10-week-old female FVB mice, for evaluation of nanoparticle toxicity, C57BL/6J mice, for evaluation of nanoparticle targeting specificity, and OT-II mice, for evaluation of therapeutic efficacy. Mice were euthanized and spleens were immediately harvested and placed in ice-cold T cell media (RPMI-1640 supplemented with 10% fetal bovine serum, penicillin/streptomycin, 55 mM 2-mercaptoethanol, 1 mM pyruvate, 2 mM glutamine and non-essential amino acids). Spleens were manually dissociated using 40-micron cell strainers (Fisher Scientific, nylon mesh) and the resulting cell suspension was centrifuged at 1500 rpm for 7 min at 4 °C. The supernatant was decanted and residual cell pellets were broken up. Red blood cells in the resulting cell suspension were lysed by adding 900 uL of microbiology grade water (Corning) followed by 100 µL of 10X PBS (Sigma) while vortex mixing.

Evaluation of T cell Activation and Cytokine Production

Whole splenocytes were seeded in standard 96-well plates at 100,000 cells/well and stimulated for 72 hours with various concentrations of whole ovalbumin or ovalbumin peptide aa323-339 ($OVA_{323-339}$). Interferon gamma (IFN-γ) production was measured in culture supernatants by specific ELISA (BD OptEIA, Catalogue # 551866) after incubation with either dimethyl sulfoxide (DMSO) or Egm dissolved in DMSO. T cell activation was evaluated by flow cytometry.

Nanoparticle Formulation

PEGylated PLGA nanoparticles were prepared using oil-in-water emulsion mediated by sonication. PLGA 50:50 lactic acid (LA):glycolic acid (GA) (10 kDa)-PEG(5 kDa)-maleimide (Nanosoft Polymers, lot number 27910051517) or PLGA 50:50 LA:GA(10 kDa)-PEG(5 kDa)-methyl (Nanosoft Polymers, lot number 275310050324) was added to PLGA 50:50 LA:GA (10

kDa, Durect corporation, lot number 902-82-1) at 25% (mass PLGA-PEG/mass PLGA) and dissolved in dichloromethane (DCM) at 25 mg polymer/mL DCM. Hydrophobic Egm and/or 1,1'-Dioctadecyl-3,3,3',3'-Tetramethylindodicarbocyanine, 4-Chlorobenzenesulfonate Salt (DiD)[69] cargo was incorporated into the oil phase prior to sonication for encapsulation within PEGylated PLGA nanoparticles. Lyophilized Egm was dissolved directly in DCM at 4% (mass Egm/mass total polymer) prior to dissolving polymers. 2uL of DiD dissolved in DMSO at 2mg/mL was added after polymers were fully dissolved for fluorescently labeled materials. Resulting solutions were vortex mixed and transferred to ice-cold 0.25% (w/v poly(vinyl alcohol) in deionized water) surfactant solution. Emulsification was achieved using a Fisher Scientific Sonic Dismembrator (Power level 3, 3 subsequent 10 seconds on, 20 seconds off cycles on ice). The resulting nanoparticle suspension was stirred for 3 hours to evaporate residual DCM, and allow nanoparticles to harden. Excess poly(vinyl-alcohol) and residual free Egm and DiD were removed via sonication in deionized water and centrifugation (20,000 g, 10 min). Recovered nanoparticles were suspended in either deionized water for chemical analysis, or 3% aqueous trehalose (Sigma) solutions for all other applications. Nanoparticles were filtered with 5 µm (Pall, acrodisc supor membrane) followed by 0.45 µm (ThermoFisher, PTFE) syringe filters prior to freezing (-80 °C) overnight and lyophilization (-40 °C, 0.2 mbar, 72 hours) using a Labconco Freezone 4.5. All nanoparticle formulation variables are summarized below (Table 2.1).

Table 2.1 Summary of nanoparticle formulation variables

Composition	Cargo	Conjugate
PLGA + PLGA-PEG-maleimide	Empty	Unconjugated
PLGA + PLGA-PEG-methyl	DiD	Anti-CD4 F(ab')
	Egm	Isotype control F(ab')

Abbreviation: PLGA, poly(lactic-co-glycolic acid); PLGA-PEG-methyl, poly(lactic-co-glycolic acid)-polyethylene glycol-methyl; PLGA-PEG-maleimide, poly(lactic-co-glycolic acid)-polyethylene glycol-maleimide; DiD, 1,1'-Dioctadecyl-3,3,3',3'-Tetramethylindodicarbocyanine, 4-Chlorobenzenesulfonate Salt; Egm, Eggmanone.

Characterization of Egm-Loaded Nanoparticle Encapsulation Efficiency

Egm and Egm-loaded nanoparticle (Egm-NP) trehalose-free lyophilizate were dissolved in DMSO for evaluation of peak Egm absorbance at 323 nm by UV/Vis spectroscopy. At least three technical replicates of 180 uL volumes were prepared for each sample. Measurements were performed in UV-transparent 96-well plates (Nunc, 96-well UV microplates) using a Biotek M1000Pro plate reader. Measured Egm-NP absorbance values were adjusted to remove the contribution of PLGA by subtracting absorbance values of matched concentration empty particles. Encapsulation efficiency was calculated as the ratio of the loading capacity determined by UV/VIS spectroscopy to the theoretical loading capacity. Loading capacity was defined as the ratio of Egm mass to the total mass of polymer in the formulation.

Characterization of Nanoparticle Size, Zeta Potential, Reactive Chemistry, and Release Rate

Hydrated nanoparticle size and zeta potential were measured using nanoparticle tracking analysis (Malvern Panalytical, Nanosight NS 300) and laser doppler electrophoresis (Malvern Panalytcal, Zetasizer Nano ZS), respectively. Percent relative standard deviation (%RSD) of each formulation was calculated according to Malvern's recommendations.[70] Maleimide reactive end chemistry was verified using 1H nuclear magnetic resonance spectroscopy (Bruker, 400MHz). At least 5mg of trehalose-free nanoparticle lyophilizate was dissolved in 600 uL deuterated

chloroform (Sigma) for NMR sample preparation. DiD release rate was measured using a Biotek M1000Pro plate reader. Nanoparticle lyophilizate was resuspended in 1X PBS and incubated at 37 °C while shaking for up to 5 days. Resuspension times were staggered so that all release samples were collected at once. Following incubation, nanoparticles were centrifuged (20,000 g, 10 min), and supernatant was decanted. Unreleased DiD was measured after dissolving collected pellets in DMSO. Amount released was quantified by normalizing DiD fluorescence of release samples to 0-hour release controls.

Evaluation of Nanoparticle Morphology and Egm Localization

Dehydrated nanoparticle morphology was evaluated using transmission electron microscopy (TEM) (Philips/FEI T-12). Freshly made nanoparticles suspended in deionized water were incubated at room temperature on poly-l-lysine-coated TEM grids (formvar coated stabilized with carbon film, Electron Microscopy Sciences) for five minutes before wicking away excess liquid with filter paper. No contrast agents were utilized for TEM imaging. Egm localization within nanoparticles was investigated using ImageJ analysis and energy-dispersive X-ray spectroscopy. Intensity profiles of equal magnification TEM images were generated using the line profile tool in ImageJ (magnification = 52000X, line width = 20 nm). Intensity profiles for each image were normalized to the average background intensity surrounding each nanoparticle. TEM imaging sample preparation was also utilized for elemental analysis of nanoparticles by scanning electron transmission energy-dispersive X-ray spectroscopy (STEM-EDS) (FEI Tecnai Osiris). Nanoscale X-ray element mappings generated from STEM-EDS spectral data were used to determine the spatial distribution of Egm within PEGylated PLGA nanoparticles. High angle annular dark-field images served as a reference for nanoparticle area among elemental mappings.

Evaluation of Egm-Loaded Nanoparticle Biocompatibility and Immunomodulatory Potential

Whole splenocytes were seeded in standard (for evaluation of therapeutic efficacy) or black-walled (for evaluation of biocompatibility) 96-well plates at 100,000 cells/well prior to adding nanoparticle treatments. Egm-NP and empty nanoparticle (empty-NP) lyophilizate was resuspended in T cell media (described above) via vortex mixing and water bath sonication immediately prior to use. Standard media was replaced with nanoparticle containing media, and cell viability was evaluated 72 hours later by Celltiter glo assay (Promega). IFN-γ production was evaluated 72 hours after stimulation with 50 µg/mL ovalbumin and nanoparticles via ELISA (BD OptEIA, Catalogue # 551866).

Antibody Fragment Conjugation to Nanoparticles

Anti-CD4 (clone GK1.5, Bio X Cell) and isotype control (clone LTF-2, Bio X Cell) $F(ab')_2$ antibody fragments were generated using the Pierce $F(ab')_2$ Prep kit (ThermoFisher catalogue # 44988). F(ab') antibody fragments were generated from $F(ab')_2$ fragments according to previously published methods.[71] Disulfide bonds between antibody fragments were reduced using 0.5 mM DTT in 1X PBS for 30 minutes at room temperature. Excess DTT was removed from fragments using 7K MWCO zeba spin desalting columns (ThermoFisher catalogue # 89882). Reduced antibody fragment concentration was quantified using nanodrop (Mettler Toledo UV5 nano) as recommended by ThermoFisher (280 nm absorbance, molar extinction coefficient = 1.4). Fragments were added to resuspended nanoparticles at a concentration of 12.5 ug antibody per $1.49 \times 10^9 \pm 1.89 \times 10^8$ resuspended nanoparticles (determined by Nanosight) in 1X PBS according to previously published methods.[71] Resulting solutions were prepared with a final volume of 1 mL and shaken for 2 hours in 2 mL microcentrifuge tubes at room temperature

on a Fisher mini vortexer (speed 8) to initiate Maleimide-thiol antibody conjugation to nanoparticles.

Evaluation of Antibody-Conjugated Nanoparticle Targeting Efficacy

Targeting efficacy was evaluated using DiD (Invitrogen, catalogue # D7757)-loaded fluorescent nanoparticles (DiD-NPs) with surface conjugated antibody fragments. Whole splenocyte cultures were incubated for 30-minutes with DiD-loaded, antibody fragment decorated nanoparticles suspended in PBS via flow cytometry (250,000 cells per $7.45 \times 10^7 \pm 9.45 \times 10^6$ NPs/mL) unless otherwise indicated.

Flow Cytometry

Product information for the fluorescently labeled antibodies used in the flow cytometry staining protocols within this work are provided in the following format: (surface marker-fluorochrome, clone, company). Flow cytometry staining probes used consisted of: (TCR-β-APC, H57-597, BD), (CD4-PE-Cy7, GK 1.5, BD), (CD4-PerCP, RM4-5, Tonbo), (CD8a-APC-Cy7, 53-6.7, Tonbo), (CD44-FITC, IM7, BD), (CD62L-PerCP, MEL-14, BD).

Cells were incubated with Fc block at 1:100 for 15 minutes at room temp in FACS buffer containing HBSS, 1% BSA, 4.17 mM sodium bicarbonate, and 3.08 mM sodium azide. Cells were labeled with an antibody cocktail consisting of either (TCR-β-FITC, CD4-PE-Cy7, CD44-FITC, CD62L-PerCP) or (CD4-PerCP, CD8a-APC-Cy7) in FACS buffer for 30 minutes on ice in the dark. Cells were washed and resuspended in 2% paraformaldehyde for analysis on a MACSQuant seven-color flow cytometer (Miltenyi Biotec); data were analyzed using FlowJo Single Cell Analysis Version 10.0.1.

Flow cytometry gating for T cell activation experiments involved selecting the lymphocyte population from forward scatter versus side scatter plots. TCR-β^+CD4^+ T cells were selected from TCR-β versus CD4 plots. Activated $CD4^+$ T cells were selected from CD44 versus CD62L plots. Flow cytometry gating for nanoparticle targeting experiments involved selecting the lymphocyte population from forward versus side scatter plots. $CD4^+$, $CD8^+$, and non-T cells were selected from CD4 versus CD8 plots. Corresponding nanoparticle$^+$ cell populations were then selected according to DiD staining intensity.

Statistical Analysis

All error bars represent standard error of the mean unless otherwise indicated. One or Two-way Analysis of Variance followed by multiple comparisons test were performed for most data presented here as indicated, and statistical significance was defined as $p < 0.05$. Statistical analyses were performed using Prism 7.04 (GraphPad Software).

RESULTS & DISCUSSION

Egm Inhibits $CD4^+$ T cell Activation and Cytokine Responses

A central hypothesis of this study is that targeted inhibition of Hh signaling could significantly reduce $CD4^+$ T cell activation in response to specific antigen. To test this hypothesis, OT-II whole splenocytes were incubated with increasing concentrations of whole OVA in the presence of unformulated Egm or an equivalent volume of DMSO (vehicle). At all OVA concentrations, Egm significantly inhibited $CD4^+$ T cell production of IFN-γ (Figure 2.1A). Using $OVA_{323-339}$, which eliminates the need for antigen processing, we demonstrated that Egm was a potent inhibitor of $CD4^+$ T cell cytokine responses, and its effects were dose dependent (Figure 2.1B). Significant reduction of IFN-γ was observed for Egm concentrations as low as 0.63 μM, and

IFN-γ was undetectable at concentrations above 2.5 μM (Figure 2.1B). After observing that Egm treatment suppressed helper T cell cytokine responses, we investigated whether Egm also suppressed T cell activation. OT-II splenocyte experiments utilizing $OVA_{323-339}$ were repeated and T cell activation was evaluated by flow cytometric analysis of T cell activation and memory markers (Figure 2.1C, D, and E). At concentrations of $OVA_{323-339}$ above 25 μg/mL, Egm significantly reduced the percent of helper T cell populations expressing the activation/memory phenotype $CD44^{hi}CD62L^{lo}$ (Figure 2.1D).[72] Additionally, Egm treatment significantly reduced expression of CD69, an additional T cell activation marker, for all concentrations of OVA tested when compared to DMSO controls (Figure 2.1E). Our results indicate that Egm treatment significantly inhibits $CD4^+$ T cell activation in the presence of specific antigen. Thus, for the first time, we have demonstrated the immunomodulatory effects of Egm on $CD4^+$ T cells and also highlighted its potential use as an immunosuppressive small molecule compound. However, Egm's *in vivo* utility is limited by its poor water solubility that necessitates the use of a rationally designed carrier to enable further investigation of its immunomodulatory potential.

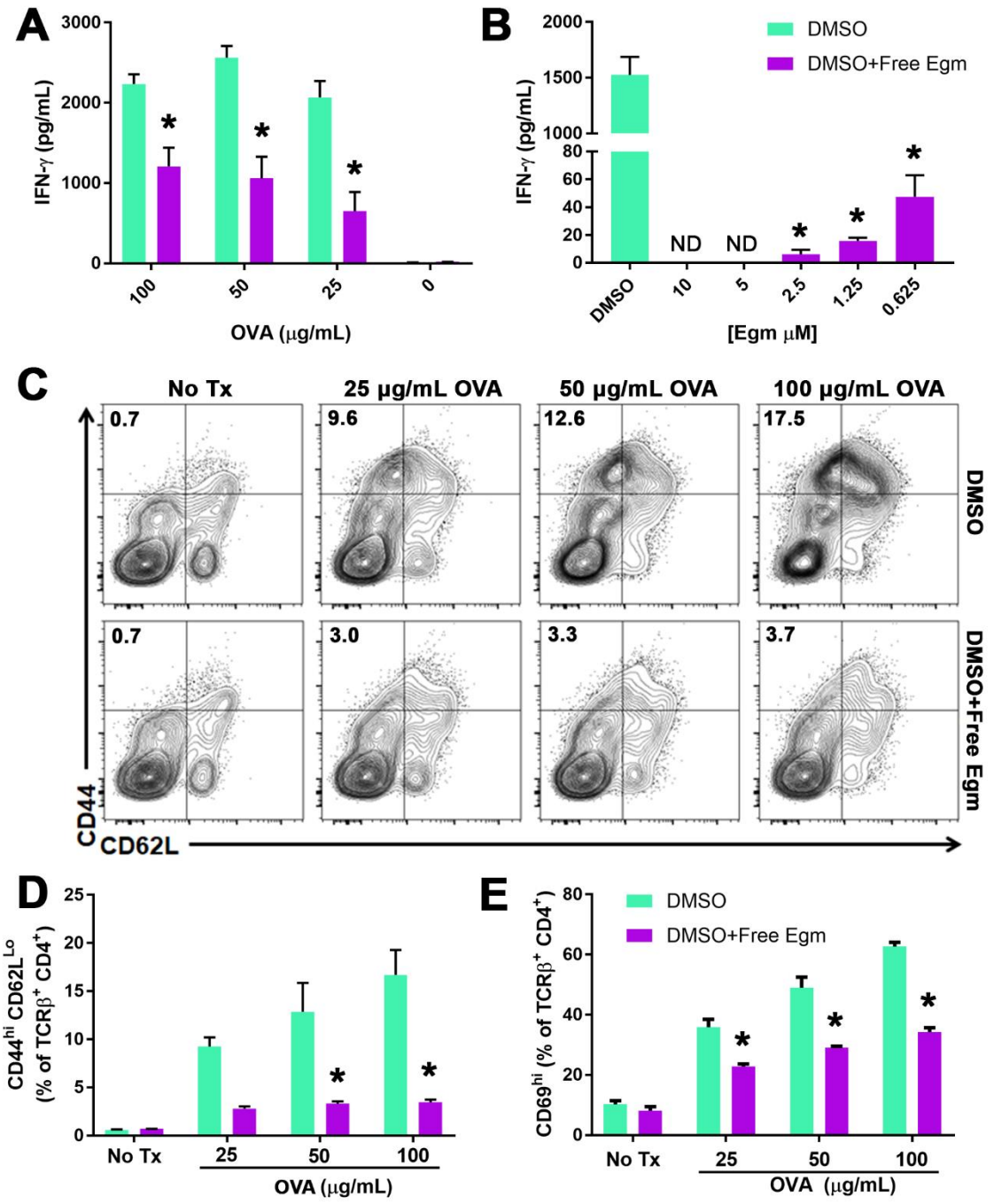

Figure 2.1 Egm inhibits $CD4^+$ T cell activation and cytokine responses.

Notes: (**A**) OT-II whole splenocytes were incubated with whole OVA protein at various concentrations for 72 hours in the presence of DMSO (vehicle) or 10 μM Egm in DMSO. (**B**) Egm dose response of OT-II whole splenocytes incubated with $OVA_{323-339}$ peptide (50 μg/mL) for 72 hours. IFN-γ concentration was measured via ELISA. (**C**) Representative flow cytometric analysis of OT-II whole splenocyte cultures incubated with $OVA_{323-339}$ peptide in the presence of

DMSO or 10 μM Egm in DMSO for 72 hours. T cell activation was evaluated by analysis of $CD44^{hi}CD62L^{lo}$ T cell populations (plots gated from $TCR\beta^{+}CD4^{+}$ T cells). (**D**) Quantification of $CD44^{hi}CD62L^{lo}$ T cell populations from 3 biological replicates. (**E**) Quantification of CD69 expression in the presence of Egm or DMSO from 3 biological replicates. The significance of the data was evaluated via ordinary One-way ANOVA with multiple comparisons test. (*P<0.05). **Abbreviations:** OVA, ovalbumin; DMSO, dimethyl sulfoxide; No Tx, no treatment.

Synthesis and Characterization of PEGylated PLGA Nanoparticles Loaded with Egm and DiD

Single oil in water emulsion and solvent evaporation strategies were utilized to synthesize PEGylated PLGA nanoparticles as a potential delivery vehicle for *in vivo* Egm administration (Figure 2.2). Egm and a fluorescent surrogate compound, DiD, were encapsulated in nanoparticles in order to investigate whether Egm could be efficiently packaged and delivered to $CD4^{+}$ T cells as a nanomedicine. Nanoparticle size and zeta potential were measured by nanoparticle tracking analysis and laser doppler electrophoresis, respectively. Because nanoparticle tracking analysis produces a population of single-particle size measurements, rather than hypothetical gaussian distributions of nanoparticle size[70], the polydispersity of each formulation was evaluated by calculating the %RSD. Egm encapsulation had no effect on particle size (Figure 2.2A, B, and C), %RSD (Figure 2.2D), or zeta potential (Figure 2.2E). Loading of DiD increased mean particle size and SD compared to all formulations, as well as, %RSD compared to select formulations (Figure 2.2A, C, and D). Differences in particle size and polydispersity measures associated with DiD loading may be an artifact caused by fluorescent excitation of the DiD inside nanoparticles by the 642 nm laser utilized in nanoparticle tracking analysis measures. Importantly, lyophilization did not significantly increase the particle size of any formulation, and the size of all lyophilized formulations were statistically similar. Lyophilization of nanoparticle formulations enabled prolonged shelf-life and “as-needed” usage

of all formulations developed in this study. All formulations had zeta potentials near -42 mV, hydrodynamic diameters near 200 nm, and narrow size distributions with %RSD below 40. Therefore, particle suspensions were monodisperse, and the appropriate size to provide passive accumulation in the spleen[34,73,74] in addition to T cell mediated transport to the spleen and lymph nodes.[71]

Zeta potential and particle size are both known to be important factors that influence the circulation half-life of nanoparticles, and these factors were unaffected by Egm loading.[33] Additionally, the zeta potential of nanoparticle targeting systems has also been shown to significantly affect the potential of nonspecific binding due to electrostatic interactions with the cell membrane.[33] PLGA nanoparticles with cationic surface charges preferentially interact with negatively charged cell membranes irrespective of targeting ligand conjugation.[37] Conversely, nanoparticles with anionic surface charges similar to our formulations possess elevated specific binding interaction to $CD4^+$ T cells by reducing nonspecific electrostatic interactions with cell membranes, allowing conjugated targeting ligand binding affinity to dominate.[68] Additionally, nanoparticle formulations with cationic zeta potentials can lead to pro-inflammatory immune responses while those with anionic zeta potentials are associated with reduced immunogenicity and increased circulation potential.[38] Therefore, we have confidence that the measured zeta potentials of our three undecorated formulations (empty, Egm-loaded, and DiD-loaded), are well-suited for antibody fragment decoration and systemic $CD4^+$ T cell targeting applications in rheumatic autoimmunity.

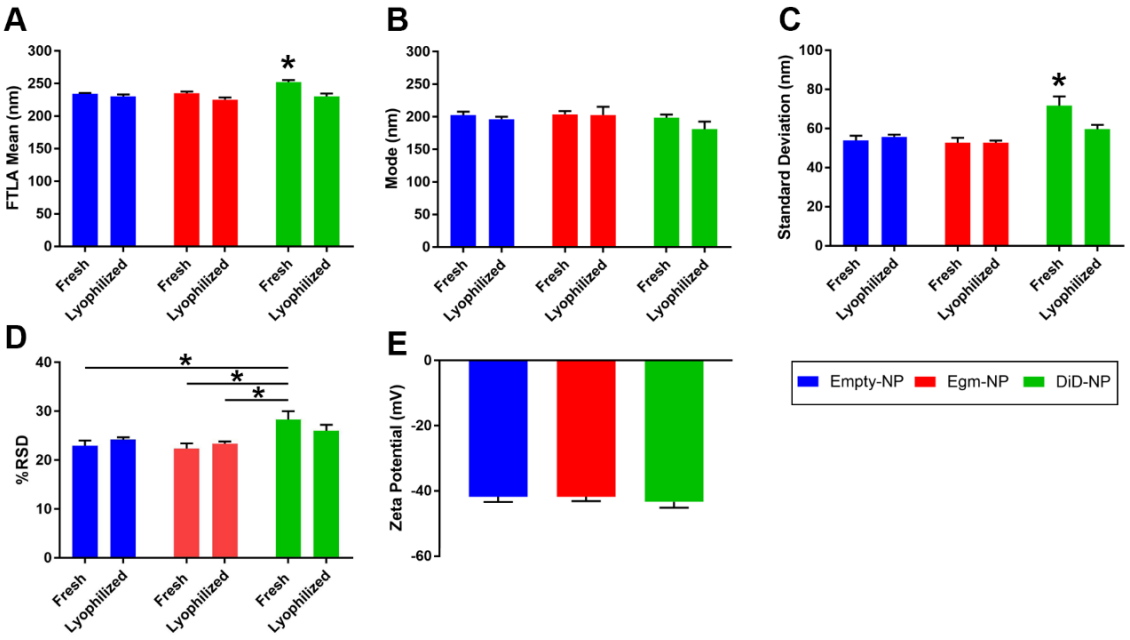

Figure 2.2 PEGylated PLGA nanoparticles retain physicochemical characteristics following Egm loading.
Notes: (**A**) FTLA mean hydrodynamic diameter of nanoparticles. (**B**) Mode of nanoparticle diameter distributions. (**C**) Standard deviation of nanoparticle diameters. (**D**) Calculated percent relative standard deviation of nanoparticle distributions (**E**) Zeta potential measures of lyophilized formulations. All measurements were performed in deionized water. All data shown represents the mean ± SEM of at least three independent batches for each formulation. The significance of the data was evaluated via ordinary One-way or Two-way ANOVA with multiple comparisons test. (*P<0.05).
Abbreviations: FTLA, finite-track length adjusted; empty-NP, empty nanoparticle; Egm-NP, Eggmanone-loaded nanoparticle; DiD-NP, DiD-loaded nanoparticle; SEM, standard error of the mean.

We verified that the presence of maleimide reactive end-chemistry on PEGylated PLGA nanoparticle coronas was unaffected by Egm loading through 1H nuclear magnetic resonance spectroscopy of nanoparticle formulations made with either PLGA-PEG-maleimide or PLGA-PEG-methyl. NMR spectra of nanoparticles made with PLGA-PEG-maleimide (Supplemental Figure A.1B and C) exhibited a peak at 6.7 ppm, characteristic of maleimide[75], that was not present in the spectra of particles made with PLGA-PEG-methyl instead (Supplemental Figure A.1A). Additionally, NMR spectra of nanoparticles loaded with Egm exhibited known

characteristic peaks of Egm[32] (Supplemental Figure A.1C) that, in addition to UV/VIS spectroscopy, confirmed the loading of Egm within nanoparticles. Egm encapsulation efficiency was 76.7 $\pm$ 11.1% (calculated from UV/VIS measures).

Emulsion Mediated Fabrication Localizes Egm in the Core of Spherical Nanoparticles

Dehydrated nanoparticle size and morphology was investigated via TEM imaging of unstained empty- and Egm-NPs on positively charged polylysine coated TEM grids (Figure 2.3A). Both nanoparticle formulations exhibited diameters in agreement with Nanosight measures (Figures 2.2A and B) and spherical morphology that is typical of emulsion mediated fabrication strategies. Interestingly, TEM imaging of Egm-NPs revealed a region of increased electron density in nanoparticle cores when compared to empty-NPs (Supplemental Figure A.2). This prompted further investigation of elemental distribution within nanoparticles via energy-dispersive X-ray spectroscopy.

The presence of sulfur, a unique element found only in the chemical structure of Egm in our formulations, was used to indicate the spatial distribution of Egm within nanoparticles. Analysis of STEM-EDS spectra revealed the presence of carbon, nitrogen, and oxygen peaks, corresponding to PLGA and PLGA-PEG-maleimide polymer components, in both particle formulations, while a sulfur peak was only present in Egm-NPs (Figure 2.3B).

Elemental mappings revealed a concentration of sulfur in the core of Egm-NPs, indicative of Egm loading, with little observable signal outside of the nanoparticle region (Figure 2.3C). In contrast, the sulfur signal observed in empty-NP elemental mappings was largely dispersed throughout the entire region of interest and, therefore, was presumed to be the result of shot-noise during signal collection (Figure 2.3D). Taken together with areas of increased contrast in TEM images of Egm-NPs, the concentration of sulfur within Egm-NPs provides evidence

suggestive of Egm localization in the nanoparticle cores mediated by emulsion mediated fabrication methods.

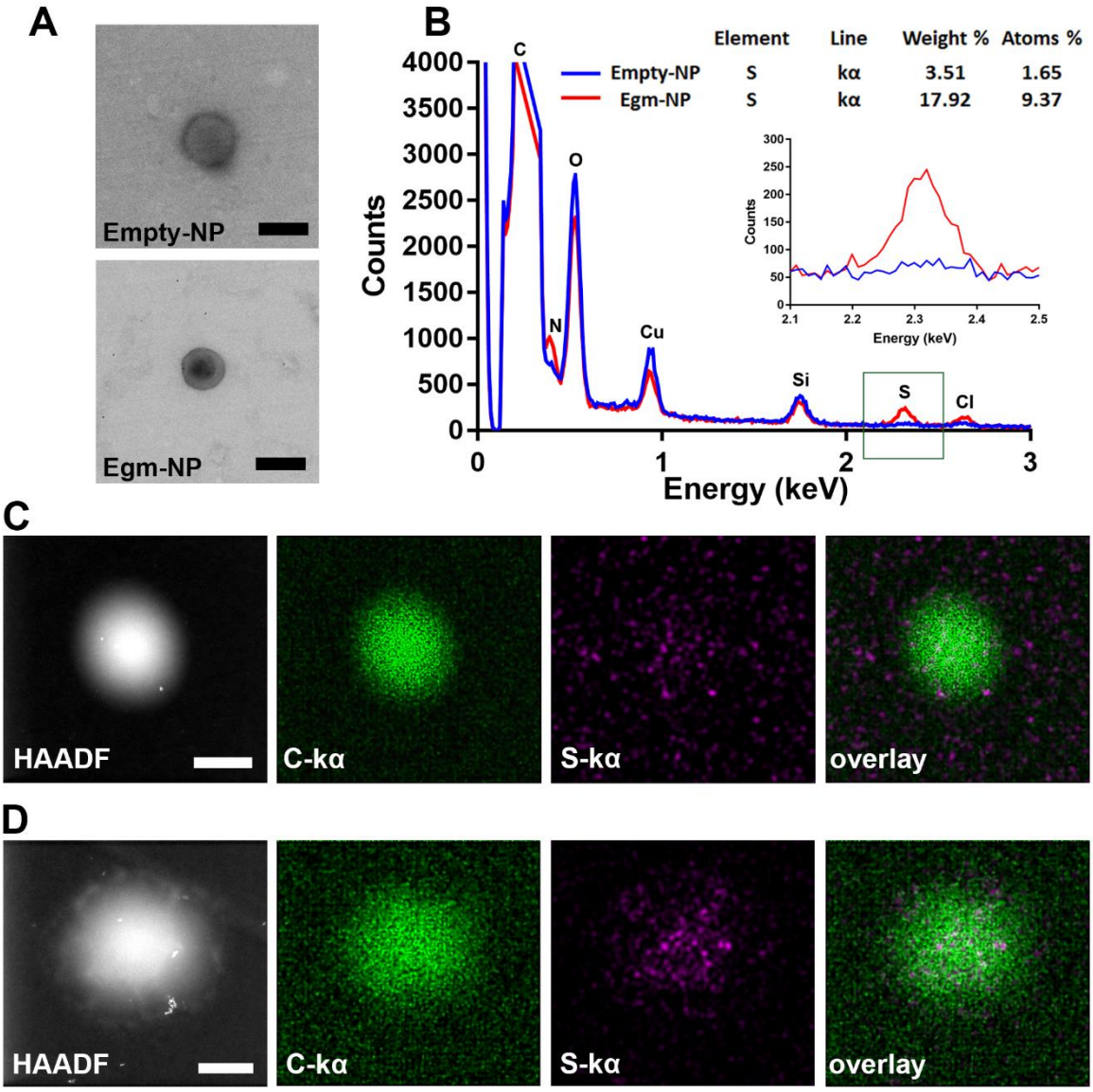

Figure 2.3 Emulsion mediated fabrication localizes Egm in nanoparticle cores.

Notes: (**A**) Transmission electron micrographs of empty and Egm-loaded nanoparticles. No negative staining was utilized. (**B**) Elemental analysis and quantification of sulfur weight % and atoms % within empty and Egm-loaded nanoparticles. Inset corresponds to the energy region within the green box. (**C**) Nanoscale X-ray element mappings of empty nanoparticle. (**D**) Nanoscale X-ray element mappings of Egm-loaded nanoparticle. All images representative of corresponding nanoparticle populations. All scale bars represent 200 nm.

Abbreviations: Empty-NP, empty nanoparticle; Egm-NP, Egm-loaded nanoparticle; HAADF, high angle angular dark field image; C, carbon; S, sulfur; O, oxygen; N, Nitrogen, Cu, copper; Si, silicon; Cl, chlorine; kα, K-alpha emission line.

Nanoparticle Formulated Egm Inhibits Antigen Specific $CD4^+$ T cell Cytokine Responses in a Therapeutically Relevant Timeframe

The use of low molecular weight PLGA with an equal molar ratio of lactic to glycolic acid in our formulation is intended to enable rapid release of Egm.[76] The release of Egm from nanoparticle formulations was investigated using fluorescent DiD in order to enable sufficient signal strength during release measurements. Lyophilized nanoparticles that were resuspended and incubated in PBS at 37 °C on an orbital shaker released 66.7% of DiD over the course of 5 days, and exhibited a characteristic burst release associated with low molecular weight, 50:50 (lactic acid:glycolic acid) PLGA equal to 32.0% within the first 24 hours (Figure 2.4A). The release kinetics we observed with DiD are expected to enable the efficacy of future potential therapeutic intervention strategies using Egm. The initial burst and controlled release periods appear suitable to address the lag phase of a secondary immune response to self-antigen generated by autoimmune memory cells. The lag phase of a secondary immune response is typically 2 to 5 days.[77] During this time, antigen presentation and subsequent isotype switching and differentiation of B cells into autoantibody-producing plasma cells, occurs in the germinal centers of secondary lymphoid organs. Although rheumatic autoimmune diseases are mainly thought of as antibody mediated diseases, the production of IgG antibodies, the isotype with the highest antigen affinity and plasma circulation potential, is a $CD4^+$ T cell dependent process that is regulated in germinal center responses. Thus, if a sufficient number of Egm-loaded nanoparticles with similar release kinetics could be targeted to the germinal centers during the lag phase, inhibition of plasma cell differentiation and autoantibody production could be

achieved on a sufficient timescale to serve as a viable therapeutic intervention strategy for rheumatic autoimmune diseases. Although we did not directly measure the release of Egm from our formulation due to concentrations below the detection limits of appropriate analytical chemistry instrumentation, we expect a similar and/or faster release profile since Egm is similarly hydrophobic, and has a significantly lower molecular weight than DiD, 416 Da compared to 1,052 Da, respectively.

After demonstrating that PEGylated PLGA nanoparticles could efficiently encapsulate and release Egm in a therapeutically relevant timeframe, we verified that the nanoparticle formulation of Egm was effective at inhibiting antigen specific inflammatory cytokine responses of $CD4^+$ T cells. IFN-γ is the hallmark cytokine produced by $CD4^+$ T follicular helper cells (Tfh) in the germinal center response that enables B cell production of high affinity, long circulating IgG antibody isotypes.[78] Inhibition of IFN-γ production by OT-II splenocytes stimulated with ovalbumin was measured 72 hours after incubation with Egm loaded and empty, undecorated nanoparticle formulations. For all concentrations of Egm evaluated, both free and nanoparticle formulations of Egm significantly inhibited the production of IFN-γ compared to media controls and no statistical difference was observed between nanoparticle-formulated and free Egm. No significant changes were observed for DMSO and blank nanoparticle vehicle controls (Figure 2.4B).

Acute toxicity of lyophilized Egm- and empty-NPs was evaluated *ex vivo* 72 hours after incubation of resuspended nanoparticles with whole splenocyte cultures derived from 8-10-week-old female FVB mice. No significant decreases in the viability of splenocytes during 72-hour incubations were observed for either formulation when compared to media controls (Figure

2.4C). Additionally, the lack of any change in IFN-γ production after treatment with empty nanoparticles is further evidence that our formulations are nontoxic and nonimmunogenic.

Overall, neither formulation resulted in significant toxicity of whole splenocytes at any concentration investigated.

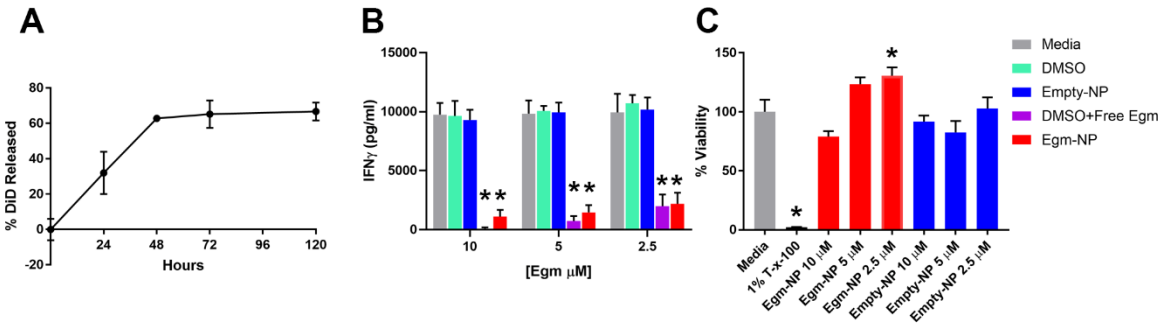

Figure 2.4 Nanoparticle formulated Egm inhibits $CD4^+$ T cell cytokine responses.

Notes: (**A**) Normalized release profile of DiD from nanoparticles incubated in 37 °C 1X PBS. (**B**) Interferon gamma (IFN-γ) production measured by ELISA from OT-II splenocytes stimulated with 50 μg/mL whole ovalbumin and incubated with vehicle controls, Egm in DMSO, and Egm loaded nanoparticles for 72 hours (n=3 biological replicates). (**C**) Average viability normalized to media controls of whole FVB splenocytes incubated for 72 hours with Egm- and empty-NPs (n=3 biological replicates). No acute toxicity was observed for either particle formulation. Final Egm concentration of particle suspensions is listed. Empty particle concentrations correspond to matched polymer doses. The significance of the data was evaluated via ordinary One-way ANOVA with multiple comparisons test (*$p<0.05$).
Abbreviations: DiD, 1,1'-Dioctadecyl-3,3,3',3'-Tetramethylindodicarbocyanine, 4-Chlorobenzenesulfonate Salt; T-x-100, triton-x-100; empty-NP, empty nanoparticle; Egm-NP, Egm-loaded nanoparticle; DMSO, dimethyl sulfoxide.

In combination with the cargo release profile and lack of acute toxicity observed from nanoparticle treatments within 72 hours (Figure 2.4A and C), IFN-γ inhibition was inferred to be the result of Egm released from nanoparticles that inhibited the activation of $CD4^+$ T cells undergoing antigen presentation. These studies cannot distinguish between inhibition due to Egm delivery to $CD4^+$ T cells or to antigen presenting cells in the mixed cell culture. Nevertheless, we

have demonstrated the first characterization of antigen specific $CD4^+$ T cell inhibition mediated by nanoparticle formulated Egm.

Maleimide-Thiol Chemistry Conjugated Anti-CD4 f(ab') Antibody Fragments Efficiently Target $CD4^+$ T cells in Heterogeneous Cell Suspensions

Successful encapsulation of fluorescent DiD within PEGylated PLGA nanoparticles enabled the characterization of $CD4^+$ T cell targeting specificity afforded by maleimide-thiol antibody fragment decoration. Anti-CD4 and isotype control F(ab') antibody fragments were conjugated to the surface of DiD-NPs and incubated for 30 minutes with whole splenocyte cultures derived from immunocompetent mice. Evaluation of DiD^+, nanoparticle bound immune cell subtypes was performed via flow cytometry (Figure 2.5A).

We analyzed DiD^+CD4^+ T cells, $CD8^+$ T cells, and non-T cells (B cells, dendritic cells, and macrophages) to determine nanoparticle CD4 targeting specificity. Anti-CD4 decorated particles achieved (~ 83%) $CD4^+$ T cell staining, and significantly increased targeting specificity for $CD4^+$ T cells compared to isotype (~5%) and undecorated controls (~2%). Additionally, anti-CD4 decorated particles also targeted $CD4^+$ T cells significantly more than $CD8^+$ T cells (~8%) and non-T cells (~3%) (Figure 2.5B). We further validated nanoparticle targeting specificity by incubating increasing concentrations of nanoparticles with whole splenocyte cultures. For anti-CD4 decorated particles, the degree of $CD4^+$ T cell targeting was dependent on particle concentration, while particle concentration had no effect on $CD8^+$ T cell targeting (Figure 2.5C). In all cases, undecorated and untargeted isotype-decorated particles exhibited low levels of nonspecific binding that was presumably due to electrostatic repulsion of negatively charged cell membranes mediated by sufficiently negative zeta potentials achieved in our formulations (Figure 2.2D). Therefore, the high degree of targeting specificity achieved by anti-CD4 decorated particles was almost certainly due to zeta potential mediated electrostatic repulsion from nonspecific cell types that was overcome by antibody fragment affinity for $CD4^+$ T cells.

The nanoparticle formulation designed and fabricated in this study yielded low levels of non-specific binding, and strong CD4 targeting specificity. More importantly, we were able to achieve these results in a physiologically relevant, heterogenous whole splenocyte population, rather than purified T cell populations.[71]

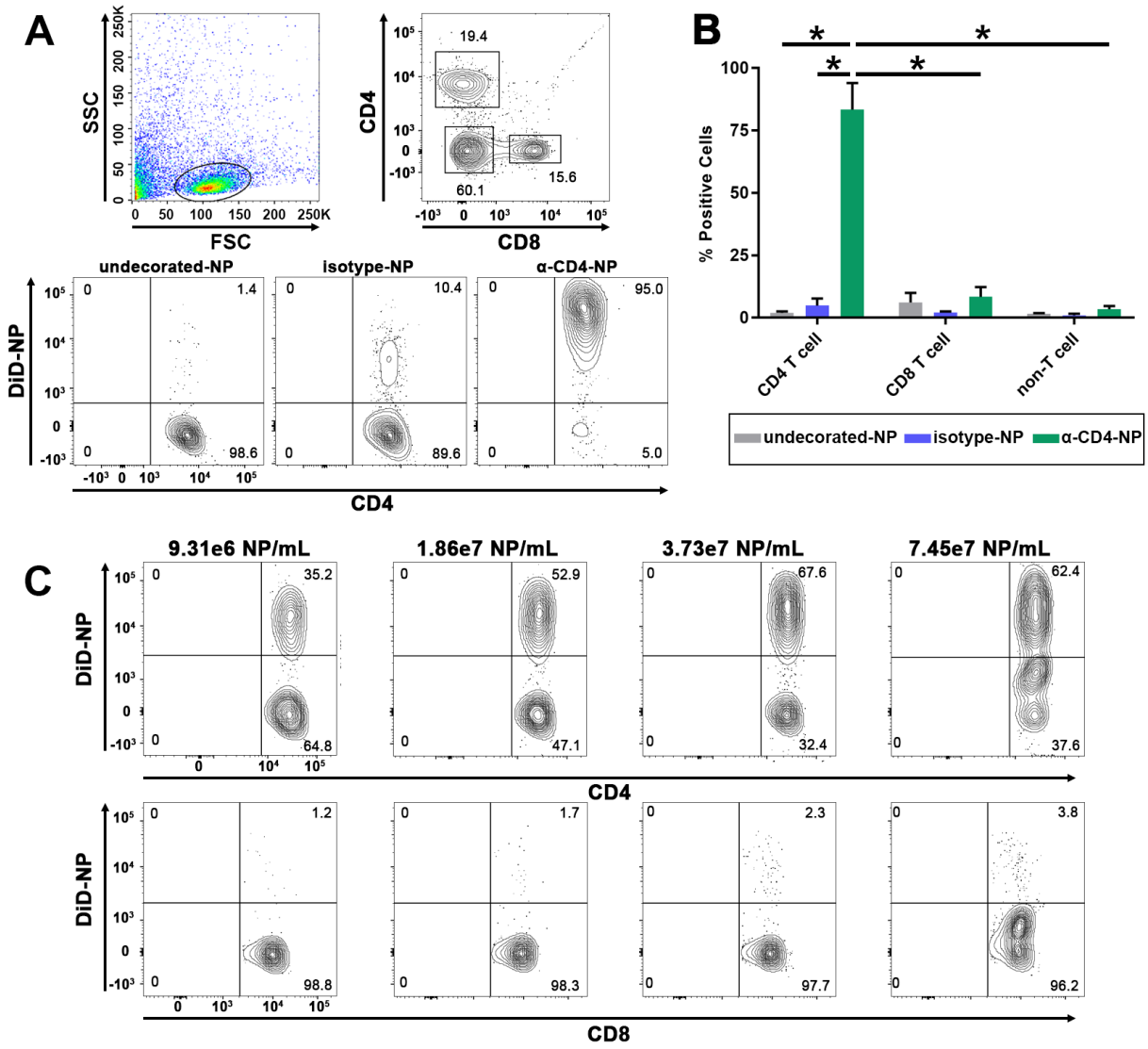

Figure 2.5 F(ab') fragment conjugated PEGylated PLGA nanoparticles target $CD4^+$ T cells.

Notes: (**A**) Flow cytometry gating strategy used to analyze the targeting specificity of anti-CD4 decorated DiD-NPs and representative staining results from 1 of 3 experiments. Full flow cytometry gating strategy for targeting experiments shown in Supplemental Figure A.3. (**B**) Quantification of DiD positive splenocytes incubated with either undecorated, isotype control decorated, or anti-CD4 decorated fluorescent nanoparticles suspended in 1X PBS. The flow cytometry probe for CD4 staining utilized an antibody clone that recognized a different epitope

of CD4 than those used to decorate nanoparticles. (**C**) Analysis of $CD4^+$ T cell targeting specificity after incubation with increasing concentrations of anti-CD4-decorated DiD-NPs. Nanoparticle concentrations were determined by nanoparticle tracking analysis. The percentage of DiD^+CD4^+ T cells and DiD^+CD8^+ T cells is indicated in the upper right-hand quadrants of the flow cytometry plots. Splenocytes were derived from female C57BL/6J mice. The significance of the data was evaluated via ordinary Two-way ANOVA with multiple comparisons test (*$p < 0.05$).

Abbreviations: SSC, side scatter; FSC, forward scatter; undecorated-NP, undecorated DiD-NP; isotype-NP, isotype control antibody fragment decorated DiD-NP; α-CD4-NP, anti-CD4 antibody fragment decorated DiD-NP.

CONCLUSIONS

In this work, we synthesized and characterized anti-CD4 decorated PEGylated PLGA nanoparticle formulations for specific delivery of Egm to $CD4^+$ T cells. Encapsulation of Egm did not affect the physical or chemical characteristics of the vehicle believed to be important for *in vivo* administration and cell-targeted delivery of cargo. Nanoscale elemental analysis and analytical chemistry methods supported the notion that emulsion mediated fabrication localized Egm within nanoparticle cores. We verified that nanoparticle formulations of Egm made from the FDA approved polymers PLGA and PEG were biocompatible and capable of releasing the majority of their payload in a therapeutically relevant timeframe. Using maleimide-thiol chemistry conjugation of targeting antibody fragments, we were able to achieve high levels of $CD4^+$ T cell targeting specificity *ex vivo* with a minimal degree of non-specific particle binding. Furthermore, we have demonstrated antigen specific inhibition of $CD4^+$ T cell cytokine responses mediated by nanoparticle formulated Egm. Collectively, this work represents the first characterization of the immunomodulatory effects of Egm, as well as, the research and development of a rationally designed nanoparticle delivery vehicle intended for systemic Egm administration for the treatment of $CD4^+$ T cell hyperactivity in rheumatic autoimmunity.

Although we limited the investigation of our formulation to $CD4^+$ T cells, others have recently validated a similar formulation for delivery to $CD8^+$ T cells.[71] In fact, the conjugation mechanism of our formulation could presumably enable preferential delivery of hydrophobic cargo to any specific cell type possessing a unique cell surface marker with a corresponding antibody that can be decorated on the surface of biomaterial-based particles. We highlighted the clinical potential of Egm delivery for the treatment autoimmune rheumatic diseases such as rheumatoid arthritis, systemic lupus erythematosus, and scleroderma, however, this formulation could also have broader applications in the treatment of human cancers associated with dysfunctional Hh signaling. Additionally, numerous FDA approved hydrophobic immunosuppressants are currently used to broadly suppress the immune systems of patients with autoimmune diseases so that disease symptoms can be managed. The modular encapsulation mechanism employed by our formulation could enable focused delivery of these agents to improve the therapeutic index by limiting the necessary dosage, reducing off-target toxicities, and mitigating opportunistic infection. Additionally, several commercially available hedgehog inhibitors are currently approved for the treatment of human cancers while others are undergoing clinical trials for use in rheumatoid arthritis. Investigation of hedgehog signaling as a new therapeutic target with Egm-loaded nanoparticles may enable off-label use of existing FDA-approved Hh inhibitors in rheumatic autoimmunity.

Future experiments will focus on characterizing nanoparticle biodistribution over time following intravenous administration to determine optimal therapeutic administration strategies. Optimization of the current formulation components will be performed to evaluate circulation half-life, *in vivo* targeting efficiency, and suppression of T follicular helper cell activation in germinal centers. Additionally, studies utilizing prophylactic and therapeutic administration of

CD4 targeted, Egm-NPs still need to be performed in order to elucidate the translational potential of Hh signaling inhibition for the restoration of peripheral tolerance mechanisms that are deficient in autoimmunity.

CHAPTER 3

ANTIBODY-CONJUGATED SUPERPARAMAGNETIC MICROPARTICLES WITH CLEAVABLE DNA LINKERS CAPTURE, LABEL, AND RELEASE EXTRACELLULAR VESICLES

ABSTRACT

Inappropriate activation of the epidermal growth factor receptor (EGFR) is a driver of tumorigenesis in cancers such as colorectal cancer (CRC). The activation status of EGFR is reflected in subpopulations of extracellular vesicles (EVs) originating from cancerous tissue and can be assessed using single EV analysis methods such as fluorescence activated vesicle sorting (FAVS). However, current laboratory-based EV purification techniques that rely on the size and density of small-EVs are labor intensive and time-consuming. Additionally, most affinity-based techniques lack the ability to release captured EVs in a non-destructive manner. In this work we developed antibody-conjugated superparamagnetic microparticles with cleavable DNA linkers to enable the capture, fluorescent labeling, and non-destructive release of $EGFR^+$ EVs. We utilized heterobifunctional DNA linkers with two unique restriction sites flanking a fluorescently modified residue to provide selective labeling of liberated EVs mediated by restriction enzyme cleavage. Furthermore, we employed conventional copper-free "click" chemistry synthesis methods to generate cetuximab-DNA conjugates. Decorated superparamagnetic microparticles enable purification of $EGFR^+$ EVs from complex biological samples. Our novel immunocapture strategy achieved highly specific recovery of $EGFR^+$ EVs from conditioned media generated by a 3D culture of DiFi cells. Additionally, we have demonstrated non-destructive release of

captured EVs and the selective transfer of fluorescent labels enabled by the restriction enzyme-mediated cleavage of DNA linkers that tether capture antibodies to paramagnetic microparticles. This work is the first characterization of a restriction enzyme cleavable antibody conjugate linker that enables non-destructive release of captured EVs. The superparamagnetic immunocapture strategy employed in this study is modular and allows for the incorporation of additional EV antigen capture antibodies, potentially for sequential capture of discrete EV subsets. Importantly, this study also demonstrates the benefit of incorporating unique cleavage sites in DNA linkers for the selective labeling of captured material that could improve downstream analysis.

INTRODUCTION

The epidermal growth factor receptor (EGFR) is a receptor tyrosine kinase that is frequently overexpressed and/or mutated to be constitutively active in a variety of human cancers.[79,80] EGFR promotes proliferation, metastasis, angiogenesis, and the inhibition of apoptosis.[79,81] Several cancer therapies such as treatment with cetuximab, a recombinant human/mouse chimeric anti-human EGFR monoclonal antibody, are used clinically to combat EGFR driven cancers.[81,82] EGFR is estimated to be overexpressed in 60-80% of colorectal cancer (CRC) tumors and is associated with poor prognosis.[46] Moreover, EGFR over expression is reflected in the content of extracellular vesicles (EVs) secreted from multiple cancers.[40,47,48] Thus, EGFR is a critical analyte for understanding CRC and can be used to target CRC-associated EVs for subsequent purification.

EVs are membranous nanoparticles produced by most eukaryotic cells that are heterogenous in size, molecular composition, and method of biogenesis.[40,42] EVs contain a lipid bilayer, have been shown to transport lipids, proteins, and RNA, and range in diameter from

approximately 40 nm-10 μm.[42] Exosomes are approximately 40-130 nm, are found in blood, urine, saliva, and other bodily fluids, and are believed to originate from intraluminal budding of the endosomal compartment in multivesicular bodies that then fuse with the plasma membrane and release exosomes into the extracellular environment.[40,42] Due to their biogenesis, exosomes maintain the plasma membrane topology of the cells they originate from and display integral membrane proteins, known as tetraspanins, on their lipid bilayer.[42,83,84] Exosomes promote cancer progression by functioning as mediators of intracellular communication between tumors and distant tissues and transfer bioactive molecules between tumors and the tumor microenvironment.[40,42,43] Additionally, significantly higher amounts of exosomes are produced by human cancer cells. The mechanisms of communication as well as the messages that are conveyed through cancer cell derived exosomes are under extensive investigation.[41,42,44,45]

We have previously demonstrated that exosomes can be effectively isolated from biological samples for fluorescence activated vesicle sorting (FAVS) via sequential ultracentrifugation, a technique that separates particles from a solution based on particle size and density.[40] FAVS effectively separates populations of single exosomes from biological samples and allows for high-throughput assessment of multiple tumor-specific biomarkers in exosomes circulating in various biofluids.[40] However, sequential ultracentrifugation is time-consuming and labor intensive. Depending on the complexity of the starting sample, it can often take multiple days to isolate EVs before any downstream analysis can be performed.[40] Additionally, ultracentrifugation is unable to discriminate between exosomes derived from healthy and diseased tissue, which can result in signal diminishment in downstream analyses due to confounding, irrelevant EVs in the analysis pool.[50] Strategies utilizing liquid chromatography suffer from the same signal confoundment issue as ultracentrifugation and also significantly

dilute collected EVs.[51] Microfluidic strategies to isolate EVs are rapidly emerging, but microfluidic devices are generally limited by low sample processing speeds and subject to clogging and shear-stress induced damage to EVs.[52] Thus, purification methods that both preferentially isolate exosomes possessing tumor-specific biomarkers and also reduce the overall sample preparation time are desperately needed to improve the downstream analysis of tumor-derived exosomes for diagnostic and therapeutic analysis in human cancers.

Affinity based separation methods that rely on superparamagnetic capture beads, are commonly used to isolate exosomes from biological samples to significantly reduce the difficulty and time associated with sample processing. However, these magnetic particles often remain linked to collected EVs, which prevent single EV analysis.[50] There are currently two affinity based strategies utilizing superparamagnetic beads that allow for the non-destructive release of captured EVs prior to downstream analysis.[85,86] Neither of these options provide a mechanism to fluorescently label captured EVs for downstream flow cytometry analysis without the use of secondary antibodies. In this work we present superparamagnetic microparticles that are conjugated with EGFR targeting antibodies through a restriction enzyme-cleavable fluorescently labeled DNA linker. Two unique restriction sites flank a fluorescently modified residue in the DNA linker to provide selective labeling and release of captured EVs. These EGFR targeting superparamagnetic microparticles were used for the selective purification and fluorescent labeling of exosomes derived from human CRC cell lines to improve subsequent fluorescence activated vesicle sorting (FAVS).[40]

EXPERIMENTAL

Preparation of DNA Linkers

Single stranded DNA (ssDNA) oligonucleotides were purchased from Integrated DNA Technologies. BamHI and ClaI cleavable forward and reverse sequences are listed in Table 3.1 below. Forward and reverse sequences were resuspended in nuclease free distilled water (Invitrogen) to a final concentration of 100 µM. Equal molar amounts of forward and reverse sequences were annealed at 94°C for 2 minutes and then gradually cooled to 4°C before storage at -20°C.

Table 3.1 Oligonucleotide sequences.

Oligonucleotide	Sequence
Antibody Link Bam_Cla Forward Cy3-Modified	5'- /5AzideN/GCC AGG ATC GAT CG/iCy3/T GGG CTC AGG GAT CCG AGT CA-3'
Antibody Link Bam_Cla Forward	5'- /5AzideN/GCC AGG ATC GAT CGT GGG CTC AGG GAT CCG AGT CA- 3'
Antibody Link Bam_Cla Reverse	5'- /5Biosg/TGA CTC GGA TCC CTG AGC CCA CGA TCG ATC CTG GC -3'

Abbreviation: 5AzideN, 5' azide modification; 5Biosg, 5' biotin modification; iCy3, internal Cy3 modification.

Synthesis and Characterization of Cetuximab-DNA Conjugates

Cetuximab (Erbitux, Eli Lilly) was adjusted to 1 mg/mL with phosphate buffered saline (PBS) for conjugation reactions. A 10 mM solution of DBCO-PEG_4-NHS esters dissolved in anhydrous DMSO was added to cetuximab at a molar excess of 10 mol_{DBCO}/mol_{IgG}.[87] The reaction was kept at room temperature for 1 hour under constant rotary shaking. After 1 hour, the reaction was quenched by adding 1M Tris-HCL (pH 7.5) to a final concentration of 100 µM for 5 minutes under constant rotary shaking. Unreacted DBCO-PEG_4-NHS ester was removed with 7kDa MWCO Zeba spin columns, and cetuximab-DBCO conjugates were concentrated in PBS using 50 kDa spin dialysis filters (Amicon ultra 2mL). The resulting concentration of cetuximab-DBCO conjugates was determined using UV-Vis spectroscopy (280 nm, Nanodrop One^c). Heterobifunctional dsDNA linkers were added to 1mg/mL solutions of cetuximab-DBCO in PBS

at a molar excess of 3 mol_{DNA}/mol_{IgG}.[87] The reaction was kept at 4°C for 4 hours under constant rotary shaking. Unreacted dsDNA linkers were removed from cetuximab-DNA conjugates using 100 kDa spin dialysis filters (Amicon ultra 0.5 mL). DBCO and Cy3 degree of labeling was determined using UV-VIS spectroscopy (309 nm and 555 nm, Nanodrop One^{C}), and hydrodynamic size was measured using dynamic light scattering (Malvern Panalytical, Zetasizer Nano ZS) in PBS. DNA conjugation was confirmed using an EMSA kit with SYBR green and SYPRO Ruby EMSA stains (ThermoFisher) according to the manufacturer's instructions. Samples were run on a 4-20% polyacrylamide gel (BioRad, 456-1094) before staining with SYBR green and SYPRO Ruby and imaging (BioRad Gel Doc EZ).

Preparation of Cetuximab-MPs

Cetuximab-MPs were assembled according to Figure 3.1. Dynabeads® M-280 Streptavidin were washed with PBS 3x prior to conjugation with cetuximab-DNA conjugates. Cetuximab-DNA conjugates were added to 10 mg/mL washed Dynabeads in nuclease-free PBS at a ratio of 10-100 µg cetuximab:1mg beads and the reaction was kept at room temperature for 30 minutes under constant rotary shaking. Cetuximab-MPs were washed 3x with nuclease-free PBS to remove unreacted cetuximab-DNA. IVIG-MPs were prepared using the same procedure. Conjugation efficiency was determined using UV-Vis spectroscopy (Nanodrop One^{C}). The concentration of cetuximab in reaction supernatants was normalized to unreacted controls representing 0% conjugation for each concentration of cetuximab evaluated.

Release of Conjugates from Functionalized MPs for Western Blots

Cetuximab-DNA conjugates were removed from cetuximab-MPs via cleavage of dsDNA linkers with BamHI-HF (NEB) restriction enzymes. Purified cetuximab-MPs were added to BamHI in

cutsmart buffer (NEB) at a ratio of 1 mg cetuximab-MPs/20-60 units BamHI. The reaction was kept at 37°C for 1 hour and agitated every 15 minutes by gentle vortex mixing. Released cetuximab-DNA conjugates were isolated via magnetic separation of the reaction supernatant from cetuximab-MPs and denatured in Laemmli buffer (Biorad, 1610747) with beta-mercaptoethanol for 10 minutes at 95 °C. Samples were then run on a 4-20% polyacrylamide gel (Biorad, 5671094) and transferred to a nitrocellulose membrane using the iBlot2 Gel Transfer Device (Thermo Fisher). The membrane was blocked with 3% gelatin in TBS-T (0.1 % Tween-20) for 1 hour at room temperature. The membrane was then incubated with goat anti-human IR800 (1:10,000, LI-Cor Cat# 926-32232) for 1 hour at room temperature. After 5 washes with TBS-T, the samples were imaged on an Odyssey Fc Imager (Li-Cor).

Cell Culture and Preparation of Extracellular Vesicle Containing Media

DiFi cells were grown in a hollow fiber (HF) bioreactor using the manufacturer's instructions and as described in "using serum replacement".[88] The bioreactor was seeded with 2-5 x 10^8 cells. Individual collections of 20 mL were spun at 1200 rpm in a clinical centrifuge and the partially cleared supernatant was collected. 15 mL of the supernatant was gravity filtered through a 0.22 µm syringe filter on the day of collection (Millex®-GP Millipore Express®-PES membrane syringe filter unit); in some cases, minimal pressure was used to push through media when the flow of media slowed. One fourth of the supernatant was kept aside as unfiltered. Approximately 250 mL of hollow-fiber media (pooled collection of 12 days of conditioned media) was collected. The media was concentrated on 2 centriprep-70 concentrators (100,000 MWCO) to between 4 and 5 mL of retentate, and the concentrators were washed 3x with 30 mL PBS supplemented with 25 mM HEPES to remove the majority of phenol red prior to evaluations of protein concentration using infrared spectroscopy (Direct Detect Spectrometer, Millipore). The

retentate was then recovered per manufacturer's standard centrifugation method and diluted ~20-fold to a final concentration of 20 mg/mL.

Capture and Release of Extracellular Vesicles with Cetuximab-MPs

Cetuximab-MPs were blocked with 2% BSA in nuclease-free PBS for 1 hour at 4°C on a rocking table prior to $EGFR^+$ EV capture. After 1 hour, BSA was removed via magnetic separation and 2-0.5 mg of cetuximab/IVIG-MPs were resuspended in 500 µL nuclease-free PBS containing 100 µg of concentrated DiFi EVs in 1.5 mL microcentrifuge tubes. Cetuximab-MPs were incubated with DiFi EVs for 16 hours at 4°C on a rocking table. After 16 hours, cetuximab-MPs were washed 4x with 0.1% BSA and 6x with nuclease-free PBS to remove unbound EVs. EVs were removed from cetuximab/IVIG-MPs via cleavage of dsDNA linkers with BamHI-HF (NEB) and ClaI (NEB) restriction enzymes, or Turbo DNase (Thermo Fisher). Purified cetuximab-MPs were added to either BamHI-HF in rcutsmart buffer (NEB) at a ratio of 1 mg cetuximab-MPs/20-60 units BamHI-HF, ClaI in cutsmart buffer (NEB) at a ratio of 1mg cetuximab-MPs/10 units of ClaI, or Turbo DNase at a ratio of 1mg cetuximab-MPs/3 units Turbo DNase added once at 0.5 hours and once at 1 hours. The reactions were prepared in 50 uL volumes, kept at 37°C for 1 hour, and agitated every 15 minutes by flicking the tubes. Released EVs were isolated via magnetic separation of the reaction supernatant from cetuximab-MPs. Capture and release of $EGFR^+$ EVs using IVIG-MPs was performed using the same procedure as cetuximab-MPs.

Characterization of Captured Extracellular Vesicles

Captured EVs were evaluated by western blotting and flow cytometry. Protein samples were quantified by BCA for western blotting. Protein samples were loaded at 13.5 µg/lane, resolved

by 9% SDS-PAGE, and transferred onto nitrocellulose membranes before Western blotting. EGFR (Millipore Cat#06-847, Rb, 1:1000), TGF βi (Proteintech, Cat#10188-1-AP, Rb 1:1000), and Syntenin (Abcam, Cat# ab133267, Rb, 1:5000) were used, respectively. All blots were blocked with Intercept blocking buffer (TBS, LICOR) at 4°C for at least two hours, then with the primary antibody overnight at 4°C. Blots were washed with 1x TBST containing 0.1% tween for 10 minutes 4x before imaging with Odyssey Fc Imager (Li-Cor).

Cetuximab-MPs and EVs were evaluated using flow cytometry as previously described for sequential ultracentrifugation isolated EVs .[40] The 20 mg/mL concentrated HF media was diluted to 200 µg/300 µL for blocking and/or staining with IVIG (10 µg/mL) (CARIMUNE®-NF vendor CSL Behring LLC, Kankakee, IL 60901) and anti-CD63 (2 µg/mL) (BD Biosciences mouse anti-human CD63 clone-H5C6 (BV-421 conjugate)) overnight at 4°C. 100 µg of stained EVs were captured with cetuximab- and/or IVIG-MPs as described above and evaluated via FAVS.

EV size and concentration was measured with a Spectradyne nCS1 microfluidic resistive pulse sensing (MRPS) with the C-400 cartridge using manufactures instructions and as described in.[89]

Statistical Analysis

All error bars represent standard error of the mean unless otherwise indicated. One or two-way analysis of variance followed by multiple comparison tests was performed for most data presented here as indicated. Statistical significance was defined as $p < 0.05$, and statistical analyses were performed using Prism 7.04 (GraphPad Software).

RESULTS & DISCUSSION

Synthesis and Characterization of Cetuximab-DNA Conjugates

Here we present the synthesis of a homogenous conjugate of restriction enzyme-cleavable, heterobifunctional DNA and cetuximab antibodies designed for the subsequent preparation of cetuximab microparticles (cetuximab-MPs) used to capture, label, and release $EGFR^+$ EVs for single EV analysis (Figure 3.1).

Cetuximab-DNA conjugates were synthesized according to a two-part "click" chemistry conjugation reaction (Figure 3.1A).[87] First, cetuximab antibodies were functionalized with dibenzocyclooctyne (DBCO) groups via N-hydroxysuccinimidyl (NHS) ester chemistry. Subsequently, DBCO-functionalized cetuximab (cetuximab-DBCO) was reacted with heterobifunctional DNA linkers containing 5' azide and biotin modifications on opposing strands to generate cetuximab-DNA conjugates (cetuximab-DNA) or Cetuximab-cyanine 3 modified DNA conjugates (cetuximab-Cy3 DNA). Several experiments were conducted to characterize the physicochemical properties of the conjugates at each stage of the chemical synthesis.

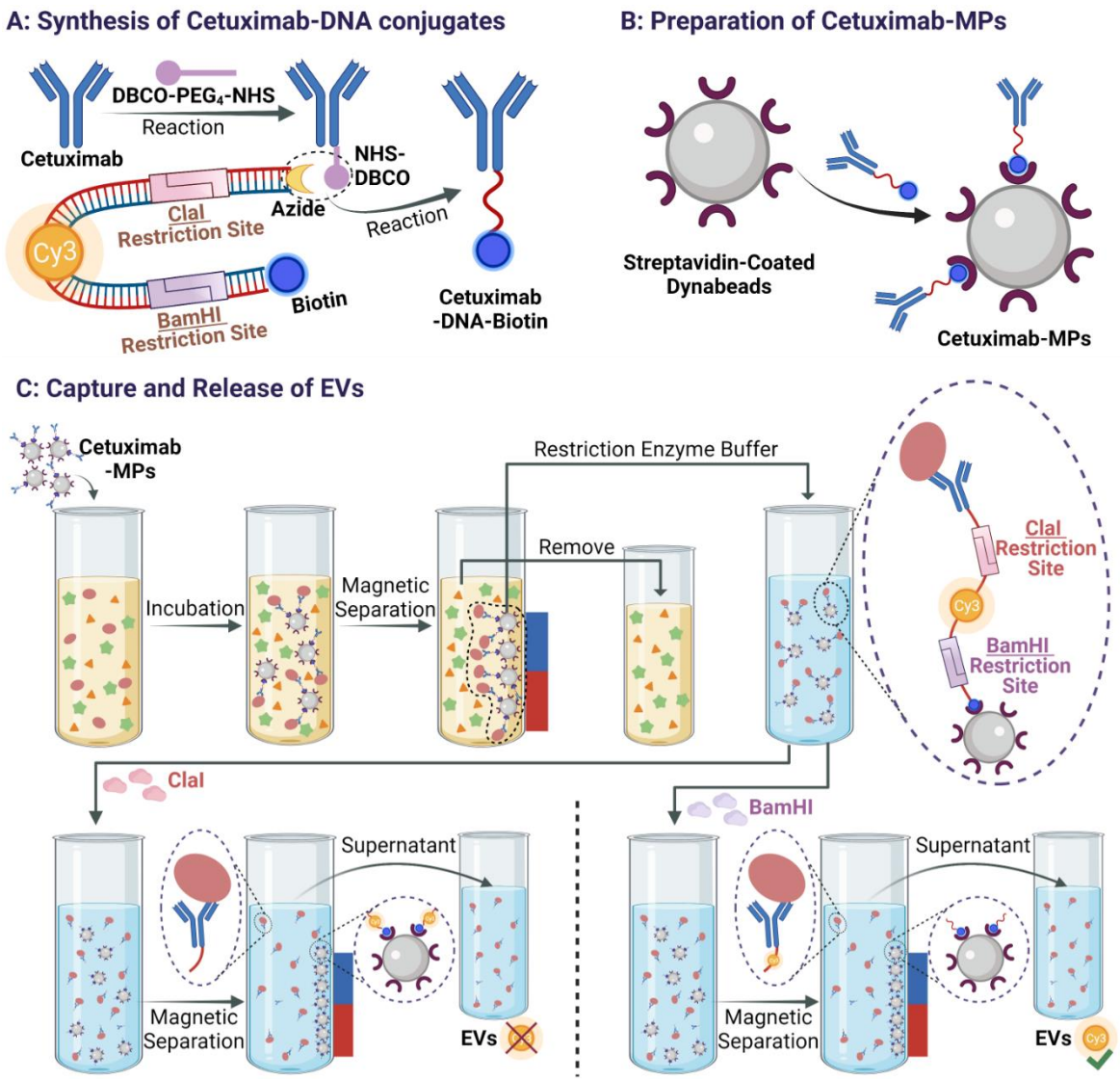

Figure 3.1 Schematic summary of EGFR^{+} EV capture, labeling, and release.

(A) Cetuximab-DNA synthesis protocol. (B) Cetuximab-MP preparation. (C) Magnetic capture and release of EVs experimental procedure.

Following DBCO functionalization, cetuximab-DBCO intermediates exhibited additional absorbance peaks at 260 nm and 309 nm corresponding to NHS and DBCO, respectively.[87,90] Conjugation of DNA linkers resulted in a reduction of the 309 nm peak intensity and addition of a 555 nm peak associated with Cy3 for cetuximab-Cy3 DNA conjugates (Figure 3.2).

Additionally, the average number of conjugated DBCO and DNA molecules per antibody calculated from UV-Vis spectroscopy was 31.5 for DBCO and 1.1 for Cy3 (Table B.1).

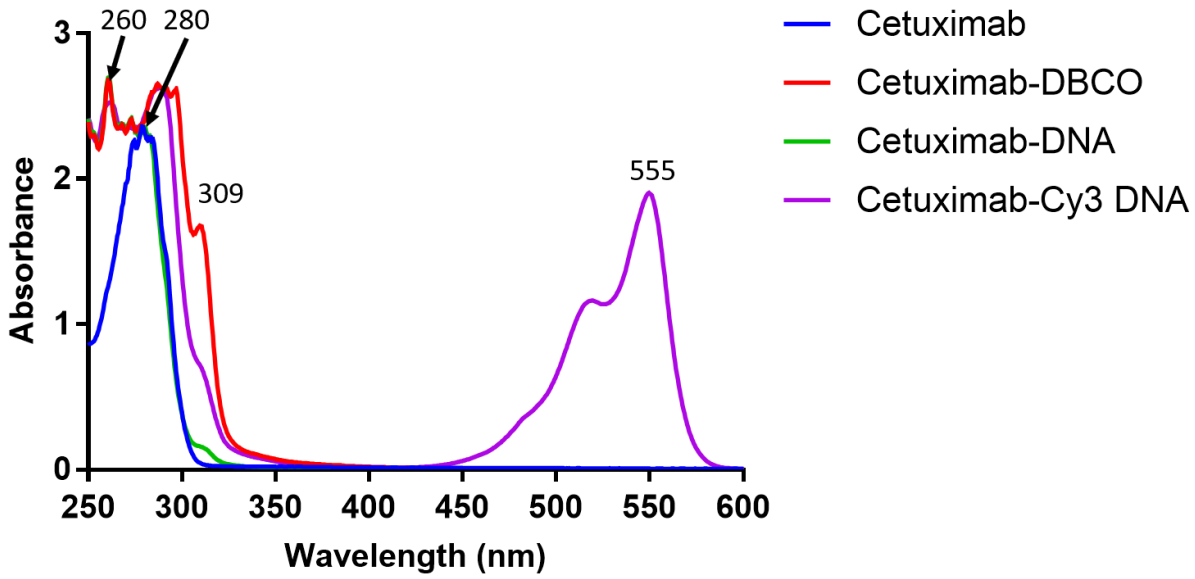

Figure 3.2 Conjugation of DNA linkers to cetuximab.

Average UV-Vis spectra representative of 3 batches of cetuximab conjugates suspended in PBS. All samples were suspended at 1.7 mg/mL for analysis. Absorption peaks corresponding to NHS/DNA (260 nm), protein (280nm), DBCO (309 nm), and Cy3 (555nm) are indicated.

DNA conjugation to cetuximab-DBCO intermediates was confirmed using gel electrophoresis and DLS. The effect of DNA conjugation on the hydrodynamic size of cetuximab conjugates was evaluated by dynamic light scattering (DLS). DLS traces revealed that all conjugates were monodisperse (Figure 3.3A). Functionalization with DBCO resulted in a 2 nm increase in the average size compared to the native cetuximab (11.3 nm). The average hydrodynamic size of cetuximab conjugates was further increased after functionalization with non-fluorescent or Cy3-modified DNA linkers by 3.9 nm and 4.8 nm, respectively (Figure 3.3B). Furthermore, DBCO and DNA conjugation reactions significantly increased the polydispersity index (PDI; a parameter calculated from a Cumulants analysis of the DLS-measured intensity

autocorrelation function)[70] of all conjugates compared to native cetuximab (0.1). Cetuximab-Cy3 DNA exhibited the highest PDI (0.31) and a secondary peak in the DLS trace (Figure 3.3C), however, similar to results that we have previously reported with fluorescent nanoparticles,[59] this may be an artifact caused by fluorescent excitation of the Cy3-modified DNA during DLS measurements, as no secondary peak was observed in the cetuximab-DNA DLS trace. Nevertheless, the PDIs of all cetuximab conjugates were below values associated with polydisperse distributions, (i.e. > 0.4), indicating that cetuximab-DNA conjugated can be cnsidered monodisperse.[70]

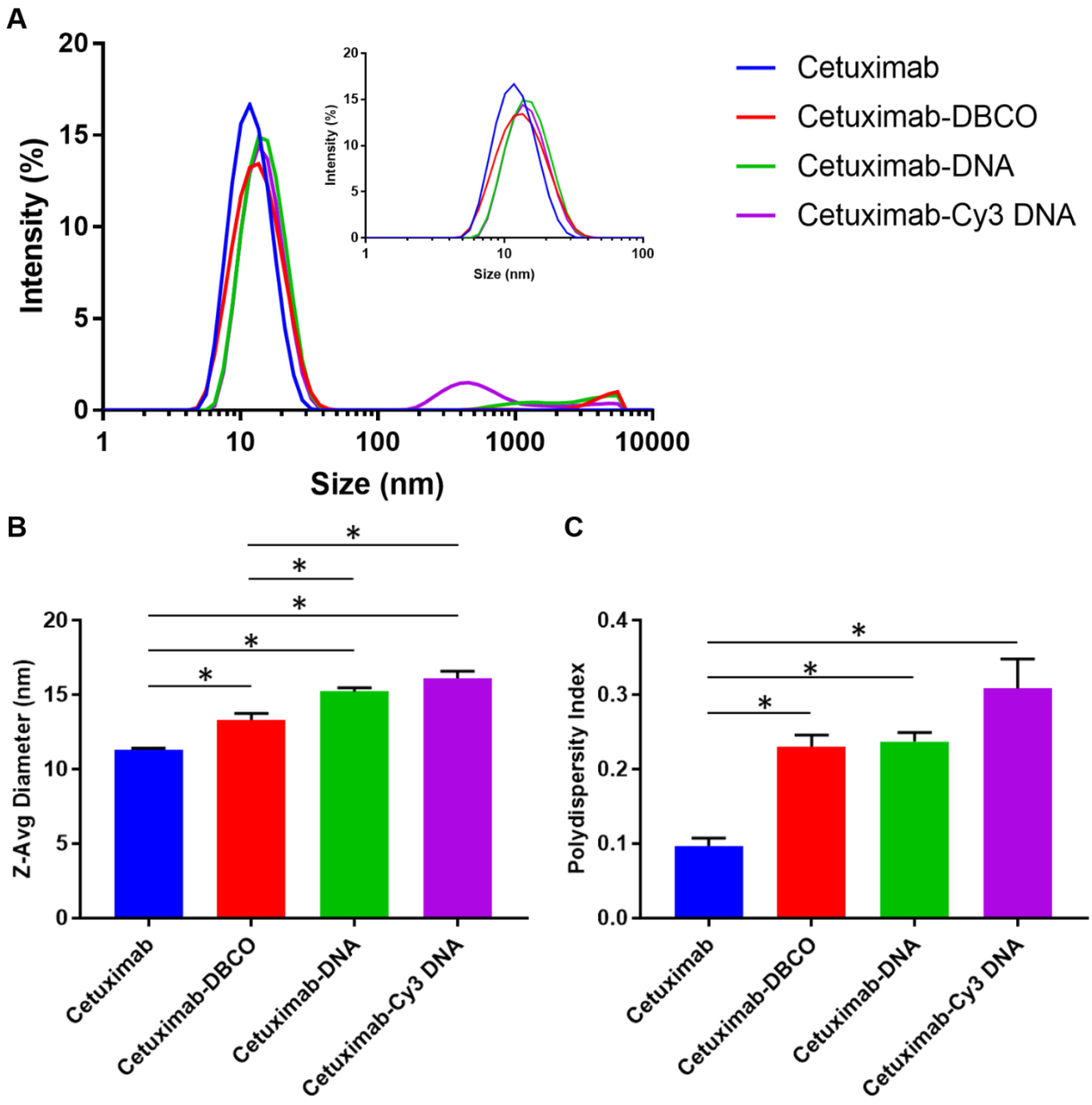

Figure 3.3 Conjugation of DNA increases the hydrodynamic size of cetuximab.

(A) Average DLS distributions representative of 3 batches of cetuximab conjugates. Inset corresponds to the distribution region between 1 and 100 nm. (B) Z-average diameter of cetuximab conjugates. (C) Polydispersity index of cetuximab conjugates. All data shown represent the mean ± SEM of at least three independent preparations for each antibody conjugate. The significance of the data was evaluated using one-way ANOVA with multiple comparison test (*P<0.05).

The effect of DNA conjugation on the electrophoretic mobility of cetuximab-DNA conjugates was evaluated using a modified electrophoretic mobility shift assay (EMSA) under non-denaturing conditions. Staining with SYBR green and SYPRO Ruby revealed that both cetuximab- and IVIG-DNA conjugates exhibited colocalized DNA and protein signals. Furthermore, both antibody-DNA conjugates migrated farther through the gel compared to their respective native antibodies but did not migrate as far as the unconjugated DNA linkers (Supplemental Figure B.1). However, unconjugated DNA linkers remained in all conjugates after spin-dialysis filtering. These results suggest that DNA conjugation increases the electrophoretic mobility of cetuximab-DNA and IVIG-DNA conjugates compared to the native cetuximab and IVIG antibodies, respectively. Thus, contrary to previously reported findings,[91] our results indicate the successful conjugation of heterobifunctional DNA linkers and resulting homogenously sized conjugate populations using conventional copper-free "click" chemistry.

Conjugation and Restriction Enzyme-Mediated Release of Cetuximab-DNA Conjugates

Cetuximab-MPs were fabricated via biotin-streptavidin conjugation of cetuximab-Cy3 DNA conjugates to 1 µm superparamagnetic Dynabeads (Figure 3.1B). The conjugation efficiency of several cetuximab-Cy3 DNA:Dynabead ratios was investigated via UV-Vis spectroscopy of depleted conjugation reaction supernatants. The highest conjugation efficiency of 98% was achieved for the 20 µg cetuximab-Cy3 DNA:1 mg Dynabead loading capacity (Figure 3.4A). Thus, all subsequent experiments using cetuximab-MPs were conducted with loading capacities $\leq$ 20 µg conjugate:1 mg Dynabead.

After determining the optimal biotin-streptavidin conjugation conditions, enzyme mediated release of cetuximab conjugates from cetuximab-MPs was investigated via western blotting and flow cytometry. Western blots of cetuximab-MP cleavage reaction supernatants

demonstrate the successful release of cetuximab-Cy3 DNA conjugates following cleavage of DNA linkers with BamHI restriction enzymes (Figure 3.4B). BamHI cleaved conjugates, as well as cetuximab-Cy3 DNA conjugate controls, exhibited additional bands than those associated with Fab and Fc fragments from native cetuximab antibodies. This may be due to DBCO mediated DNA functionalization of cetuximab antibodies at various primary amines found in both the Fc and Fab portions of the antibody (Figure 3.4B).

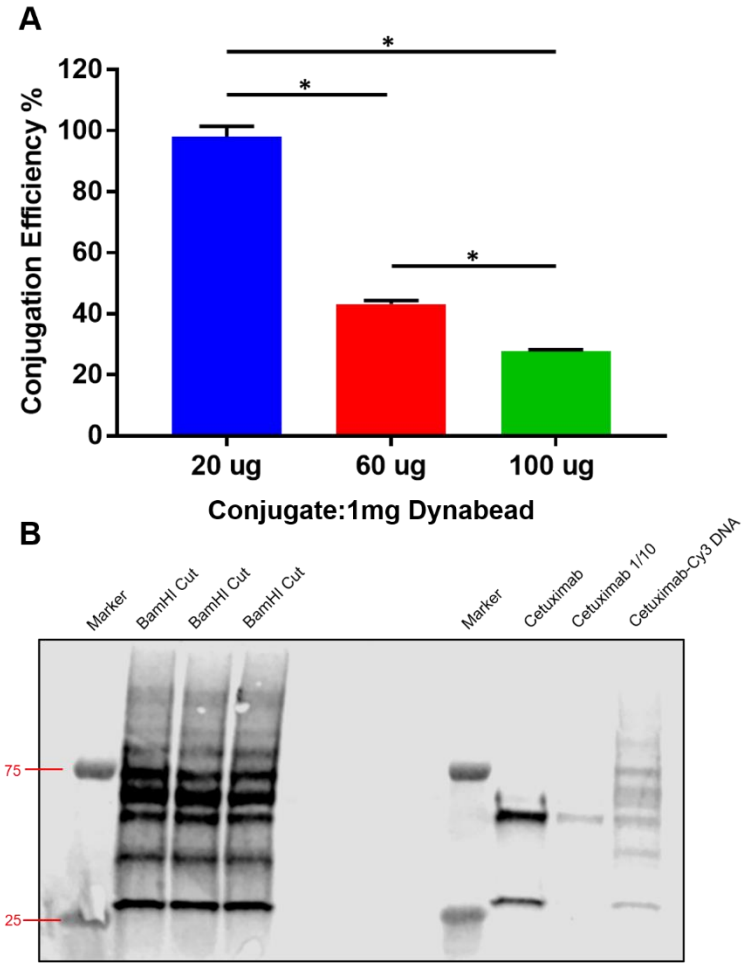

Figure 3.4 Conjugation and release of cetuximab-Cy3 DNA conjugates.

(A) Conjugation efficiency of cetuximab-Cy3 DNA conjugates added to washed Dynabeads in PBS at a ratio of 20-100 µg cetuximab:1mg beads. (B) Representative western blot of BamHI cleaved cetuximab-Cy3 DNA conjugates released from 20 µg cetuximab:1mg beads. All data shown represent the mean ± SEM of at least three independent preparations for each antibody conjugate. The significance of the data was evaluated using one-way ANOVA with multiple comparison test (*P<0.05).

The release of cetuximab conjugates following BamHI cleavage was confirmed via flow cytometry (Figure 3.5). Unconjugated Dynabeads exhibited slight autofluorescence in the Cy3 channel with a mean fluorescence intensity (MFI) of 68 for singlets (Figure B.7B). Cetuximab-MPs made with cetuximab-Cy3 DNA conjugates yielded elevated levels of Cy3 fluorescence (MFI=1346) for singlet beads in addition to a secondary population of cetuximab-MPs with increased scatter and Cy3 fluorescence (MFI=2665) that is suggestive of doublets (Figure 3.5C). The heterobifunctional DNA linkers used in this study were designed with two unique restriction sites flanking a fluorescently modified residue to provide selective labeling of liberated EVs mediated by restriction enzyme cleavage. In this way, cetuximab-MPs cleaved with ClaI should retain Cy3 fluorescence while those cleaved with BamHI should release Cy3 fluorescence on cetuximab conjugates (Figure 3.1C). Cetuximab-MPs singlets cleaved with BamHI lost 77.2% of their Cy3 fluorescence (MFI =307) while those cleaved with ClaI retained 91.9% of their Cy3 fluorescence (MFI=1237). Furthermore, cetuximab-MP singlets cleaved with ClaI were 4x brighter than those cleaved with BamHI (Figure 3.5E and H). Thus, these results confirm the successful release of cetuximab-Cy3 DNA conjugates visualized by western blot (Figure 3.4B) and also demonstrate the selective release or retainment of the Cy3 label after cleavage of DNA linkers with BamHI or ClaI restriction enzymes, respectively.

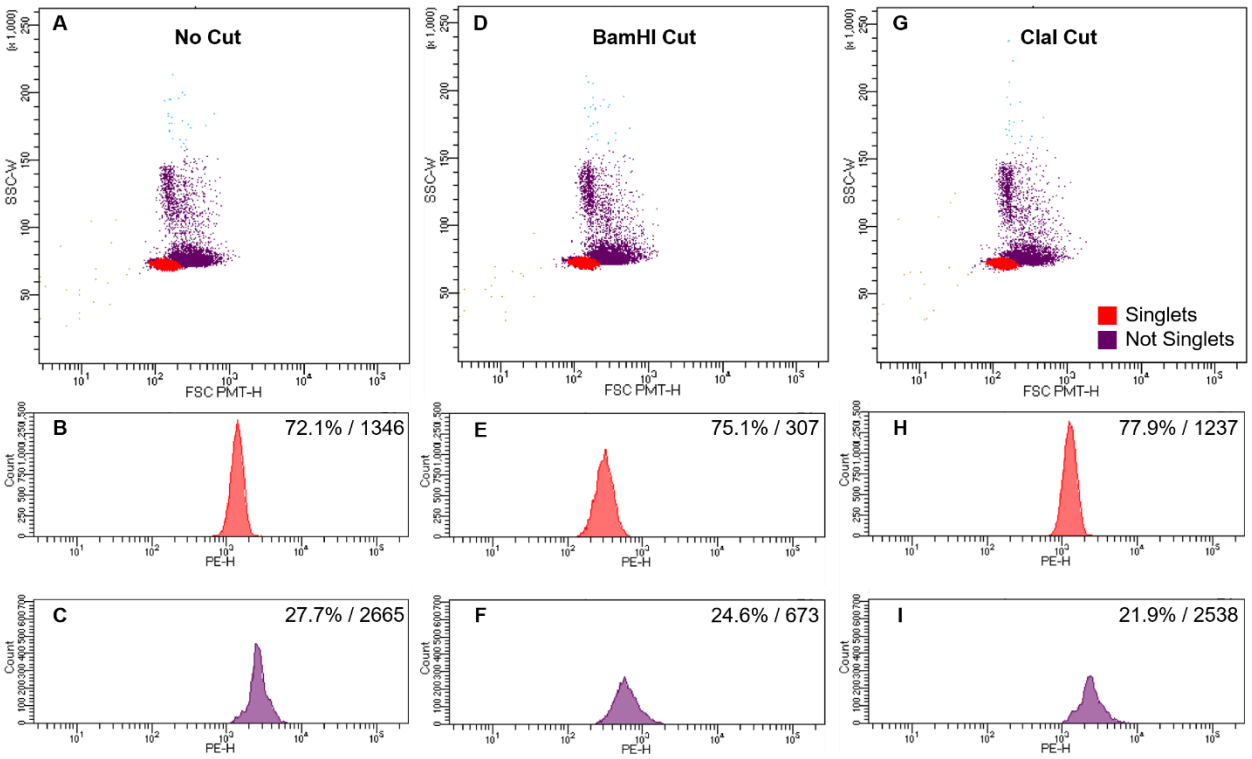

Figure 3.5 Selective release of Cy3 fluorescence from cetuximab-MPs.

(**A**) Scatter profile of cetuximab-MPs before restriction enzyme cleavage. (**B**) Cy3 fluorescence of cetuximab-MPs singlets before restriction enzyme cleavage. (**C**) Cy3 Fluorescence of cetuximab-MPs that were not singlets before restriction enzyme cleavage. (**D**) Scatter profile of cetuximab-MPs after BamHI cleavage. (**E**) Cy3 fluorescence of cetuximab-MPs singlets after BamHI cleavage. (**F**) Cy3 Fluorescence of cetuximab-MPs that were not singlets after BamHI cleavage. (**G**) Scatter profile of cetuximab-MPs after ClaI cleavage. (**H**) Cy3 fluorescence of cetuximab-MPs singlets after ClaI cleavage. (**I**) Cy3 Fluorescence of cetuximab-MPs that were not singlets after ClaI cleavage. All cetuximab-MPs made with 10 µg cetuximab:1mg bead loading capacity and suspended at equivalent concentrations for flow cytometry measures (n=1, % total from 20,000 events and mean Cy3 fluorescence intensity shown for each population).

Cetuximab-MPs Purify EGFR$^+$ EVs

DiFi cells are a human colorectal cancer (CRC) cell line that express 5 x 10^6 EGFR molecules per cell.[92] EVs secreted from DiFi cells are enriched with EGFR[40] and were used to simulate the purification of human EGFR$^+$ EVs from biological samples. 100 µg of EGFR$^+$ DiFi EVs isolated from a hollow fiber bioreactor culture of DiFi cells were incubated with 0.5-2 mg of cetuximab/IVIG-MPs with 10 µg cetuximab/IVIG : 1 mg Dynabead loading capacities (Figure 3.1C). The protein content of captured and released DiFi EVs was evaluated via western blotting.

Concentrated media samples isolated from hollow fiber bioreactor cultures of DiFi cells (DiFi concentrate) contained both $EGFR^+$ EV-related (EGFR and syntenin-1) and non-EV related (TGF βi) proteins. EVs released from cetuximab-MPs with BamHI, ClaI, or DNase were enriched with EGFR and syntenin-1 with minimal levels of TGF βi present. Those released from IVIG-MPs contained no detectable EGFR and syntenein-1 (Figure 3.6). Furthermore, depleted supernatants from IVIG-MPs contained EGFR, syntenin-1 and TGF βi, while those from cetuximab-MPs only contained TGF βi (Figure 3.6 and Supplemental Figure B.3). EVs released from cetuximab-MPs cleaved with DNase resulted in the highest detectable $EGFR^+$ EV related protein signals. However, this may be due to the significant concentration of albumin in the buffers required for BamHI and ClaI restriction enzyme cleavage. 24.1-33.3% of the total protein loaded in each well for cetuximab- and IVIG-MPs cleaved with BamHI and ClaI was albumin from the restriction enzyme buffers. The buffer required for DNase cleavage contained no added protein (Figure 3.6).

In order to investigate the efficiency of enzyme-mediated release of captured EVs from cetuximab- and IVIG-MPs, leftover MPs from BamHI, ClaI, and DNase cleavage reactions were boiled in sample loading buffer containing SDS and β-mercaptoethanol to provide destructive release conditions driven by heat, reduction of disulfide bonds, and EV lysis. Proteins released from cetuximab-MPs cleaved with BamHI, ClaI, and DNase by destructive conditions all contained significant amounts of EGFR and Syntenin-1, while those derived from IVIG-MPs only contained low amounts of TGF βi (Figure 3.6). In combination with the results observed from released EVs and depleted supernatants, these results suggest that the capture of $EGFR^+$ EVs by cetuximab-MPs is highly specific, with no observable nonspecific capture found on the

control IVIG-MPs. Despite the highly specific capture afforded by cetuximab-MPs, the restriction enzyme-mediated release of EGFR$^+$ EVs was only partially effective.

Reduction of the loading capacity of cetuximab-DNA conjugates:Dynabeads from 20 µg:1 mg (Figure B.3) to 10 µg:1 mg (Figure 3.6) improved the release of EGFR$^+$ EVs. However, further optimization of the release mechanism still needs to be achieved to enable the highest release of captured EVs for downstream analysis. Nevertheless, to the best of our knowledge, these results demonstrate the first restriction enzyme-mediated release of EVs from paramagentic immunocapture beads.

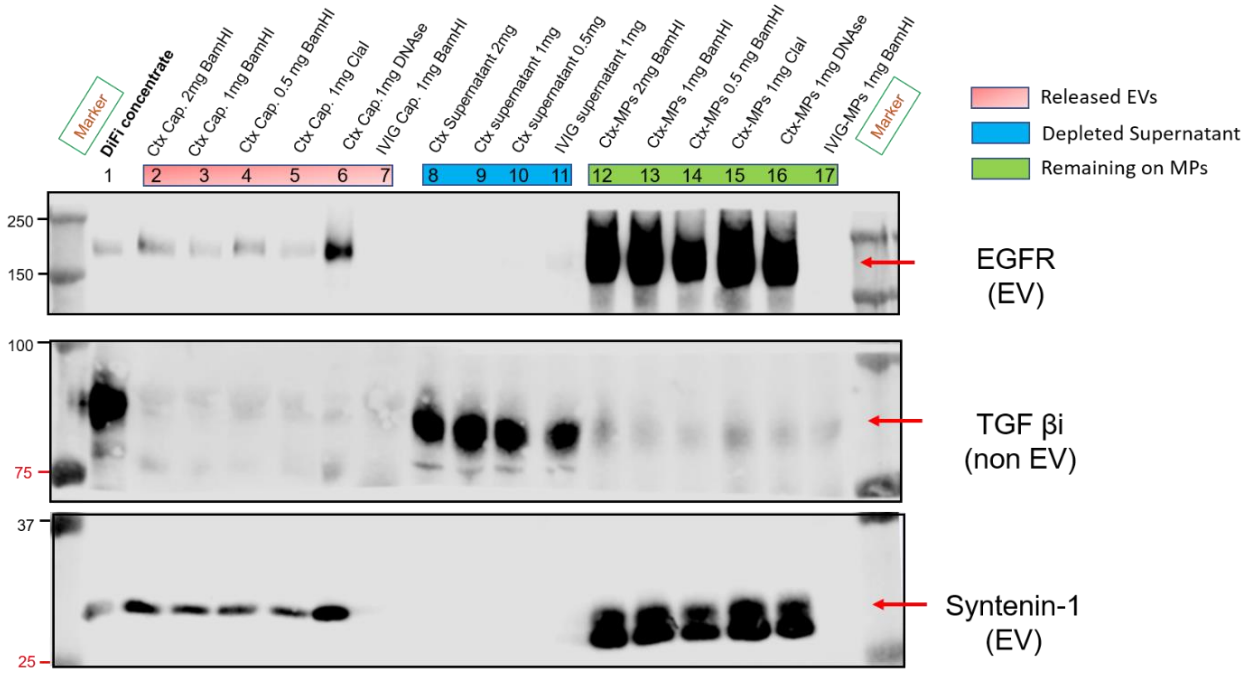

Figure 3.6 Cetuximab-MPs capture and release EGFR$^+$ EVs.

(A) Western blot of BamHI, ClaI, and Turbo DNase cleaved EGFR$^+$ EVs after capture with 10 µg cetuximab/IVIG : 1 mg Dynabeads. Cetuximab- and IVIG-DNA conjugates used for this experiment were made with non-Cy3-modifed DNA. The sample loaded in lane 1 represents the starting DiFi concentrate material. Samples loaded in lanes 2-7 represent the captured material that was released from cetuximab- or IVIG-MPs using BamHI, ClaI, or Turbo DNase cleavage of DNA linkers. BamHI and ClaI reaction buffers contained 0.1 µg/µL albumin that represented 24.1%-33.3% of the total protein loaded in lanes 2-5 and lane 7. Turbo DNase buffer does not

contain any protein. Samples loaded in lanes 8-11 represent the supernatant that was removed from beads after capture. Samples 12-17 represent the captured material that remained on the MPs after cleavage with BamHI, ClaI, or TurboDNase. Proteins were BCA quantified and loaded into lanes 1-11 at 13.5 µg/well. Proteins loaded in lanes 12-17 were prepared by boiling the respetive beads in the same volume of sample buffer to release material that remained on MPs after enzyme cleavage. Beads were removed from these samples prior to loading in lanes 12-17 via magentic separation.

Cetuximab-MPs Capture, and Release EGFR$^+$ EVs

In addition to bulk EV analysis methods (Figure 3.6), we also investigated whether EVs released from cetuximab-MPs with BamHI, ClaI, and DNase were compatible with downstream single EV analysis methods derived from fluorescence activated vesicle sorting (FAVS).[40] The majority of EVs released from cetuximab-MPs were between 65 nm and 85.1 nm, suggesting that most EVs captured by cetuximab-MPs were small exosomes (Figure B.2).[42] 100 µg of EGFR$^+$ DiFi EVs stained with anti-CD63, a tetraspanin associated with classical exosomes,[49] were incubated with 1 mg of cetuximab- or IVIG-MPs to evaluate the ability of cetuximab-MPs to capture and release EGFR$^+$ exosomes (Figures 3.7 and 3.8). Following BamHI and DNase cleavage, MPs and released EVs were analyzed via flow cytometry. Control MPs that were not exposed to DiFi EVs were used to distinguish the scatter of MPs from released EVs, as well as suspected singlet beads from those that appeared to be doublets (Figures 3.5 B.4). To provide quantitative analysis of restriction enzyme-mediated release efficiency, measured events corresponding to singlets were considered separately from those suspected to be doublets.

Cetuximab-MP singlets cleaved with BamHI (MFI=326) and DNase (MFI=300) showed little change in CD63 fluorescence intensity compared to those that were not cleaved with either enzyme (MFI=324) (Figure 3.7B, E, and H). However, while the distributions of CD63 fluorescence for BamHI and DNase cleaved cetuximab-MP singlets were unimodal, the distribution of CD63 fluorescence for those that were not cleaved with either enzyme was

bimodal with two distinct levels of CD63 fluorescence intensity (MFI ~200 and ~550). Therefore, although the MFI for each distribution was approximately equal, both BamHI and DNase cleavage resulted in a reduction of CD63 fluorescence intensity, indicating the successful release of $EGFR^+$ EVs. Furthermore, the corresponding doublets resulting from cleavage with BamHI (MFI=706) and DNase (MFI=635) both exhibited decreased CD63 fluorescence intensity compared to those from uncleaved MPs (MFI=917) (Figure 3.7C, F, and I). Additionally, as observed in western blots (Figure 3.6), the capture of $EGFR^+$ exosomes by cetuximab-MPs was highly specific, with almost no observable CD63 signal present on IVIG-MPs (Figure 3.7J, K, and L).

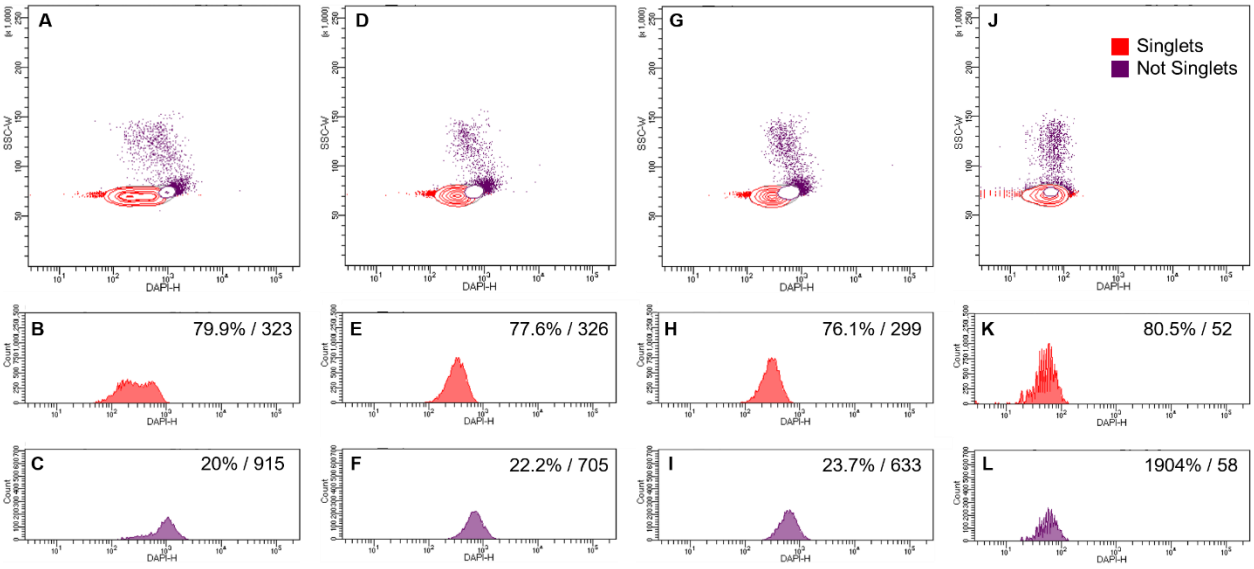

Figure 3.7 FAVS analysis of MPs from the capture and release of anti-CD63 stained $EGFR^+$ EVs.

(**A**) CD63 fluorescence of the scatter profile of cetuximab-MPs before restriction enzyme cleavage. (**B**) CD63 fluorescence of cetuximab-MPs singlets before restriction enzyme cleavage. (**C**) CD63 Fluorescence of cetuximab-MPs that were not singlets before restriction enzyme cleavage. (**D**) CD63 fluorescence of the scatter profile of cetuximab-MPs after BamHI cleavage. (**E**) CD63 fluorescence of cetuximab-MPs singlets after BamHI cleavage. (**F**) CD63 Fluorescence of cetuximab-MPs that were not singlets after BamHI cleavage. (**G**) CD63 fluorescence of the scatter profile of cetuximab-MPs after DNase cleavage. (**H**) CD63 fluorescence of cetuximab-MPs singlets after DNase cleavage. (**I**) CD63 Fluorescence of

cetuximab-MPs that were not singlets after DNase cleavage. (**J**) CD63 fluorescence of the scatter profile of IVIG-MPs before restriction enzyme cleavage. (**K**) CD63 fluorescence of IVIG-MPs singlets before restriction enzyme cleavage. (**L**) CD63 Fluorescence of IVIG-MPs that were not singlets before restriction enzyme cleavage. All MPs made with 10 µg cetuximab or IVIG:1mg Dynabead loading capacity and suspended at equivalent concentrations for flow cytometry measures (n=1, % total from 20,000 events and mean CD63 fluorescence intensity shown for each population).

The scatter profile of the supernatant resulting from BamHI and DNase cleavage of MPs following capture of anti-CD63 stained EVs contained a unique region with reduced forward and side scatter pulse height and width, presumably representing released EVs. Interestingly, there was also a significant region of scatter similar to that generated from MPs alone (Figures 3.5 and B.4). This suggests that residual MPs were present in the supernatant removed from cleavage reactions. This population may have been generated due to shearing of the magnetically pelleted MPs while supernatant was removed by pipetting, or due to the presence of MPs that could no longer be magnetized. Therefore, these events were removed from consideration, and we instead focused on the population of events with reduced pulse height and width as potential released EVs (Figure 3.8A, E, I and M). The events representing potential released EVs singlets resulting from BamHI (76.2%, MFI=80) and DNase (76.2%, MFI=144) cleavage of cetuximab-MPs both exhibited higher CD63 fluorescence intensity than those resulting from IVIG-MPs cleaved with BamHI (74.3%, MFI=34) and DNase (83.2%, MFI=34) (Figure 3.8C, G, K, and O). Additionally, CD63 fluorescence distributions of all potential released EVs from BamHI (12.2%, MFI=69) and DNase (28.1%, MFI=139) cleavage of cetuximab-MPs exhibited higher CD63 fluorescence than those resulting from IVIG-MPs cleaved with BamHI (20.5%, MFI=37) and DNase (16.3%, MFI=36) (Figure 3.8D, H, L, and P).

These results provide evidence that both BamHI and DNase cleavage released $CD63^+$ EVs from cetuximab-MPs but not from IVIG-MPs. However, the events with the highest CD63

fluorescence intensity after BamHI and DNase cleavage corresponded to cetuximab-MP singlets that were still present in the supernatant (Figure 3.8B, F, J, and N). Anti-CD63 stained EVs were also not completely removed from cetuximab-MPs after cleavage (Figure 3.7). Therefore, as observed in western blots (Figure 3.6), the restriction enzyme-mediated release from cetuximab-MPs after capture of $EGFR^+$ EVs is not optimal and is hypothesized to be significantly impacted by steric hindrance resulting from captured EVs. Additionally, from this data alone we are unable to determine if the $CD63^+$ events observed correspond to single EVs compatible with downstream antigen specific sorting of EVs enabled by FAVS. It is possible that a portion of these events could represent $CD63^+$ EV doublets or aggregates. Future experiments investigating the optimal sample processing and staining procedures of cetuximab-MPs may resolve the scatter profile of released EVs from that of MPs alone. Orthogonal measures from western blots, electron microscopy, and stochastic optical reconstruction microscopy (STORM) analysis of FAVS processed samples, will be performed to confirm our results.[40]

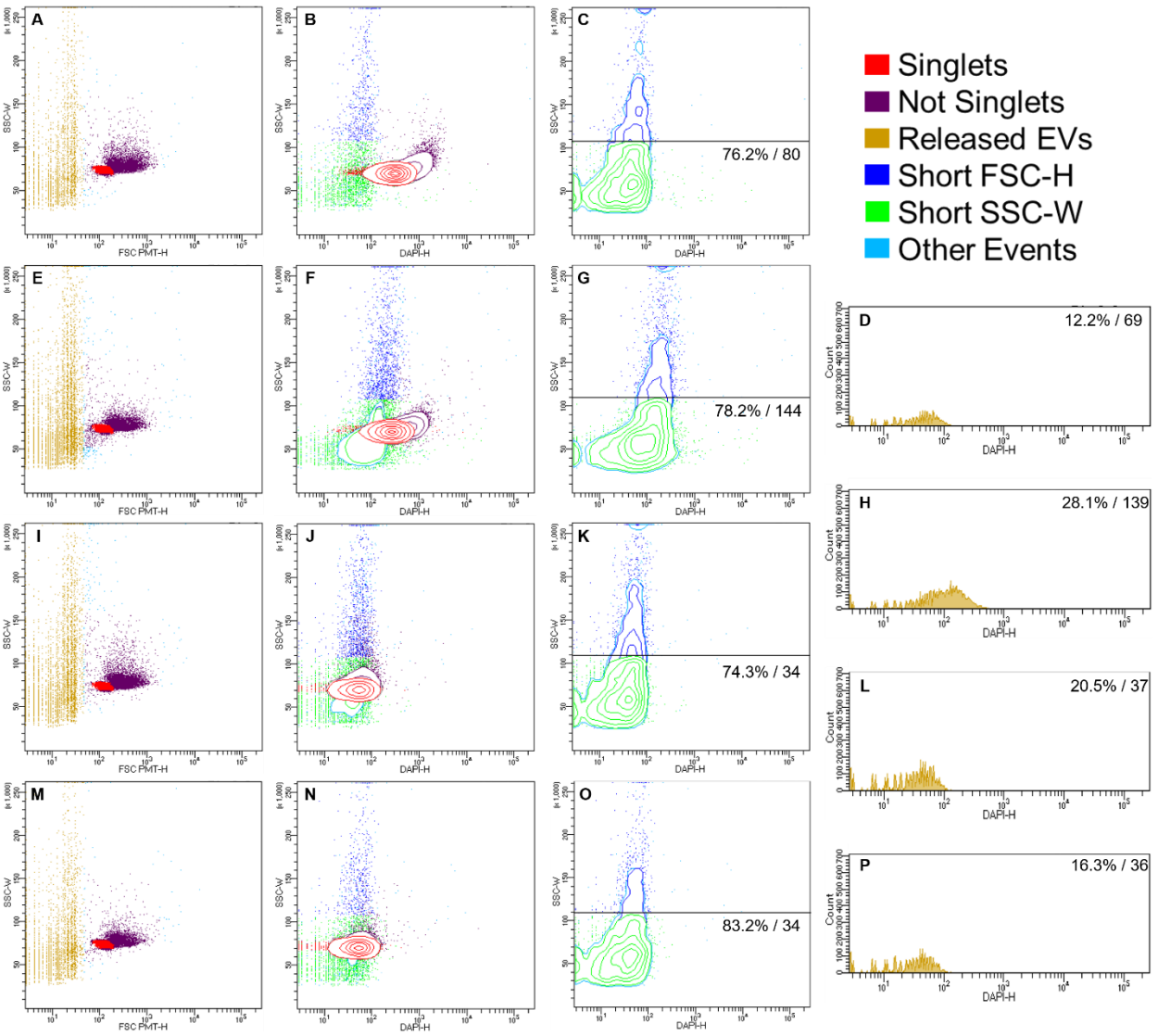

Figure 3.8 FAVS analysis of the supernatant from the capture and release of anti-CD63 stained $EGFR^{+}$ EVs.

(**A**) Scatter profile of cetuximab-MP supernatant released with BamHI cleavage. (**B**) CD63 fluorescence of the scatter profile of cetuximab-MP supernatant released with BamHI cleavage. (**C**) CD63 fluorescence of the scatter profile of released EVs from BamHI cleavage. (**D**) CD63 fluorescence of released EVs from BamHI cleavage of cetuximab-MPs. (**E**) Scatter profile of cetuximab-MP supernatant released with DNase cleavage. (**F**) CD63 fluorescence of the scatter profile of cetuximab-MP supernatant released with DNase cleavage. (**G)** CD63 fluorescence of the scatter profile of released EVs from DNase cleavage. (**H**) CD63 fluorescence of released EVs from DNase cleavage of cetuximab-MPs. (**I**) Scatter profile of IVIG-MP supernatant released with BamHI cleavage. (**J**) CD63 fluorescence of the scatter profile of IVIG-MP supernatant released with BamHI cleavage. (**K**) CD63 fluorescence of the scatter profile of released EVs from BamHI cleavage. (**L**) CD63 fluorescence of released EVs from BamHI cleavage of IVIG-MPs. (**M**) Scatter profile of IVIG-MP supernatant released with DNase cleavage. (**N**) CD63 fluorescence of the scatter profile of IVIG-MP supernatant released with DNase cleavage. (**O)**

CD63 fluorescence of the scatter profile of released EVs from DNase cleavage. (**P**) CD63 fluorescence of released EVs from DNase cleavage of IVIG-MPs. All MPs made with 10 µg cetuximab/IVIG:1mg Dynabead loading capacity and suspended at equivalent concentrations for flow cytometry measures (n=1, % parent for C, G, K, and O; % total from 20,000 events for D, H, L, and P; mean CD63 fluorescence intensity shown for each population).

Restriction Enzyme Cleavage Enables Selective Labeling of Captured EVs

We also investigated whether cleavage of the Cy3-modified DNA linkers that tether captured EVs to cetuximab-MPs would result in selective labeling of captured EVs with Cy3. Unstained $EGFR^+$ EVs were utilized for these experiments (Figure 3.9). Similar to the captured material analyzed in Figure 3.8, the scatter profile of the supernatant from BamHI and ClaI cleaved cetuximab-MPs utilizing Cy3-modifed DNA linkers contained a significant number of events that corresponded to residual MPs in the supernatant (Figure 3.9A, E, I and M). Therefore, the same gating strategy used in (Figure 3.8) was employed to isolate released EVs from residual MPs in the supernatant based on scatter. Events representing potential released EV singlets resulting from BamHI (83.8%, MFI=110) cleavage of cetuximab-MPs exhibited higher Cy3 fluorescence intensity than those resulting from cetuximab-MPs cleaved with ClaI (78%, MFI=47), and IVIG-MPs cleaved with BamHI (88.1%/MFI=51) and ClaI (90.5%, MFI=32) (Figure 3.9C, G, K, and O).

Cy3 fluorescence distributions of all potential released EVs from BamHI (13%, MFI=111) cleavage of cetuximab-MPs also exhibited higher mean Cy3 fluorescence than those resulting from cetuximab-MPs cleaved with ClaI (8.4%, MFI=47), and IVIG-MPs cleaved with BamHI (11.1%, MFI=54) and ClaI (8.1%, MFI=33) (Figure 3.9D, H, L, and P). Furthermore, as observed with control particles (Figure 3.5), residual MPs in the supernatant of cetuximab-MPs and IVIG-MPs cleaved with ClaI retained more Cy3 fluorescence compared to MPs cleaved with BamHI (Figure 3.9B, F, J, and N).

Collectively these results provide evidence that BamHI cleavage of Cy3-modified DNA linkers resulted in successful transfer of Cy3 fluorescence to $EGFR^+$ EVs captured with cetuximab-MPs. To the best of our knowledge, this is the first study supporting the selective transfer of a fluorescent label from an immunocapture bead to extracellular vesicles enabled by a non-destructive release mechanism. Despite this, it is clear that the release of captured EVs is not fully optimized. A majority of the Cy3 label, and likely the majority of captured EVs, were retained on the cetuximab-MPs after BamHI cleavage. Future experiments investigating additional optimization of the loading capacity of cetuximab-DNA conjugates, as well as the restriction enzyme cleavage reactions, still need to be performed to enable efficient release and fluorescent labeling of captured EVs. Furthermore, the experiments summarized in (Figure 3.9) will be repeated utilizing $EGFR^+$ EVs stained with lipophilic dyes, anti-CD63, and additional anti-EGFR antibodies, such as mab806,[40] to verify that the Cy3 positive singlets observed in these experiments were indeed $EGFR^+$ EVs.

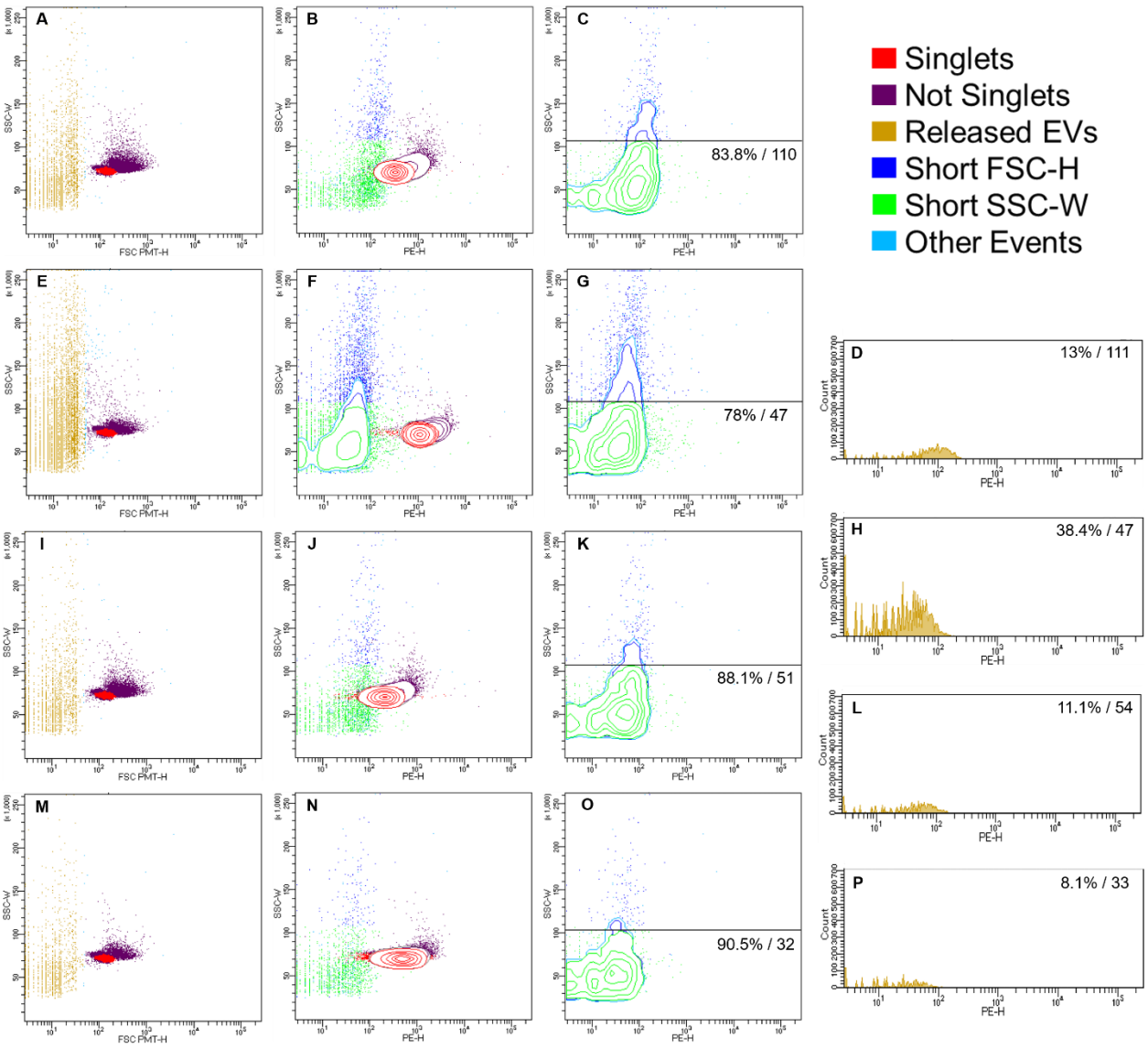

Figure 3.9 FAVS analysis of Cy3 transfer to unstained EGFR^{+} EVs.

(**A**) Scatter profile of cetuximab-MP supernatant released with BamHI cleavage. (**B**) Cy3 fluorescence of the scatter profile of cetuximab-MP supernatant released with BamHI cleavage. (**C**) Cy3 fluorescence of the scatter profile of released EVs from BamHI cleavage. (**D**) Cy3 fluorescence of released EVs from BamHI cleavage of cetuximab-MPs. (**E**) Scatter profile of cetuximab-MP supernatant released with ClaI cleavage. (**F**) Cy3 fluorescence of the scatter profile of cetuximab-MP supernatant released with ClaI cleavage. (**G**) Cy3 fluorescence of the scatter profile of released EVs from ClaI cleavage. (**H**) Cy3 fluorescence of released EVs from ClaI cleavage of cetuximab-MPs. (**I**) Scatter profile of IVIG-MP supernatant released with BamHI cleavage. (**J**) Cy3 fluorescence of the scatter profile of IVIG-MP supernatant released with BamHI cleavage. (**K**) CD63 fluorescence of the scatter profile of released EVs from BamHI cleavage. (**L**) Cy3 fluorescence of released EVs from BamHI cleavage of IVIG-MPs. (**M**) Scatter profile of IVIG-MP supernatant released with ClaI cleavage. (**N**) Cy3 fluorescence of the scatter profile of IVIG-MP supernatant released with ClaI cleavage. (**O**) Cy3 fluorescence of the

scatter profile of released EVs from ClaI cleavage. (**P**) Cy3 fluorescence of released EVs from ClaI cleavage of IVIG-MPs. All MPs made with 10 µg cetuximab/IVIG:1mg Dynabead loading capacity and suspended at equivalent concentrations for flow cytometry measures (n=1, % parent for C, G, K, and O; % total from 20,000 events for D, H, L, and P; mean Cy3 fluorescence intensity shown for each population).

CONCLUSIONS

In this study, we synthesized a homogenous conjugate of restriction enzyme cleavable DNA and cetuximab antibodies. The "click" chemistry conjugation of DNA linkers increased the average hydrodynamic radius of native cetuximab antibodies and resulted in homogenously sized antibody-DNA conjugates. Biotin/streptavidin conjugation of antibody-DNA conjugates resulted in facile fabrication of cetuximab-MPs with high conjugation efficiency. We validated the restriction enzyme-mediated cleavage mechanism and release of cetuximab-DNA conjugates from MPs using western blots and flow cytometry. Using cetuximab-MPs, we efficiently captured $EGFR^+$ EVs with high levels of purity from conditioned cell culture media. Flow cytometry analysis demonstrated proof-of-concept, non-destructive release and selective fluorescent labeling of $EGFR^+$ EVs. Collectively, this work represents the first characterization of a restriction enzyme cleavable antibody conjugate that enables non-destructive release of captured EVs and the research and development of a novel affinity-based separation reagent intended to purify $EGFR^+$ EVS for evaluation of EGFR activation status via FAVS.

Although we limited the evaluation of the purification efficiency of cetuximab-MPs to conditioned cell culture media, others have recently validated a similar approach in human plasma,[93] and we anticipate the performance of our strategy to be comparable. In fact, the restriction enzyme-mediated release we employed offers the unique advantage of selective labeling of captured EVs with fluorescent probes bound to DNA linkers that competing strategies cannot provide.[93] Selective labeling of captured EVs could enable multiplexing of the

samples for FAVS by incorporating multiple antibody-DNA conjugates with modified DNA linkers containing unique fluorescent probes to trigger sorting of captured EVs based on the transfer of the correct label from cleavage of the linker.

The restriction enzyme-mediated release of captured EVs was only partially effective, and we hypothesize that the incomplete release of EVs from the surface of cetuximab-MPs is mainly due to steric hindrance resulting from captured EVs on the surface of MPs blocking interaction of restriction enzymes with the dsDNA linkers that tether the cetuximab capture antibodies to the surface of the MPs. One additional factor that could be affecting release efficiency is DNA contamination from unconjugated DNA linkers. Unconjugated DNA linkers could be eliminated via size exclusion and/or ion exchange chromatography enabled purification of cetuximab-DNA conjugates.[87] Further reduction in the loading capacity of cetuximab-DNA conjugates, as well as, increasing the overall surface area of the paramagnetic Dynabeads used in this study, may provide improved access to restriction sites by reducing the density of captured EVs.

Increasing the concentration and/or the incubation period of the restriction enzyme cleavage reactions could also enable higher cleavage efficiencies although the results here reflect some optimization of these factors. Alternatively, increasing the length of the DNA linkers used to tether capture antibodies to cetuximab-MPs could also provide increased access to restriction sites to improve cleavage efficiency. Future experiments utilizing a streptavidin-conjugated, plate-bound interpretation of the cetuximab-MPs presented in this study could also be pursued if other strategies to improve cleavage efficiency are unsuccessful. Despite these limitations, our results provide the first proof of concept studies demonstrating antigen specific capture, selective labeling, and non-destructive release of EVs from complex biological samples while providing a

straightforward method for the isolation of specific EVs in sufficient numbers to power new analytical studies of EV properties.

CHAPTER 4

CONCLUSION

CHAPTER SUMMARIES & IMPACT

The research presented in this dissertation highlights the development of two unique antibody conjugates to provide novel therapeutic and diagnostic solutions. The overall goals of this work were to enable both targeted immunosuppression of $CD4^+$ T follicular helper (Tfh) cells and the purification of $EGFR^+$ cancer associated extracellular vesicles. The work presented in this dissertation represents an important first step towards the realization of both applications.

Significant Aim 1

In chapter 2, anti-CD4 decorated PEGylated PLGA nanoparticle formulations were developed for specific delivery of Egm to $CD4^+$ T cells. Encapsulation of Egm did not affect the physicochemical properties of the base nanoparticle delivery vehicle. Nanoscale elemental analysis and NMR revealed that emulsion mediated fabrication localized Egm within nanoparticle cores. PEGylated PLGA nanoparticle formulations of Egm made from the FDA approved polymers PLGA and PEG were biocompatible and released the majority of their payload within 48 hours. Using maleimide-thiol chemistry conjugation of targeting antibody fragments, we achieved high levels of $CD4^+$ T cell targeting specificity in a heterogenous population of immune cells. Furthermore, we demonstrated antigen specific inhibition of $CD4^+$ T cell cytokine responses mediated by nanoparticle formulated Egm. Collectively, this work was the first characterization of the immunomodulatory effects of Egm, and identified the optimal

antibody conjugation chemistry and nanoparticle formulation parameters for targeted delivery of Egm to $CD4^+$ T cells.

The primary innovation of this research is founded in the development of immune cell targeted carriers designed specifically to improve therapies for rheumatic autoimmune diseases, such as SLE. SLE treatments remain largely focused on unformulated drugs that lack pharmacologic or tissue specificity. Although there is currently one approved monoclonal antibody therapy developed specifically for SLE, Benlysta, its effectiveness is limited, and the majority of patients still utilize corticosteroids, hydroxychloroquine, and other untargeted immunosuppressive therapies to manage disease symptoms. Consequently, a lifetime of systemic immunosuppression results in a number of unfavorable health outcomes, including compromised immunity against pathogens, premature cardiovascular disease, and osteoporosis while failing to robustly address the symptoms of SLE. CD4-targeted Egm-NPs overcome two critical obstacles to improve therapy and a novel compound addresses a third limitation of current therapies to create an entirely new paradigm for next-generation SLE therapeutics.

Overactivity of PDE4 promotes augmented T cell cytokine responses that are important for GC formation and has been identified in SLE patients. A number of PDE4 inhibitors exist, including some that are clinically available for non-SLE indications, such as apremilast (Otezla®). However, the chemical structure of these compounds leads to profound insolubility in water. Despite initial dose titration, orally administered PDE4 inhibitors are associated with significant gastrointestinal consequences. The onset of symptom relief in the approved indications, including plaque psoriasis and psoriatic arthritis, can also be slow. We hypothesize that the low aqueous solubility of PDE4 inhibitors compromises bioavailability and results in accumulation in the gastrointestinal tissues, producing the observed side effects and minimizing

the dose that can reach the target tissues. Overcoming this solubility obstacle is one potential innovation of CD4-targeted Egm-NPs.

Current PDE4 inhibitors strongly inhibit a range of PDE4 isoforms including PDE4D2 that is present throughout the cell cytosol and possesses important, non-immune functions. Egm is unable to suppress PDE4D2 activity but inhibits other PDE4D isoforms that are recruited to the T cell surface and are involved in GC formation. Therefore, Egm presumably modulates signaling primarily near the site of the immune synapse and may minimally impact cellular functions that depend on PDE4D2 activity. This unique pharmacologic specificity combined with an effective delivery system may enable improved therapeutic carrying capacity and symptom management in SLE, which is the second innovation of this research. The ability to target drug delivery to $CD4^+$ T cells, or antibody-producing B cells that are also involved in GC responses, also provides additional new tools for characterizing the benefit of SLE drug targeting among various immune cell types involved in the disease. In addition, state-of-the-art drug delivery that provides targeted inhibition of autoantibody production would produce paradigm-breaking impacts in the treatment of SLE and other autoimmune diseases such as atopic dermatitis, rheumatoid arthritis, and scleroderma.

Significant Aim 2

Chapter 3 demonstrated the synthesis and characterization of a homogenous conjugate of restriction enzyme cleavable DNA and cetuximab antibodies. Conventional “click” chemistry conjugation of DNA linkers increased the average hydrodynamic radius of native cetuximab antibodies. Cetuximab-MPs were easily fabricated using biotin/streptavidin conjugation of antibody-DNA conjugates and streptavidin coated superparamagnetic microparticles. We validated the restriction enzyme-mediated cleavage mechanism of cetuximab-DNA conjugates

from MPs alone, but we experienced sub-optimal release associated with steric hindrance from captured EVs on the surface of MPs. Using cetuximab-MPs, we efficiently captured $EGFR^+$ EVs with high levels of purity from conditioned cell culture media. Flow cytometry analysis demonstrated proof-of-concept, non-destructive release and selective fluorescent labeling of $EGFR^+$ EVs. Collectively, this work was the first characterization of a restriction enzyme cleavable antibody conjugate that enabled antigen specific capture, selective labeling, and non-destructive release of EVs from complex biological samples.

Superparamagnetic microparticles, are commonly used to isolate cells and EVs from biological samples. Commercially available microparticles allow for covalent and non-covalent conjugation of capture antibodies that bind specific antigens to magnetically retrieve cells and EVs from the bulk sample. In the case of EVs, magnetic purification simplifies purification procedures and eliminates the need for specialized ultracentrifugation equipment. However, these magnetic particles often remain linked to collected EVs, which prevents downstream single EV analysis. To the best of our knowledge, no commercial options contain a cleavable linkage between the EV capturing antibody and the superparamagnetic particle that can transfer a fluorescent label. Unlike the rigorously characterized antigens used to distinguish the majority of human immune cell subtypes, new EV subtypes are still actively being discovered and the antigens that distinguish them are not fully established. Although the molecular topology of exosomes largely reflects the plasma membrane of the cell they originate from, the biogenesis of other EV subtypes is largely unknown. Therefore, it is difficult to apply a negative selection strategy to isolate single EV populations in a manner similar to those that are commercially available for depleting irrelevant immune cell populations based on the characteristic antigens that are used to distinguish their subtypes. Furthermore, although we only presented one

fluorescently modified DNA linker in Chapter 3, multiple DNA linkers modified with unique fluorescent probes could be conjugated to additional capture antibodies in order to multiplex antigen specific EV purification strategies. Thus, antigen specific purification and fluorescent labeling of known EV antigens paired with non-destructive liberation of captured EVs represents a significant innovation of this work.

Traditional laboratory-based, sequential ultracentrifugation techniques often require labor intensive procedures to isolate EVs from biological samples and resulting EV pellets often contain impurities in the form of lipoproteins and other non-membranous secreted nanoparticles. The majority of these contaminants can be removed through FAVS processing. However, this results in increasingly labor-intensive sample processing and increases the overall time required to approximately 48 hours to achieve pure samples of EVs. The cetuximab-MP mediated purification procedures presented in Chapter 3 vastly simplify sample processing to purify antigen specific populations of EVs. EV capture requires one overnight incubation period followed by approximately 6 hours of sample washing and restriction enzyme cleavage procedures to purify $EGFR^+$ EVs. However, we did not explore shorter incubation periods or modified washing procedures in Chapter 3 that could reduce the overall time required to obtain purified populations of EVs. The overnight incubation period at 4°C that we employed is likely unnecessary. Typical immunoprecipitation protocols employ incubation periods of 4-16 hours at 4°C and incubating samples at room temperature or 37°C can reduce that incubation period further. Additionally, we employed 10 wash cycles after capture to remove impurities from cetuximab-MPs, but most commercial protocols only recommend 3-5 wash steps. As presented in Chapter 3, our current purification procedures require approximately 24 hours to obtain purified EVs. This represents a 50% reduction in the sample processing time compared to

sequential ultracentrifugation followed by FAVs and further optimization of the incubation period and wash cycles could enable sample processing to be completed in less than 24 hours. Studying the biogenesis and bioactivity of EVs requires an enormous effort, and the reduction in sample processing time is the second innovation of this work. Any amount of time that can be utilized performing experiments rather than processing samples will improve our overall understanding of the biological implications of EVs in the context of health and disease.

SHORTCOMINGS

Significant Aim 1

We did not fully investigate the physicochemical effects of antibody fragment conjugation on Egm-NPs in Chapter 2. Initial attempts to characterize the effect of isotype control F(ab') fragment conjugation on the hydrodynamic diameter of Egm-NPs are presented in Appendix C. However, anti-CD4 fragment conjugated particles were not included in these measurements, and we did not evaluate any potential changes to the zeta potential of Egm-NPs. Thorough characterization of the physicochemical changes induced by fragment conjugation should be completed to better inform future *in vivo* studies.

The nanoparticle targeting presented in Chapter 2 was limited to $CD4^+$ T cells, but the conjugation mechanism of our formulation could enable preferential delivery of hydrophobic cargo to any specific cell type possessing a unique cell surface marker with a corresponding targeting antibody. To fully investigate the ability of Egm to inhibit germinal center responses, the B cell targeting capabilities of Egm-NPs should be investigated. Both T and B lymphocytes traffic from the bloodstream to SLOs before entering germinal center reactions. Decoration of Egm-NPs with anti-CD19 targeting antibody fragments would enable an additional cell-mediated

delivery strategy to enable preferential delivery of Egm to GCs, should $CD4^+$ T cell enabled delivery fail *in vivo*. Evaluation of CD19 efficiency should be performed as demonstrated in Chapter 2 using CD4 targeted NPs before moving to *in vivo* studies.

In addition to investigating the B cell targeting capabilities of Egm NPs, the immunological effects of Egm on B cells as well as other immune cell subtypes should also be explored. PDE4 is known to be active in antigen presenting cells such as B cells, dendritic cells, and macrophages. Therefore, the non-specific, hydrolytic release of Egm from our nanoparticle formulation could inhibit T cell activation via suppression of antigen presentation rather than suppression of signal transduction from the TCR during immune synapse formation. Ultimately, suppression of antigen presentation could also lead to the desired outcome of reduced autoantibody production, but we did not fully explore this mechanism in Chapter 2.

We presented initial measurements of the *in vivo* biodistribution of anti-CD4-NPs in Appendix C. However, a complete investigation of the biodistribution of our formulation has not yet been completed. Prior to investigation of *in vivo* efficacy of targeted Egm delivery, we should verify that CD4 and CD19 targeted particles are capable of targeting helper T cells and B cells in the secondary lymphoid organs where germinal center reactions occur. In order to do so, 8- to 10-week-old female, C57BL/6 mice could be retroorbitally injected with DiD-loaded-α-CD4-NPs, α-CD19-NPs, isotype-NPs, or undecorated-NPs. Initial studies determining the appropriate concentration of nanoparticles to inject, as well as the kinetics of binding in the blood, spleen, liver, and lymph nodes should be performed. Mice could be injected with nanoparticle suspensions and euthanized 1, 2, 3, 18, 24, 48, and 72 hours later so that tissue samples can be collected and processed for GC targeting analysis via flow cytometry and fluorescence microscopy. These studies will determine if helper T cell and B cell targeting is

effective following IV injection and whether nanoparticle-bound T and B cells traffic to the tissues where germinal center reactions occur.

We highlighted the clinical potential of Egm delivery for the treatment of autoimmune rheumatic diseases such as rheumatoid arthritis, systemic lupus erythematosus, and scleroderma. However, therapeutic studies utilizing prophylactic and therapeutic administration of CD4/CD19 targeted, Egm-NPs still need to be performed in order to evaluate their translational potential. To investigate whether nanoparticle formulated Egm can enable targeted immunosuppression of germinal center responses, we can immunize C57Bl/6 mice with NP-OVA + alum that have previously been adoptively transferred with purified OT-II $CD4^+$ T cells (specific for OVA). Mice can be immunized at the base of the tail and receive retroorbital injections of nanoparticle formulated Egm. To examine acute responses to the NP-OVA antigen, mice should be immunized and then immediately injected with α-CD4-Egm-NPs, α-CD19-Egm-NPs, undecorated-Egm-NPs, or corresponding empty-NPs targeted to CD4 or CD19. A separate control group of mice should receive IP injections of unformulated Egm dissolved in peanut oil to represent untargeted administration in the absence of nanoparticles. The optimal Egm dosage and frequency of injections to administer should be based on the results from biodistribution studies.

Following initial immunizations and Egm injections, mice should be boosted on day +7 before the spleen and lymph nodes are removed at day +14. Germinal center reactions can be assessed in these secondary lymphoid organs by flow cytometry staining for $CD4^+$ T cell activation (as described in Chapter 2), B cell activation ($CD80^+$, $CD86^+$, MHC class II^+), Tfh cells ($CD4^+TCR\beta^+CXCR5^+PD\text{-}1^{hi}$), germinal center B cells ($CD19^+B220^+Fas^+GL7^+$), and plasma cells ($CD138^+$, $CD19^{lo/-}$, $B220^{lo/-}$). We should also evaluate the percentage of class-

switched, GC B cells specific for NP-OVA by including stains for IgG1 and NP reactivity into our flow cytometry panel. Furthermore, NP-OVA specific IgG1 antibody titers in the serum should be measured by ELISA. Finally, ALT and AST liver enzyme content in the blood, and liver and kidney pathology should be evaluated to determine if any toxicity resulting from Egm or nanoparticle administration occurs.

In addition to evaluating acute responses to antigen, we should also investigate whether targeted delivery of Egm can address memory responses, which better mimic the "flaring up" of symptoms associated with many rheumatic autoimmune diseases. As described above, C57Bl/6 mice that have received adoptive transfers of OT-II $CD4^+$ T cells should be immunized with NP-OVA and boosted on day +7. However, no Egm treatments will be administered initially. Instead, the mice will be boosted again on day +21 to stimulate OT-II memory cells and then immediately injected with α-CD4-Egm-NPs, α-CD19-Egm-NPs, undecorated-Egm-NPs, or corresponding empty-NPs targeted to CD4 or CD19. A separate control group of mice will again receive IP injections of unformulated Egm dissolved in peanut oil. On day +28, the spleen, lymph nodes, and serum will be collected and the same analysis of germinal center reactions, antibody responses, and toxicity investigations described above should be performed. If Egm-NPs successfully inhibit acute and memory responses to antigen, therapeutic studies should be performed in the context of disease specific models to evaluate the therapeutic benefit of Egm-NPs in rheumatic autoimmunity.

Significant Aim 2

Although the work performed in Chapter 3 represents a significant proof-of-concept towards enabling a novel affinity-based purification strategy to enable selective capture and release of $EGFR^+$ EVs from complex biological samples, there is still much work to be done to optimize

and validate the performance of cetuximab-MPs. Procedure improvements can be made to improve the synthesis of cetuximab-DNA conjugates. For instance, the spin dialysis methods used to isolate cetuximab-DNA conjugates from unbound DNA linkers were not completely effective. Other studies have utilized chromatography electrophoresis to purify oligonucleotide- and DNA-conjugated antibodies.[87,91] Future studies should employ a combination of size exclusion or ion exchange chromatography, along with extraction of conjugate bands from native PAGE gels to purify cetuximab-DNA conjugates on the basis of the increased size, electrophoretic mobility, and negative charge afforded by successful conjugation of DNA linkers to native cetuximab antibodies. Improving the purity of cetuximab-DNA conjugates is expected to directly improve the loading potential and restriction enzyme-mediated cleavage of conjugates from cetuximab-MPs. Although we achieved $\geq$ 98% conjugation efficiency using the methods described in Chapter 3, a significant portion of "dummy strands" (DNA linkers with no cetuximab antibodies present) are assumed to be bound to cetuximab-MPs through biotin/streptavidin conjugation of the 5' biotin present in all DNA used for these studies. These "dummy strands" likely occupy a significant portion of the available streptavidin binding sites. In a similar fashion, a significant amount of "dummy strands" conjugated to cetuximab-MPs would directly compete with cetuximab-DNA conjugates for the total enzymatic activity of the restriction enzymes utilized to release conjugates by increasing the total number of restriction sites available for cleavage. Therefore, improving the purity of cetuximab-DNA conjugates would likely improve the maximum loading potential of fully functional cetuximab-DNA conjugates and cleavage efficiency of DNA linkers.

Once improved purification procedures have been established, the restriction enzyme-mediated cleavage of captured EVs should be optimized. Although we investigated several

cetuximab-MP loading capacities and modulated the reaction conditions of BamHI, ClaI, and DNase reaction conditions, a thorough investigation of these parameters still needs to be explored. The data presented in Chapter 3 clearly demonstrate a reduction in cleavage efficiency once $EGFR^+$ EVs were captured by cetuximab-MPs. We believe this is mainly due to steric hindrance mediated by captured EVs interfering with access to restriction sites. Further reduction in the loading capacity of cetuximab-DNA conjugates as well as increasing the overall surface area of the paramagnetic Dynabeads used may provide improved access to restriction sites reducing the density of captured EVs. Furthermore, increasing the concentration and/or the incubation period of the restriction enzyme cleavage reactions could also enable higher cleavage efficiencies. An attempt to employ both approaches was made in Chapter 3 that resulted in improved performance; however, release is not yet optimal.

Alternatively, increasing the length of the DNA linkers used to tether capture antibodies to cetuximab-MPs could also provide increased access to restriction sites to improve cleavage efficiency. We initially pursued a relatively short sequence length of 35 bp to reduce the susceptibility of our cetuximab-DNA conjugates and to prevent premature cleavage by endogenous nucleases found in human plasma. Antibody-DNA conjugates with 37 bp DNA sequences have previously been shown to resist significant nuclease degradation up to 5.7 days in human plasma by relying on the close proximity of the antibody and DNA sequence to provide protection from nuclease activity via end-capping in the absence of more sophisticated DNA engineering approaches.[94] As observed in Chapter 3, even after exposing EV capturing cetuximab-MPs with a total expected DNA linker content of 3 µg to a quantity of DNase recommended for digesting 200 µg of genomic DNA, the majority of captured EVs were not released from cetuximab-MPs. Future experiments investigating modifications to the sequence of

DNA linkers used to synthesize cetuximab-DNA conjugates should be pursued if other strategies to improve cleavage efficiency are unsuccessful.

The $EGFR^+$ EV capture efficiency of cetuximab-MPs was also not fully investigated. Current formulations have enabled the capture of a sufficient quantity of 100 µg EVs using 1mg of cetuximab-MPs, but the total capture efficiency was not investigated. Additionally, only 1 incubation period of 16 hours at 4°C was pursued. In order to fully optimize the capture efficiency of cetuximab-MPs, additional experiments titrating the mass of MPs added to a given mass of EVs, as well as a range of incubation periods for a given mass of EVs, should be investigated to determine the optimal conditions needed for sufficient capture of $EGFR^+$ EVs.

Although release samples were sufficient for investigation of capture sample purity via western blotting, flow cytometry measurements introduced additional challenges that still need to be addressed. Relatively strong 1T magnets were used to magnetically pellet cetuximab-MPs on the side of 1.5mL microcentrifuge tubes with an internal diameter of ~8mm. Despite this, isolated supernatants from restriction enzyme cleavage reactions appear to contain a significant population of MPs in the scatter profile generated by flow cytometry. Because cetuximab-MPs are much larger than EVs and should have a sufficiently larger increase in density, centrifugation of isolated supernatants at relatively low speeds around 3000-4000x g should provide sufficient speeds to separate residual MPs from released EVs.

Released EVs bound to whole cetuximab antibodies may also form chains or doublets that could be too large to distinguish from MPs based on scatter due to the swarm effect where multiple EVs are illuminated at the same time and measured as a single event.[95] Previous studies utilized shearing forces introduced by injecting stained EVs through progressively smaller gauge needles in order to ensure that flow cytometry measurements were performed on a homogenous

population of single EVs rather than doublets or larger aggregates.[40] We did not perform this step in order to evaluate the performance of the restriction enzyme-mediate release from cetuximab-MPs alone. However, future studies investigating the optimal procedures to prepare samples for flow cytometry analysis will determine if applying shearing forces to released EVs produce scatter profiles that can be resolved from MPs alone. Additionally, we could utilize maleimide conjugation of F(ab') cetuximab fragments to DNA oligomers instead of DBCO conjugation of whole cetuximab. F(ab') fragments only have one antigen binding site which would prevent multiple EVs from binding to a single antibody tethered to cetuximab-MPs.

Finally, no evaluation of purification efficiency in biofluids such as plasma, CSF, or urine was performed. Although the conditioned cell culture media from the HF bioreactor culture of DiFi cells contains a variety of irrelevant proteins, biofluids such as plasma are inherently more complex.[96] As the complexity of biological samples increase, the concentration of $EGFR^+$ EVs present may also become too low for a single cetuximab-MP purification strategy. In this case, additional capture antibody-DNA conjugates could be synthesized, and we could explore sequential antibody conjugated-MP purifications using more general EV markers to secure initial populations of EVs from complicated samples. For instance, samples could initially be incubated with anti-CD9 or anti-CD63 conjugated MPs to collect as many EVs as possible in the initial extraction before cleaving with ClaI restriction enzymes so that Cy3 is not transferred. EV collections would then need to be washed with large molecular weight cutoff filters to remove residual enzyme activity before they could be incubated with cetuximab-MPs and cleaved with BamHI to transfer Cy3 fluorescence.

FUTURE DIRECTIONS

Significant Aim 1

The targeted inhibition of $CD4^+$ T cells via nanoparticle formulated Egm was the primary application that motivated the studies presented in Chapter 2, but the potential applications of this research extend well beyond that initial goal. The maleimide-thiol conjugation strategy utilized in Chapter 2 is highly modular and could provide a suitable targeting strategy for a variety of drug delivery vehicles with clinical relevance. We highlighted the potential targeted delivery of immunosuppressive compounds in Chapter 2; however, many other classes of drugs such as corticosteroids, cytokine therapies, and small interfering RNA could benefit from targeted delivery. Chemotherapies are a classic example of this concept, because their administration often results in high levels of toxicity to cells of the immune system, hair follicles, and gastrointestinal tract. In fact, many of the founding studies that highlighted the clinical potential of PLGA nanoparticles were performed to improve the administration of chemotherapies, such as doxorubicin. Although PLGA nanoparticles may not be a suitable delivery vehicle for agents other than small molecule drugs, as long as a maleimide chemical group can be incorporated in the corona of these particles the same targeting benefits that were highlighted in Chapter 2 could be extended to these new areas. Additionally, antibody-DNA conjugates similar to those presented in Chapter 3 have recently been utilized to improve the administration of doxorubicin by utilizing DNA as a novel carrier for hydrophobic small molecules.[91] Should nanoparticle delivery of Egm fail *in vivo*, the antibody conjugate design concepts presented in Chapter 3 could be adapted to provide a GC targeting antibody-DNA conjugate delivery strategy for Egm similar to what was demonstrated with doxorubicin.[91]

The conjugation of anti-CD4 F(ab') antibody fragments on our particle formulation enabled the preferential delivery of Egm to helper T cells without the need to identify autoantigens that trigger an autoimmune response. Although this strategy could enable targeted suppression of a subpopulation of the adaptive immune system, true antigen specific tolerance would preserve as much of a patient's natural immunity as possible. If a patient's individual autoantigens could be identified, then alternative targeting strategies involving peptide-MHC/HLA conjugates could be developed so that only T cells with autoreactive T cell receptors would be depleted or inhibited. Several impactful studies published by Pere Santamaria's research group have recently demonstrated that peptide-MHC based nanomedicines can suppress the activity of autoimmune T cells without disturbing general or local immunity against infection and tumors.[97,98] The biggest obstacle currently preventing this type of approach from becoming standard practice is a lack of established target discovery and validation pipelines that could identify the autoantigens affecting patients on an individual level. However, recent developments in the manufacturing of anti-cancer neoantigen T cell therapies presented by BioNTech may soon enable a similar approach to be explored in autoimmunity to identify autoimmune peptide-HLA pairs that could be used to generate precision peptide-HLA nanomedicines.[99]

Significant Aim 2

The cetuximab-DNA conjugates presented in Chapter 3 were developed to enable the purification, non-destructive release, and fluorescent labeling of $EGFR^+$ EVs from complex biological samples. They were conjugated to superparamagnetic microparticles to provide an alternative purification strategy for downstream FAVS, but the technique may be better implemented in a 96-well plate format as others have recently demonstrated.[93] The 1.5 mL microcentrifuge tubes that were utilized in Chapter 3 are not ideal for high-throughput

applications. Beyond 8-10 samples it becomes increasingly difficult to process samples in a timely fashion without sacrificing sample quality. If automatic magnetic particle handlers, such as the Thermofisher KingFisher Flex purification system, were paired with a 96-well plate format using cetuximab-MPs, then the issues associated with disturbing magnetically generated pellets could be eliminated and automation of the sample processing steps could be achieved.

Instead of transferring liquids between microplates, the KingFisher system uses magnetic rods that are dipped into the wells of a microplate in order to mix and transfer magnetic particles between plates. Multiple plates could be prepared so that the KingFisher system could automate capture of EVs on cetuximab-MPs from biofluids, washing of cetuximab-MPs to remove impurities, and cleavage of DNA linkers with restriction enzymes to non-destructively release EVs from cetuximab-MPs within unique plates prepared for each step of the process. Furthermore, multiple capture antibody conjugated particles with unique fluorescent labels on the restriction enzyme cleavable DNA linkers could be incorporated into a single plate to provide multiplexed purification of EVs from biofluids. In this way, the KingFisher system could automatically guide the cetuximab-MPs through each part of the sample processing procedures presented in Chapter 3 so that the advantages of cetuximab-MPs sequential ultracentrifugation could be combined with the high-throughput format of a 96-well plate in order to enable high-throughput, multiplexed antigen specific purification of EVs.

Alternatively, the cetuximab-DNA conjugates could also be functionalized to the inside of an affinity chromatography column to remove the need for automatic magnetic bead handlers. In this way, biofluids could be flowed through affinity columns so that cetuximab-DNA conjugates could bind to EGFR EVs in the sample. Unbound components could then be washed out of columns by flowing wash buffer through the columns. Afterwards, elution buffer

containing restriction enzymes could be flowed through the columns to cleave the DNA linkers and elute captured EVs for downstream analysis.

Beyond diagnostic evaluation of EVs from biofluids in CRC and other cancers, the restriction enzyme cleavable DNA linkers that were developed in Chapter 3 could be useful for the purification of EV derived therapeutics for regenerative therapies.[100] EVs derived from stem cells and progenitor cells are currently under investigation to determine if they may have therapeutic effects comparable to their parental cells. Several diseases with unmet clinical needs, such as critical size bone defects, epidermolysis bullosa, and spinal cord injuries, could benefit from mesenchymal stromal cell (MSC)-derived EV therapies.[100] Heterogeneity among secreted EVs exists in regard to both vesicle size and functional cargo that may be of therapeutic value for regenerative medicine. Just like any pharmaceutical product, EV-based therapies must be rigorously characterized and purified in order to be GMP compliant. In addition to the removal of cellular debris, free or aggregated protein, and lipoprotein particles that are found in the media of MSC cultures, it may also be necessary to enrich EVs that contain the functional cargo of interest. If affinity-based purification strategies are employed to enrich EVs with specific functional cargo, then the restriction enzyme cleavable DNA linkers developed in Chapter 3, or a similar equivalent, could enable high-throughput purification and non-destructive release of EV therapeutics using KingFisher particle handlers or other scalable forms of affinity purification that utilize capture antibodies. The manufacturing and enrichment processes of EV therapeutics is still under investigation by many pharmaceutical and biotechnology companies. To this date, no EV-based therapeutics have been approved for human use but the cetuximab-DNA conjugates developed in Chapter 3 could enable significant strides to be made in the research and

development of scalable manufacturing procedures for future therapies that could lead to major advancements in regenerative medicine.

APPENDIX A

SUPPLEMENTARY INFORMATION FOR CHAPTER 1

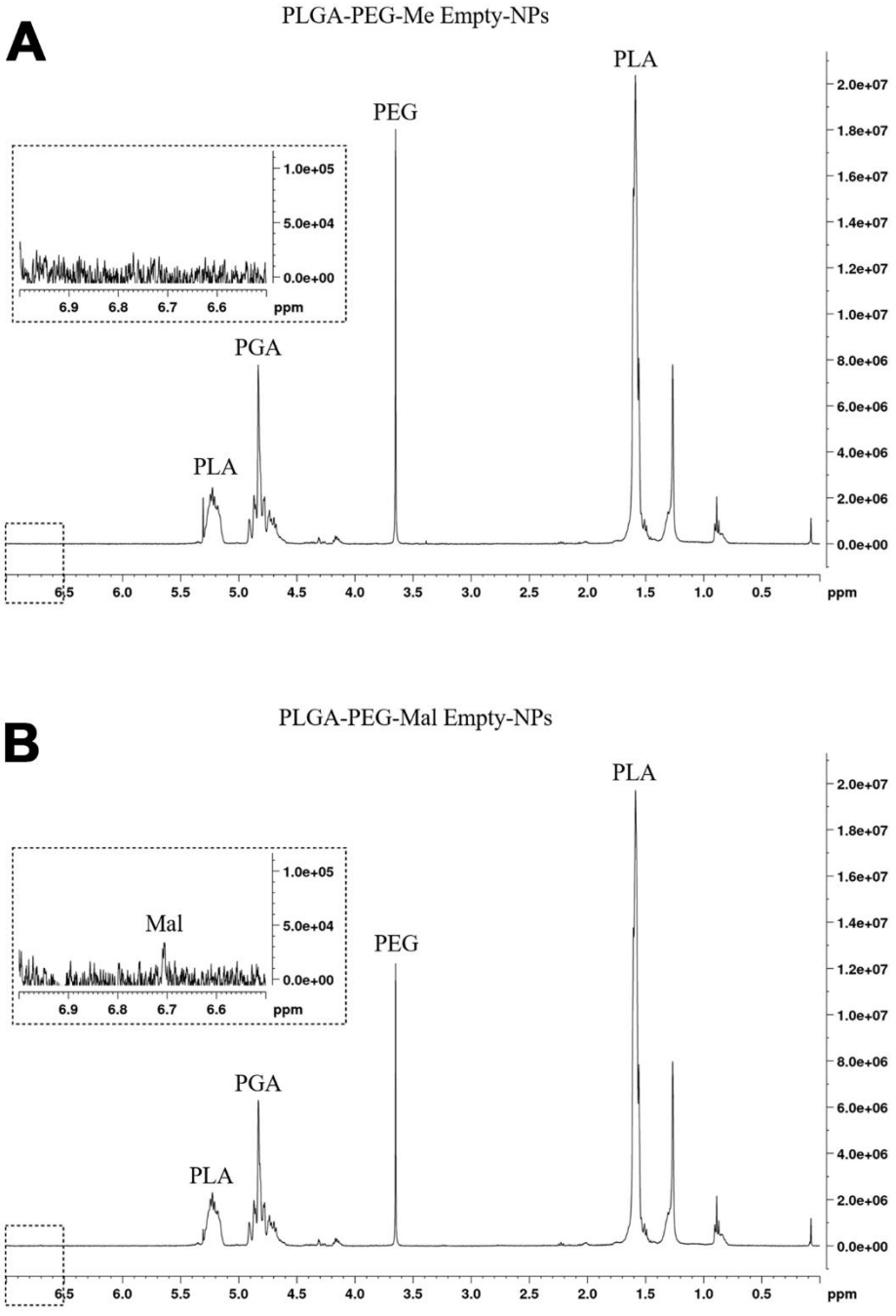

Figure A.1 Undecorated nanoparticle chemical characterization.

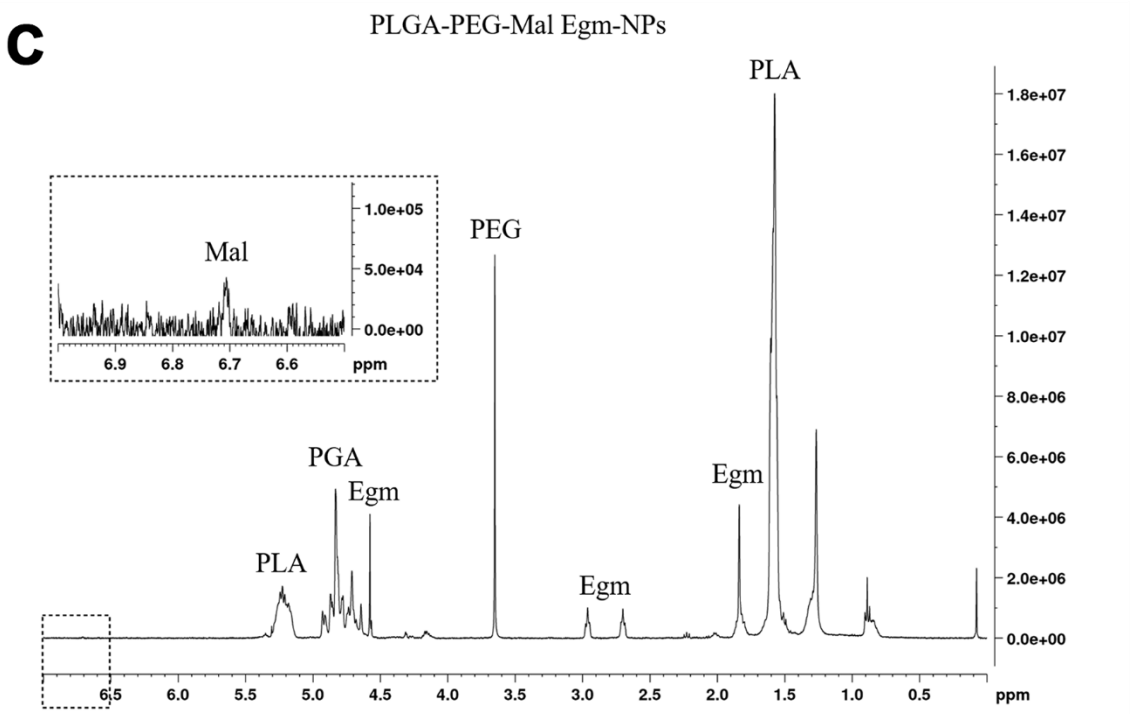

Figure A.1 (Continued) Undecorated nanoparticle chemical characterization.

Notes: (**A**) NMR analysis of nanoparticles made with PLGA(10 kDa) and PLGA(10 kDa)-PEG(5 kDa)-methyl. (**B**) NMR analysis of nanoparticles made with PLGA(10 kDa) and PLGA(10 kDa)-PEG(5 kDa)-maleimide. **(C)** NMR analysis of nanoparticles made with PLGA(10 kDa) and PLGA(10 kDa)-PEG(5 kDa)-maleimide loaded with Egm. All particles were characterized using 1H nuclear magnetic resonance spectroscopy (Bruker, 400 MHz). All NMR was performed in deuterated chloroform.
Abbreviations: PLA, poly(lactic acid); PGA, poly(glycolic acid); PEG, polyethylene glycol; Mal, maleimide; Me, methyl; Egm, Eggmanone.

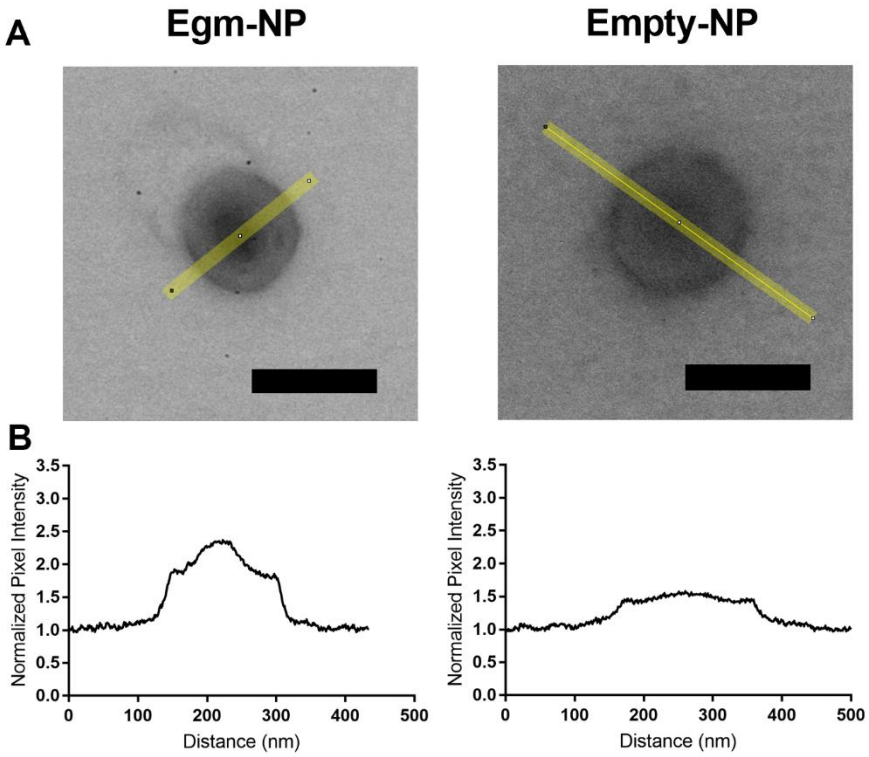

Figure A.2 Line profile analysis of contrast in nanoparticle cores.

Notes: (**A**) Representative TEM micrographs of Egm-NP (left) and empty-NP (right) with superimposed line profile region of interest (ROI)s generated in ImageJ. (**B**) Quantification of pixel intensity along the length of the yellow line profile ROIs indicated above for Egm-NP (left panels) and empty-NP (right panels). Pixel intensities were normalized to the background intensity surrounding each nanoparticle. Scale bars represent 200 nm distances.
Abbreviations: Egm-NP, Egm-loaded nanoparticle; empty-NP, empty-nanoparticle.

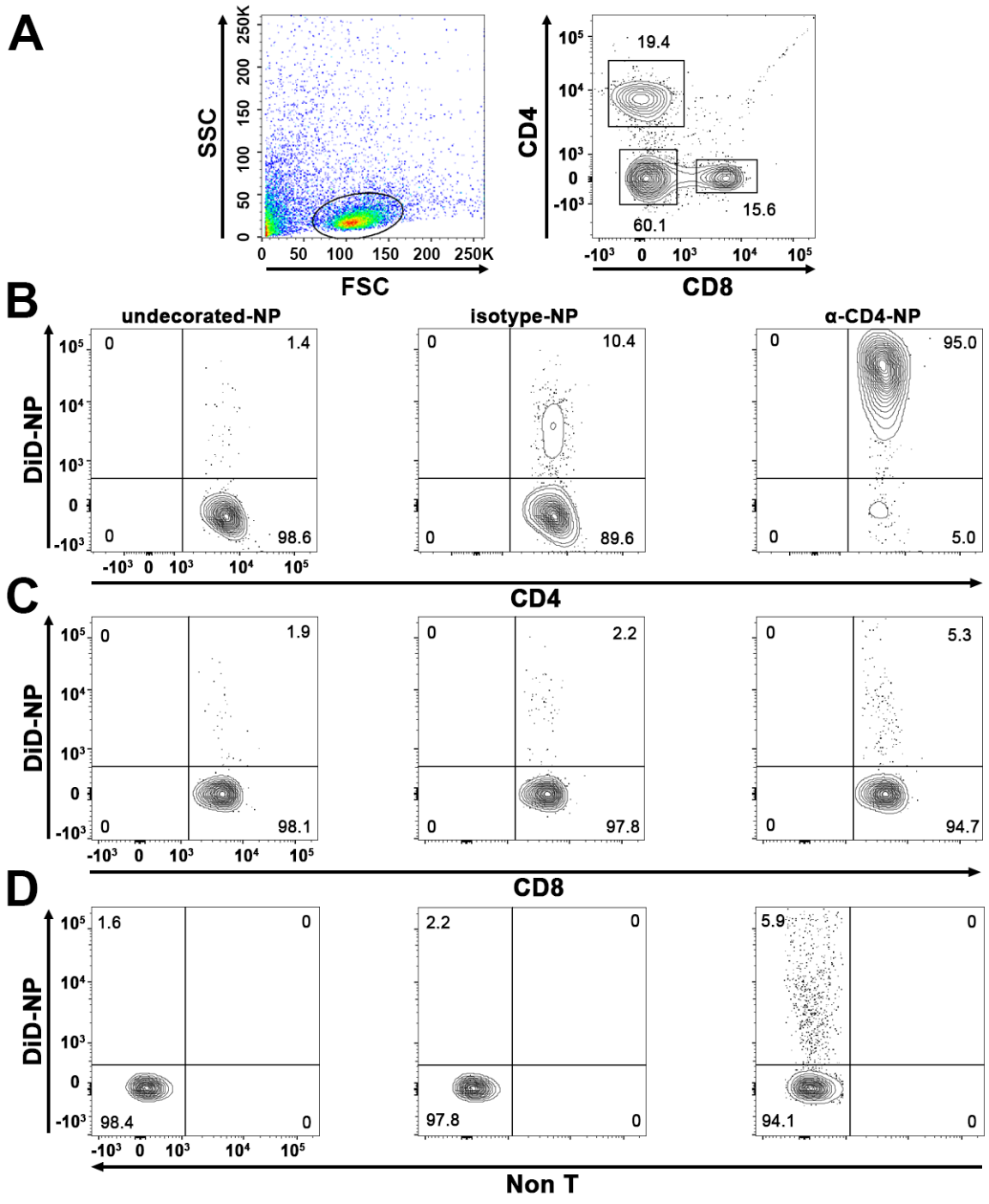

Figure A.3 Expanded flow cytometry gating strategy used in targeting experiments.

Notes: (**A**) Flow cytometry gating strategy used to analyze the targeting specificity of anti-CD4 decorated, DiD-NPs after incubation of whole splenocytes with either undecorated, isotype control decorated, or anti-CD4 decorated DiD-NPs suspended in 1X PBS. The lymphocyte population was selected from forward versus side scatter plots. $CD4^+$ T cells, $CD8^+$ T cells, and

non-T cells were selected from CD4 versus CD8 plots. Corresponding nanoparticle bound cell populations were then selected according to DiD staining intensity. (**B**) Nanoparticle bound $CD4^+$ T cells indicated by cell populations in upper right-hand quadrants. (**C**) Nanoparticle bound $CD8^+$ T cells indicated by cell populations in upper right-hand quadrants. (**D**) Nanoparticle bound non-T cells indicated by cell populations in upper left-hand quadrants. Data shown are representative staining results from 1 of 3 experiments. The flow cytometry probe for CD4 staining utilized an antibody clone that recognized a different epitope of CD4 than those used to decorate nanoparticles. Splenocytes were derived from female C57BL/6J mice.
Abbreviations: SSC, side scatter; FSC, forward scatter; DiD-NP, DiD-loaded nanoparticle; undecorated-NP, undecorated DiD-NP; isotype-NP, isotype control antibody fragment decorated DiD-NP; α-CD4-NP, anti-CD4 antibody fragment decorated DiD-NP; Non T, non-T cells.

APPENDIX B

SUPPLEMENTARY INFORMATION FOR CHAPTER 2

Table B.1 Cetuximab-Cy3 DNA degree of labeling calculated from UV-Vis spectroscopy.

DBCO per Antibody	Cy3 per Antibody
31.47 ± 14.03	1.086 ± 0.1398
N = 3	N= 3

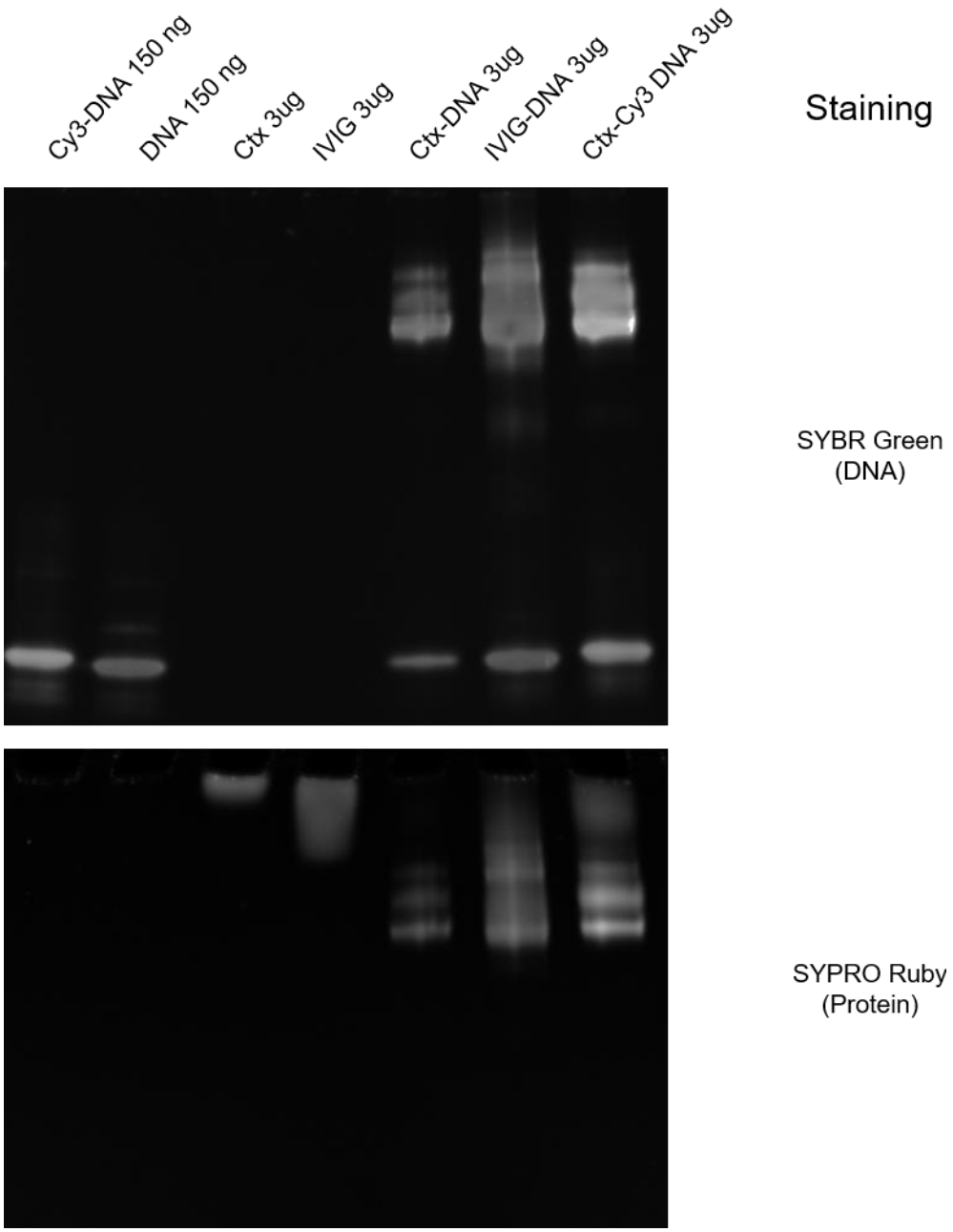

Figure B.1 DNA conjugation increases the electrophoretic mobility of cetuximab and IVIG conjugates.

Subsequent SYBR green and SYPRO Ruby staining of the same native PAGE. Samples loaded in lanes 1-2 represent DNA linkers with and without Cy3-modification. Samples loaded in lanes 3-4 represent the native cetuximab and IVIG antibodies used to prepare conjugates. Samples loaded in lanes 5-6 represent antibody-DNA conjugates of cetuximab and IVIG made with either DNA linker.

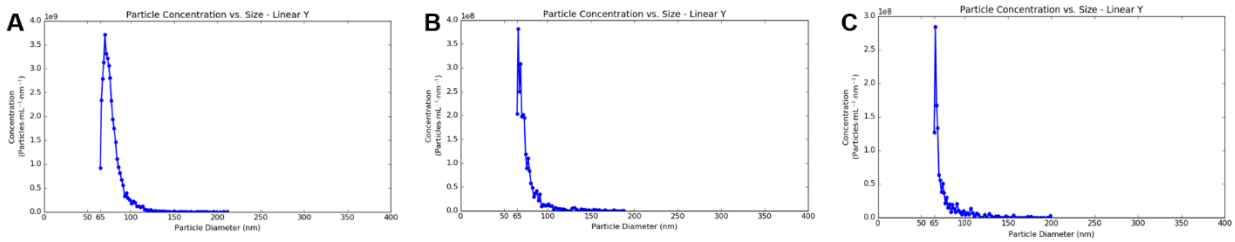

Analysis	DiFi Concentrate
Size range min (nm):	65.0
Size range max (nm):	400.0
Total concentration (/mL):	5.98E+10
Number of particles detected:	6623
Statistical error in concentration (%):	1.2%
D10 (nm):	68.4
D50 (nm):	78.4
D90 (nm):	91.8

Analysis	Ctx Cap. BamHI
Size range min (nm):	65.0
Size range max (nm):	400.0
Total concentration (/mL):	3.61E+09
Number of particles detected:	1035
Statistical error in concentration (%):	3.4%
D10 (nm):	65.0
D50 (nm):	71.7
D90 (nm):	85.1

Analysis	IVIG Cap. BamHI
Size range min (nm):	65.0
Size range max (nm):	400.0
Total concentration (/mL):	1.71E+09
Number of particles detected:	362
Statistical error in concentration (%):	6.2%
D10 (nm):	65.0
D50 (nm):	71.7
D90 (nm):	91.8

Figure B.2 Spectradyne analysis of released EVs from 20:1 cetuximab-MPs.

(A) 1:10 dilution of $EGFR^+$ EVs from DiFi concentrate material. (B) 1:10 dilution of $EGFR^+$ EVs released from cetuximab-MPs after BamHI cleavage (C) 1:10 dilution of $EGFR^+$ EVs released from IVIG-MPs after BamHI cleavage. Cetuximab- and IVIG-DNA conjugates used for this experiment were made with non-Cy3-modifed DNA.

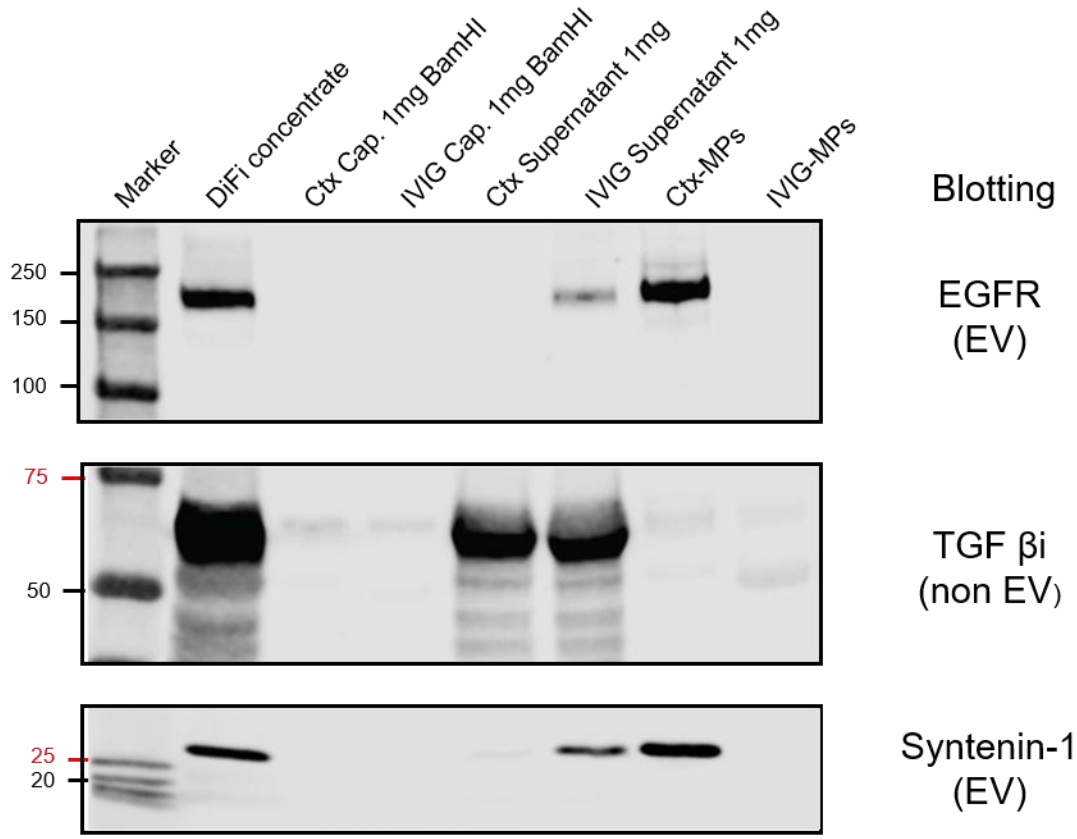

Figure B.3 Western blot of 20:1 cetuximab-MP EGFR$^+$ EV capture and release.

Western blot of BamHI cleaved EGFR$^+$ EVs after capture with 20 µg cetuximab/IVIG :1 mg Dynabeads. Cetuximab- and IVIG-DNA conjugates used for this experiment were made with non-Cy3-modifed DNA. The sample loaded in lane 2 represents the starting DiFi concentrate material. Samples loaded in lanes 3-4 represent the captured material that was released from Cetuximab/IVIG beads using BamHI cleavage of DNA linkers. Samples loaded in lanes 5-6 represent the supernatant that was overloaded to show residual EGFR and synthenin-1. Samples 7-8 represent the captured material that remained on the MPs after cleavage with BamHI. These samples were prepared by boiling the respetive beads in the same volume of sample buffer. Beads were removed from these samples prior to loading via magentic separation.

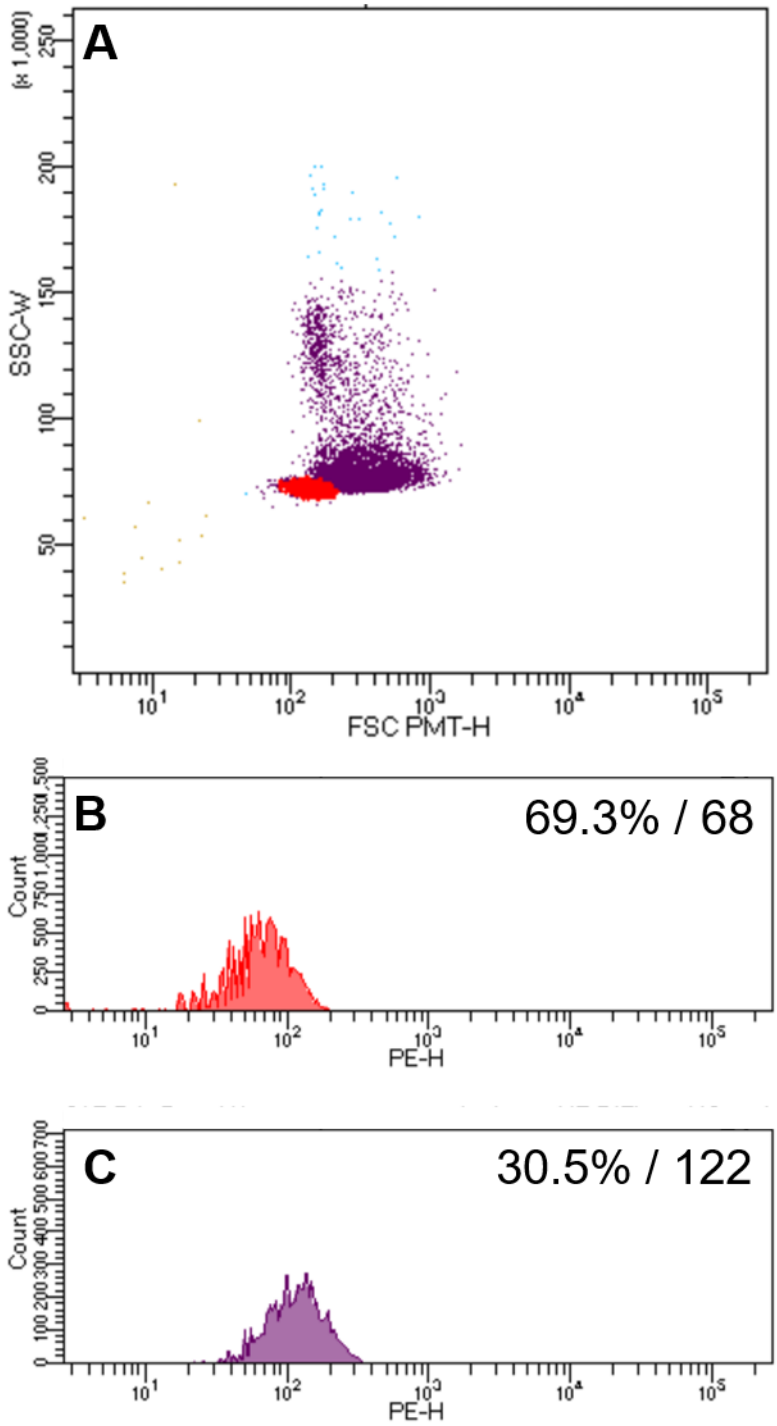

Figure B.4 Cy3 fluorescence of unconjugated Dynabeads.

(**A**) Scatter profile of unconjugated Dynabeads. (**B**) Cy3 fluorescence of Dynabead singlets. (**C**) Cy3 Fluorescence of Dynabeads that were not singlets.

APPENDIX C

ADDITIONAL RESEARCH PERFORMED

PEGylated PLGA Particle Size and Zeta Potential after Conjugation of F(ab') Antibody Fragments

Changes in PEGylated PLGA particle size and zeta potential after conjugation of F(ab') antibody fragments were investigated using DLS. Isotype control F(ab') antibody fragments conjugated to Egm nanoparticles formulated as in Chapter 2 resulted in an increase in the Z-average hydrodynamic diameter compared to unconjugated Egm nanoparticles when measured by DLS (Figure C.1). We investigated whether this could have been due to aggregation events resulting from F(ab') conjugation by centrifuging these particles and measuring pelleted nanoparticles and those left in the supernatant with DLS. Particles recovered from centrifuged pellets were closer in size to F(ab') conjugated particle suspensions, while those recovered from the supernatant were closest in size to unconjugated particles. These results suggest that a portion of nanoparticles may be increasing in size during F(ab') conjugation, but DLS is not best suited for measuring distinct populations of nanoparticles that are close in size.

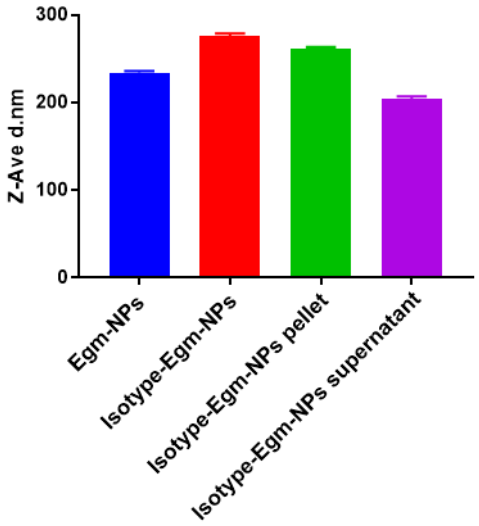

Figure C.1 Hydrated size measurements of F(ab') conjugated Egm nanoparticles

Notes: Z-average diameter of resuspended Egm nanoparticle with and without conjugation of isotype control F(ab') antibody fragments. Additional measurements of F(ab') conjugated particles were made after centrifugation to determine if aggregates formed during conjugation procedures (n = 1 sample, 4 measurements made for each sample).

Biodistribution of CD4$^+$ T cell Targeting Nanoparticles.

After successfully achieving *ex vivo* CD4$^+$ T cell targeting specificity in Chapter 2, we evaluated the *in vivo* capabilities of the same nanoparticle formulation in immunocompetent C57BL/6J mice. 18 hours after administration, the spleen, inguinal lymph nodes, and liver, were collected for evaluation of nanoparticle biodistribution and targeting specificity. No detectable DiD signal was observed in the lymph nodes, and we believe this to be due to the lack of a draining lymph node following systemic administration.

Similar to the observations from Chapter 2 utilizing *ex vivo* splenocyte cultures, α-CD4 decorated particles achieved ~ 21% CD4$^+$ T cell staining in the spleen, and significantly increased targeting specificity for CD4$^+$ T cells compared to isotype (~7%) controls. Additionally, targeting of CD4$^+$ T cells by α-CD4 decorated particles in the spleen was

confirmed by significantly elevated staining levels compared to $CD8^+$ T cells (~8%) and non-T cells (~6%) (Figure C.2A). No statistical differences in staining levels were observed for isotype control decorated particles, suggesting that binding was the result of non-specific interactions.

CD4 targeting specificity was not conserved in the liver, a known biological sequestration site of nanoparticle therapeutics, where antibody fragment decoration had no effect on targeting specificity, and the majority of particles were bound to non-T cells (~15%) (Figure C.2B). Macrophage populations in the liver often nonspecifically uptake nanoparticles < 500 nm in diameter over a wide range of formulations, and nanoparticles greater than 250 nm will often accumulate in the liver after systemic administration.[73,74,101,102] Therefore, the majority of DiD-loaded nanoparticles in the liver were most likely accumulated by non-T cell populations because of non-specific uptake by macrophages. Despite this, CD4 targeting specificity levels for α-CD4 decorated particles were higher in the spleen compared to isotype and α-CD4 decorated particles in the liver. These results suggest that the intrinsic lymphatic trafficking abilities of helper T cells circulating in the blood may provide preferential accumulation of α-CD4 decorated nanoparticles in the spleen that can be leveraged for therapeutic inhibition of germinal center responses.

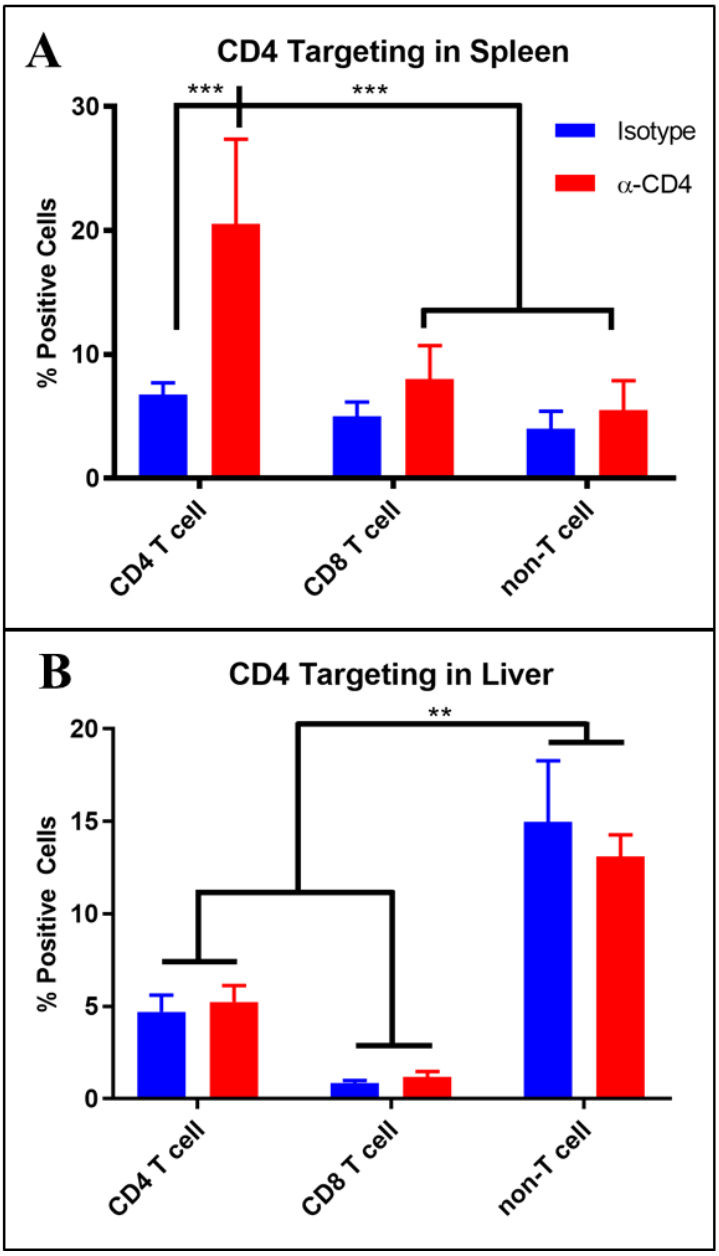

Figure C.2 In vivo $CD4^+$ T cell targeting.

Notes: (**A**) Quantification of DiD positive immune cells isolated from the spleen 18 hours after retro-orbital injection of 2 mg of either isotype control decorated, or α-CD4 decorated fluorescent nanoparticles suspended in 1x PBS. The flow cytometry probe for CD4 staining utilized an antibody clone that recognized a different epitope of CD4 than those used to decorate nanoparticles. (**B**) Quantification of DiD positive immune cells isolated from the spleen 18 hours after retro-orbital injection of 2 mg of either isotype control decorated, or α-CD4 decorated fluorescent nanoparticles suspended in 1x PBS. The flow cytometry probe for CD4 staining utilized an antibody clone that recognized a different epitope of CD4 than those used to decorate nanoparticles. The mass of nanoparticles injected was re-suspended in a 200 µL injection volume (n=4 mice, **p < 0.005 and *** p = 0.0001, ordinary Two-way ANOVA with multiple

comparisons test was performed to evaluate statistical significance.) This figure was adapted from Christopher Haycook's 2018 MS thesis.

REFERENCES

1. Chiu, M. L., Goulet, D. R., Teplyakov, A. & Gilliland, G. L. Antibody Structure and Function: The Basis for Engineering Therapeutics. *Antibodies* **8**, (2019).

2. Joubert, N., Beck, A., Dumontet, C. & Denevault-sabourin, C. Antibody- Drug Conjugates : The Last Decade. *Pharmaceuticals* **13**, (2020).

3. Marder, W., Vinet, É. & Somers, E. C. Rheumatic autoimmune diseases in women and midlife health. *Women's Midlife Heal.* **1**, 1–8 (2015).

4. Miyagawa, I., Kubo, S. & Tanaka, Y. A wide perspective of targeted therapies for precision medicine in autoimmune diseases. *Expert Rev. Precis. Med. Drug Dev.* **5**, 447–453 (2020).

5. Domeier, P., Schell, S. & Rahman, Z. Spontaneous germinal centers and autoimmunity. *Autoimmunity* **50**, 4–18 (2017).

6. Souness, J. E., Aldous, D. & C., S. Immunosupressive and anti-inflammatory effects of cyclic AMP phosphodiesterase (PDE) type 4 inhibitors. *Immunopharmacology* 127–162 (2000).

7. Burnouf, C. and Pruniaux, M. P. Recent advances in PDE4 inhibitors as immunoregulators and anti-inflammatory drugs. *Curr. Pharm. Des.* 1255–1296 (2002).

8. Castro, A., Jerez, M. J., Gil, C., and Martinez, A. Cyclic nucleotide phosphodiesterases and their role in immunomodulatory responses: advances in the development of specific phosphodiesterase inhibitors. *Med. Res. Rev* 229–244 (2005).

9. Schett, G., Sloan, V. S., Stevens, R. M. & Schafer, P. Apremilast : a novel PDE4 inhibitor in the treatment of autoimmune and inflammatory diseases. *Ther. Adv. Musculoskelet. Dis.* **2**, 271–278 (2010).

10. Lerner, A., and Epstein, P., M. Cyclic nucleotide phosphodiesterases as targets for treatment of haematological malignancies. *Biochem. J* 21–41 (2006).

11. Bjørgo, E. and Taske´n, K. Novel mechanism of signaling by CD28. *Immunol Lett* 1–6 (2010).

12. Essayan, D.M., Huang, S.K., Kagey-Sobotka, A. and & Lichtenstein, L. M. Differential efficacy of lymphocyte- and monocyte-selective pretreatment with a type 4 phosphodiesterase inhibitor on antigendriven proliferation and cytokine gene expression. *J Allergy Clin Immunol* 28–37 (1997).

13. Essayan, D.M., Huang, S.K., Undem, B. J. & Kagey-Sobotka, A. and Lichtenstein, L. M. Modulation of antigen- and mitogen-induced proliferative responses of peripheral blood mononuclear cells by nonselective and isozyme selective cyclic nucleotide phosphodiesterase inhibitors. *J Immunol* 3408–3416 (1994).

14. Vang, A. G. *et al.* Differential Expression and Function of PDE8 and PDE4 in Effector T cells : Implications for PDE8 as a Drug Target in Inflammation. *Front. Pharmacol.* **7**, 1–9 (2016).

15. Peter, D. *et al.* Differential Expression and Function of Phosphodiesterase 4 (PDE4) Subtypes in Human Primary CD4+ T cells: Predominante Role of PDE4D. *J. Immunol.* **178**, 4820–4831 (2007).

16. Jimenez, J.L., Punzon, C., Navarro, J. & Munoz-Fernandez, M.A. and Fresno, M. Phosphodiesterase 4 inhibitors prevent cytokine secretion by T lymphocytes by inhibiting nuclear factor-kB and nuclear factor of activated T cells activation. *J Pharmacol Exp Ther* 753–759 (2001).

17. Abrahamsen, H. *et al.* TCR- and CD28-Mediated Recruitment of Phosphodiesterase 4 to Lipid Rafts Potentiates TCR Signaling. *J. Immunol.* 4847–4858 (2004). doi:10.4049/jimmunol.173.8.4847

18. Amgen. To Evaluate the Preliminary Safety, Tolerability, Pharmacokinetics, Pharmacodynamics and Efficacy of CC-11050 in Subjects With Discoid Lupus Erythematosus and Subacute Cutaneous Lupus Erythematosus. *Good Clinical Practice Network* (2013).

19. Celgene. Safety Study of Clinical and Immune Effects of Phosphodiesterase 4 (PDE-4) Inhibitor in Cutaneous Lupus Patients. *ClinicalTrials.gov* (2010).

20. Galindo-Rodriguez, G. *et al.* Pentoxifylline in the treatment of refractory nephrotic syndrome secondary to lupus nephritis. *J. Rheumatol.* **30**, (2003).

21. Lugnier, C. Cyclic nucleotide phosphodiestase (PDE) implication in lupus erythematosus: Effect of a new PDE4 inhibitor. in *8th Molecular Immunology & Immunogenetics Congress* (2017).

22. Yougbare, I., Boire, G., Roy, M., Lugnier, C. & Rouseau, E. NCS 613 exhibits anti-inflammatory effects on PBMCs from lupus patients by inhibiting p38 MAPK and NF-κB signalling pathways while reducing proinflammatory cytokine production. *Can. J. Physiol. Pharmacol.* (2013).

23. Schafer, P. H. *et al.* Phosphodiesterase 4 in inflammatory diseases : Effects of apremilast in psoriatic blood and in dermal myofibroblasts through the PDE4/CD271 complex. *Cell. Signal.* **28**, 753–763 (2016).

24. Keravis, T. *et al.* Disease Progression in MRL/lpr Lupus-Prone Mice Is Reduced by NCS 613, a Specific Cyclic Nucleotide Phosphodiesterase Type 4 (PDE4) Inhibitor. *PLoS One* **7**, (2012).

25. Giembycz, M. A. Can the anti-inflammatory potential of PDE4 inhibitors be realized: guarded optimism or wishful thinking? *Br. J. Pharmacol* **155**, 288–290 (2008).

26. Spina, D. PDE4 inhibitors: current status. *Br. J. Pharmacol* **155**, 308–315 (2008).

27. Tenor, H., Hatzelmann, A., Beume, R., Lahu, G., Zech, K., and Bethke, T. D. Pharmacology, clinical efficacy, and tolerability of phosphodiesterase4 inhibitors: impact of human pharmacokinetics. *Handb. Exp. Pharmacol* **204**, 85–119 (2011).

28. Poole, R. M., and Ballantyne, A. D. Apremilast: first global approval. *Drugs* **74**, 825–837 (2014).

29. RS, K. Apremilast in Patients with Lupus Rashes [abstract]. *Arthritis Rheumatol* **69 (suppl**, (2017).

30. De Souza, A., Strober, B., Merola, J., Oliver, S. & Franks, A. J. Apremilast for discoid lupus erythematosus: results of a phase 2, open-label, single-arm, pilot study. *J Drugs Dermatol* **11**, 1224–1226 (2012).

31. Williams, C. H. *et al.* An In vivo Chemical Genetic Screen Identifies Phosphodiesterase 4 as a Pharmacological Target for Hedgehog signaling Inhibition Charles. *Cell Rep.* **11**, 43–50 (2015).

32. Hong, C. *et al.* Compounds and Methods for Inhibiton of Hedgehog Signaling and Phosphodiesterase. (2016).

33. Honary, S. & Zahir, F. Effect of Zeta Potential on the Properties of Nano-Drug Delivery Systems - A Review (Part 1). *Trop. J. Pharm. Res.* **12**, 255–264 (2013).

34. Hoshyar, N., Gray, S., Han, H. & Bao, G. The effect of nanoparticle size on in vivo pharmacokinetics and cellular interaction. *Nanomedicine* **11**, 673–692 (2016).

35. Schudel, A., Francis, D. M., Thomas, S. N. & Francis, D. M. Material design for lymph node drug delivery. *Nat. Rev. Mater.* **4**, 415–428 (2020).

36. Maeda, H. Toward a full understanding of the EPR effect in primary and metastatic tumors as well as issues related to its heterogeneity. *Adv. Drug Deliv. Rev.* **91**, 3–6 (2015).

37. Fröhlich, E. The role of surface charge in cellular uptake and cytotoxicity of medical nanoparticles. *Int. J. Nanomedicine* **7**, 5577–5591 (2012).

38. Kishimoto, T. K. & Maldonado, R. A. Nanoparticles for the induction of antigen-specific immunological tolerance. *Front. Immunol.* **9**, (2018).

39. Siddiqui, M. Z. Monoclonal antibodies as diagnostics; An appraisal. *Indian J. Pharm. Sci.* **72**, 12–17 (2010).

40. Higginbotham, J. N. *et al.* Identification and characterization of EGF receptor in individual exosomes by fluorescence-activated vesicle sorting. *J. Extracell. Vesicles* **5**, 1–15 (2016).

41. Guo, Y. *et al.* Effects of exosomes on pre-metastatic niche formation in tumors. *Mol. Cancer* **18**, 1–11 (2019).

42. Zijlstra, A. & Di Vizio, D. Size matters in nanoscale communication. *Nat. Cell Biol.* **20**, 228–230 (2018).

43. Van der Vos, K. E. *et al.* Directly visualized glioblastoma-derived extracellular vesicles transfer RNA to microglia/macrophages in the brain. *Neuro. Oncol.* **18**, 58–69 (2016).

44. Jabalee, J., Towle, R. & Garnis, C. The Role of Extracellular Vesicles in Cancer : Cargo , Function , and Therapeutic Implications. *Cells* **7**, 1–23 (2018).

45. Wu, K., Xing, F., Wu, S., Watabe, K. & Salem, W. Extracellular vesicles as emerging targets in cancer: recent development from bench to bedside. *Biochim. Biophys. Acta* **1868**, 538–563 (2018).

46. Pabla, B., Bissonnette, M. & Konda, V. J. Colon cancer and the epidermal growth factor recepor: Current treatment paradigms, the importance of diet, and the role of chemoprevention. **6**, 133–142 (2015).

47. Zhang, H. *et al.* Exosome-delivered EGFR regulates live microenvironment to promote gastric cancer liver metastasis. *Nat. Commun.* (2017). doi:10.1038/ncomms15016

48. Kharmate, G., Hosseini-beheshti, E. & Caradec, J. Epidermal Growth Factor Receptor in Prostate Cancer Derived Exosomes. *PLoS One* 1–14 (2016). doi:10.1371/journal.pone.0154967

49. Jeppesen, D. K. *et al.* Reassessment of Exosome Composition. *Cell* **177**, 428–445.e18 (2019).

50. Patel, G. K., Khan, M. A., Zubair, H. & Srivastava, S. K. Comparative analysis of exosome isolation methods using culture supernatant for optimum yield , purity and downstream applications. *Sci. Rep.* **9**, 1–10 (2019).

51. Bellotti, C., Lang, K., Kuplennik, N., Sosnik, A. & Steinfeld, R. High-grade extracellular vesicles preparation by combined size-exclusion and affinity chromatography. *Sci. Rep.* **11**, 1–13 (2021).

52. Liga, A., Vliegenthart, A. D. B., Oosthuyzen, W., Dear, J. W. & Kersaudy-Kerhoas, M. Exosome isolation: A microfluidic road-map. *Lab Chip* **15**, 2388–2394 (2015).

53. Yumura, K. *et al.* Mutations for decreasing the immunogenicity and maintaining the function of core streptavidin. *Protein Sci.* **22**, 213–221 (2013).

54. McHugh, M. D. *et al.* Paracrine co-delivery of TGF-β and IL-2 using CD4-targeted nanoparticles for induction and maintenance of regulatory T cells. *Biomaterials* **59**, 172–181 (2015).

55. Chinol, M. *et al.* Biochemical modifications of avidin improve pharmacokinetics and biodistribution, and reduce immunogenicity. *Br. J. Cancer* **78**, 189–197 (1998).

56. Fontaine, S. D. *et al.* Long-Term Stabilization of Maleimide − Thiol Conjugates. *Bioconjug. Chem.* **26**, 145–152 (2015).

57. Kalia, D., Malekar, P. V & Parthasarathy, M. Exocyclic Olefinic Maleimides : Synthesis and Application for Stable and Thiol-Selective Bioconjugation. *Angewante chemie Int. Ed.* **55**, 1432–1435 (2016).

58. Jones, J., Starkey, J. & Kleinhofs, A. Toxicity and mutagenicity or sodium azide in mammalian cell cultures. *Mutat. Res.* **77**, 7979 (1980).

59. Haycook, C. P. *et al.* PEGylated PLGA Nanoparticle Delivery of Eggmanone for T Cell Modulation : Applications in Rheumatic Autoimmunity. *Int. J. Nanomedicine* **15**, 1215–1228 (2020).

60. Vaughan, S. & Dawe, H. R. Common themes in centriole and centrosome movements. *Trends Cell Biol.* **21**, 57–66 (2011).

61. De La Roche, M. *et al.* Hedgehog signaling controls T cell killing at the immunological synapse. *Science (80-.).* **342**, 1247–1250 (2013).

62. Smelkinson, M. The Hedgehog Signaling Pathway Emerges as a Pathogenic Target. *J. Dev. Biol.* **5**, 14 (2017).

63. Crompton, T., Outram, S. V. & Hager-Theodorides, A. L. Sonic hedgehog signalling in T-cell development and activation. *Nat. Rev. Immunol.* **7**, 726–735 (2007).

64. Chan, V. S. F. *et al.* Sonic hedgehog promotes CD4+T lymphocyte proliferation and modulates the expression of a subset of CD28-targeted genes. *Int. Immunol.* **18**, 1627–1636 (2006).

65. Kupfer, A. & Singer, S. J. The specific interaction of helper T cells and antigen-presenting B cells. IV. Membrane and cytoskeletal reorganizations in the bound T cell as a function of antigen dose. *J. Exp. Med.* **170**, 1697–713 (1989).

66. Xie, C., Ramirez, A., Wang, Z., Chow, M. S. S. & Hao, J. A simple and sensitive HPLC–MS/MS method for quantification of eggmanone in rat plasma and its application to pharmacokinetics. *J. Pharm. Biomed. Anal.* (2018). doi:10.1016/j.jpba.2018.01.009

67. Song, G., Petschauer, J., Madden, A. & Zamboni, W. Nanoparticles and the Mononuclear Phagocyte System: Pharmacokinetics and Applications for Inflammatory Diseases. *Curr. Rheumatol. Rev.* **10**, 22–34 (2014).

68. Cao, S. *et al.* Optimization and comparison of CD4-targeting lipid–polymer hybrid nanoparticles using different binding ligands. *J. Biomed. Mater. Res. - Part A* **106**, 1177–1188 (2018).

69. ThermoFisher. Lipophilic Tracers. 1–6 (2008). Available at: https://www.thermofisher.com/order/catalog/product/D7757.

70. Malvern Instruments Limited. Comparison of statistical measures reported by NTA and DLS techniques. *Retrieved from: www.malvern.com* (2015).

71. Schmid, D. *et al.* T cell-targeting nanoparticles focus delivery of immunotherapy to improve

antitumor immunity. *Nat. Commun.* **8**, 1–11 (2017).

72. Gerberick, G. F., Cruse, L. W., Miller, C. M., Sikorski, E. E. & Ridder, G. M. Selective modulation of t cell memory markers CD62L and CD44 on murine draining lymph node cells following allergen and irritant treatment. *Toxicol. Appl. Pharmacol.* **146**, 1–10 (1997).

73. Li, S.-D. & Huang, L. Pharmacokinetics and biodistribution of nanoparticles. *Mol Pharm* **5**, 496–504 (2008).

74. Moghimi, S. M., Hunter, A. C. & Andresen, T. L. Factors Controlling Nanoparticle Pharmacokinetics: An Integrated Analysis and Perspective. *Annu. Rev. Pharmacol. Toxicol.* **52**, 481–503 (2012).

75. Olivier, J. C., Huertas, R., Hwa, J. L., Calon, F. & Pardridge, W. M. Synthesis of pegylated immunonanoparticles. *Pharm. Res.* **19**, 1137–1143 (2002).

76. Hirenkumar K. Makadia1 and Steven J. Siegel2, H. Poly Lactic-co-Glycolic Acid (PLGA) as Biodegradable Controlled Drug Delivery Carrier Hirenkumar. *Polym.* **3**, 1377–1397 (2011).

77. Ademokun, A. A. & Dunn-Walters, D. Immune Responses: Primary and Secondary. *Encycl. Life Sci.* (2010). doi:10.1038/npg.els.0000947

78. Jackson, S. *et al.* B cell IFN-γ receptor signaling promotes autoimmune germinal centers via cell-intrinsic induction of BCL-6. *J. Exp. Med.* **213**, 733–750 (2016).

79. Sigismund, S., Avanzato, D. & Lanzetti, L. Emerging functions of the EGFR in cancer. *Mol. Oncol.* **12**, 3–20 (2018).

80. Schlessinger, J. Receptor tyrosine kinases: Legacy of the first two decades. *Cold Spring Harb. Perspect. Biol.* **6**, 1–15 (2014).

81. Vincenzi, B., Zoccoli, A., Pantano, F., Venditti, O. & Galluzzo, S. CETUXIMAB: From Bench to Bedside. *Curr. Cancer Drug Targets* **10**, 80–95 (2010).

82. Yarden, Y. & Pines, G. The ERBB network: At last, cancer therapy meets systems biology. *Nat. Rev. Cancer* **12**, 553–563 (2012).

83. Higginbotham, J. N. *et al.* Amphiregulin Exosomes Increase Cancer Cell Invasion. *Curr. Biol.* **21**, 779–786 (2011).

84. Théry, C., Ostrowski, M. & Segura, E. Membrane vesicles as conveyors of immune responses. *Nat. Rev. Immunol.* **9**, 581–593 (2009).

85. Cai, S. *et al.* Immuno-modified superparamagnetic nanoparticles via host-guest interactions for high-purity capture and mild release of exosomes. *Nanoscale* **10**, 14280–14289 (2018).

86. Löf, L. *et al.* Detecting individual extracellular vesicles using a multicolor in situ proximity ligation assay with flow cytometric readout. *Sci. Rep.* **6**, 1–9 (2016).

87. Wiener, J., Kokotek, D., Rosowski, S., Lickert, H. & Meier, M. Preparation of single- and double-oligonucleotide antibody conjugates and their application for protein analytics. *Sci. Rep.* **10**, 1–11 (2020).

88. Yan, I., Shukla, N., Borrelli, D. & Patel, T. Use of a Hollow Fiber Bioreactor to Collect Extracellular Vesicles from Cells in Culture. in *Extracellular RNA-Methods and Protocols* (ed. Patel, T.) 35–41 (Springer, 2018). doi:10.1007/978-1-4939-7652-2_4

89. Cimorelli, M., Nieuwland, R., Varga, Z. & van der Pol, E. Standardized procedure to measure the size distribution of extracellular vesicles together with other particles in biofluids with microfluidic resistive pulse sensing. *PLoS One* **16**, 1–19 (2021).

90. Klykov, O. & Weller, M. G. Quantification of N-hydroxysuccinimide and N-hydroxysulfosuccinimide by hydrophilic interaction chromatography (HILIC). *Anal. Methods* **7**, 6443–6448 (2015).

91. Liu, T. *et al.* Selective Delivery of Doxorubicin to EGFR + Cancer Cells by Cetuximab–DNA Conjugates. *ChemBioChem* **20**, 1014–1018 (2019).

92. Gross, M. E. *et al.* Cellular Growth Response to Epidermal Growth Factor in Colon Carcinoma Cells with an Amplified Epidermal Growth Factor Receptor Derived from a Familial Adenomatous Polyposis Patient. *Cancer Res.* **51**, 1452–1459 (1991).

93. Mitchell, M. I. *et al.* Extracellular Vesicle Capture by AnTibody of CHoice and Enzymatic Release (EV-CATCHER): A customizable purification assay designed for small-RNA biomarker identification and evaluation of circulating small-EVs. *J. Extracell. Vesicles* **10**, (2021).

94. Dovgan, I. *et al.* On the use of DNA as a linker in antibody-drug conjugates: synthesis, stability and in vitro potency. *Sci. Rep.* **10**, 1–9 (2020).

95. van der Pol, E., Gemert, M. J. C. Van, Sturk, A., Nieuwland, R. & Leeuwen, T. G. Van. Single vs . swarm detection of microparticles and exosomes by flow cytometry. *J. Thromb. Haemost.* **10**, 919–930 (2012).

96. Chan, K. C. *et al.* Analysis of the human serum proteome. *Clin. Proteomics* **1**, 101–225 (2004).

97. Singha, S. *et al.* Peptide-MHC-based nanomedicines for autoimmunity function as T-cell receptor microclustering devices. *Nat. Nanotechnol.* **12**, 701–710 (2017).

98. Umeshappa, C. S. *et al.* Suppression of a broad spectrum of liver autoimmune pathologies by single peptide-MHC-based nanomedicines. *Nat. Commun.* **10**, 1–17 (2019).

99. Choi, J. *et al.* Systematic discovery and validation of T cell targets directed against oncogenic KRAS mutations. *Cell Reports Methods* **1**, 100084 (2021).

100. Gimona, M., Pachler, K., Laner-Plamberger, S., Schallmoser, K. & Rohde, E. Manufacturing of human extracellular vesicle-based therapeutics for clinical use. *Int. J. Mol. Sci.* **18**, (2017).

101. Ernsting, M. J., Murakami, M., Roy, A. & Li, S. D. Factors controlling the pharmacokinetics, biodistribution and intratumoral penetration of nanoparticles. *J. Control. Release* **172**, 782–794 (2013).

102. Miteva, M. *et al.* Tuning PEGylation of mixed micelles to overcome intracellular and systemic siRNA delivery barriers. *Biomaterials* **38**, 97–107 (2015).